Single White-Light-Emitting Nanostructures Based on Förster Resonance Energy Transfer: Development, Characterization and Applications

by

Vadim Chirmanov

A thesis
presented to the University of Waterloo
in fulfillment of the
thesis requirement for the degree of
Master of Science
in
Chemistry

Waterloo, Ontario, Canada, 2015

Author's Declaration

I hereby declare that I am the sole author of this thesis. This is a true copy of the thesis, including any required final revisions, as accepted by my examiners.

I understand that my thesis may be made electronically available to the public.

Vadim Chirmanov.

Abstract

Electric energy use associated with lighting reaches up to 3400 Terawatts hours and constitutes approximately 20 % of the world total electricity output per year. That in turn contributes to the release of at least 1900 Mt of CO_2 gas in the Earth's atmosphere. Light emitting diodes have emerged as a possible substitute for the conventional light sources and much effort is directed toward improving them. This project presents results on the development and characterization of white-light-emitting chromophores based on the Förster resonance energy transfer between γ-Ga_2O_3 and organic dyes.

Several experiments were performed to estimate the average number of Rhodamine B molecules per Ga_2O_3 nanocrystal. Under standard conditions efficiency of the energy transfer was found to be between 24 - 49 % for the 3.6 and 5.3 nm nanocrystals, resulting in the average donor-acceptor separations of 2.97 and 3.67 nm, respectively. Data analyses revealed close dependence of the process on the average nanocrystal size. Additional experiments were also conducted with ATTO-590, displaying similar trends.

Generation of white light was achieved based on the color complementarity between blue-emitting γ-Ga_2O_3 nanocrystals and the orange-emitting dye. Additional samples of ZnO with various dyes were also analyzed for color matching. Chromaticity coordinates of (0.332, 0.338) and correlated color temperature of 5528 K were obtained in the colloidal state using a 230 nm excitation source. Series of chromophores were applied to the 255 nm and 300 nm ultraviolet diodes. All devices displayed remarkable characteristics with chromaticity coordinates and color temperatures being close to the point of equal energy, and high color rendering indices. The principle of downconverting a narrow UV radiation to visible white light through resonance energy transfer was demonstrated and applied. Development of completely inorganic conjugates could potentially greatly improve the properties and expand the applications of such phosphors.

Acknowledgements

Firstly I would like to extend my gratitude to my supervisor Dr. Pavle Radovanovic for giving me the opportunity to pursue a degree of Master in Chemistry in his group. I thank you for introducing me to the concepts of solid-state chemistry and presenting me with a fascinating research project on development of new white-light-emitting chromophores. Dr. Radovanovic's support and encouragements helped me to prevail over numerous obstacles that I have faced on my way toward my graduation and I shall never forget it.

I would also like to thank my advisory committee members Dr. Jean Duhamel and Dr. Eric Prouzet for taking their time to provide me with detailed comments and suggestions on my proposal seminar and thesis. Your creative input helped me improve my scientific writing and presentation skills as well as to better understand the subject. I would also like to give a big "Thank you" to Dr. Duhamel and his research group, specifically Michael, Remi and Lu, for extensive training and assistance with numerous TCSPC measurements and data analyses conducted in their lab.

I could not have completed my study without all of the help and support provided by my lab group members - Ian, Shokouh, Ting, Melanie, Tahereh, Manu, Lisa, Paul, Arunasish, Vahid and Terry. Your contribution to my (I hope so) success and your friendship throughout these years are eternally appreciated. Special gratitude goes to Ian, Melanie, Ting and Manu for considerable direct contributions to my research project, I could not have done without you.

I could not have gotten that far without the help from many wonderful people from the University of Guelph and GWC^2. I would like to thank Dr. Schwan, Dr. Rowntree and Dr. Soldatov as well as Ms. Kim Rawson for their motivation in continuation of my education and assistance with my application process. During my several years at the University of Waterloo I have had the pleasure of meeting numerous wonderful people including teaching staff, students and maintenance personnel. In particular I would like to thank all the lab instructors and office personnel I had the opportunity to meet - Sue, Jake, Rick, Cathy and Marguerite (still feel strange being so informal).

I would also like to acknowledge the continuous encouragement and support that my family has shown me throughout my undergrad and graduate days. Always being there for me, any time, any place - greatest people ever, even my loud mouth, know-it-all little sister. Also I would like to include my dog for looking after me and making me go out for long walks in the park. To all my friends in

both Guelph and Waterloo thanks for all the good times - it has been really memorable. I would also like to thank everyone involved with the Grand River Rocks and Guelph Grotto indoor climbing gyms, and Victory Muay Thai for keeping me emotionally and physically healthy. Considering the aspects of a graduate student's life it was extremely important for me to be physically active in order to stay on track and keep my sanity. Special acknowledgement goes to the amazing little brunette girl that I have met in the course of my studies, who has shown me an unbelievable degree of support, understanding, love and care. Thank you, Lisa, for everything you have done for me.

Finally, as a spiritual person who has experienced a lot of unexplainable events in life I would like to thank God for getting me that far and placing all these amazing people and events in my path. Always taking time answering my prayers, extending invisible hand to pull me out of the mess I made - truly incredible. I am really sorry for all the pain and stress I might have caused to others over the past few years, I truly am sorry. I tried to do my best.

Sincerely,

Vadim V. Chirmanov.

Table of Contents

List of Figures

List of Tables

List of Abbreviations

A490	ATTO-490
A565	ATTO-565
A590	ATTO-590
A610	ATTO-610
acac	Acetylacetonate
CB	Conduction Band
CCT	Correlated Color Temperature
CFL	Compact Fluorescent Lamp
CIE	*Commission internationale de l'éclairage*, International Commission on Illumination
CMF	Color Matching Function
CQS	Color Quality Scale
CRI	Color Rendering Index
DAP	Donor-Acceptor Pair
DI	Deionised
DNA	Deoxyribonucleic Acid
EQE	External Quantum Efficiency
FRET	Förster Resonance Energy Transfer
ICP	Inductively Coupled Plasma
IR	Infrared
IRF	Instrument Response Function
LED	Light-Emitting Diode
NC	Nanocrystal
NP	Nanoparticle
OAm	Oleylamine
OAc	Acetate
PL	Photoluminescence
ppm	parts per million
QBS	Quinine Bisulfate

QD	Quantum Dot
QY	Quantum Yield
RB	Rhodamine B
RBL	Rhodamine B Lactone
RT	Room Temperature
SD	Standard Deviation
SPD	Spectral Power Distribution
TCO	Transparent Conducting Oxide
TCSPC	Time Correlated Single Photon Counting
TEM	Transmission Electron Microscopy
TIR	Total Internal Reflection
TOPO	Tri-*n*-octylphosphine Oxide
UV	Ultraviolet
UV-vis	Ultraviolet-visible
VB	Valence Band
WLED	White Light-Emitting Diode
XRD	X-Ray Diffraction
YAG	Yttrium Aluminum Garnet

Chapter 1
Introduction to Solid-State Lighting

1.1 Development of the Efficient Light Sources

1.1.1 Technological Advances and Their Effects on the Environment

The past century has shown a dramatic leap in technology, which has led to a considerable increase in the world's population and average life expectancy.[1] The ever-growing demand for energy has increased the consumption of fossil fuels,[2] which further contribute to the increase of CO_2 concentration in the atmosphere. Geological studies have indicated a correlation between the levels of CO_2 and its effect on the pH of oceans.[3] More recent studies have shown increase in the CO_2 content from 200 parts per million (ppm) to 380 ppm as a direct result of human activity.[4] Rising levels of CO_2 inevitably lead to the acidification of water, which has a severe adverse effect on the shell-forming species.[4,5] Such environmental changes could have severe adverse effects on the oceanic biosphere as well as the rest of the planet in the future. Daily use of the electric energy associated with lighting of residential, commercial, outdoor and industrial sectors reaches up to 3400 Terawatt hours and constitutes approximately 20 % of the world's total electricity output per year.[6] Brightly lit urban areas of the world are clearly visible in Figure 1.1, showing Earth's surface at night as seen from orbit. Such energy consumption contributes to the release of at least 1900 Mt of CO_2 gas in the planet's atmosphere.[6] As a result, the development of efficient and environmentally friendly light sources is required. Light emitting diodes (LEDs) have emerged as a possible solution but additional work is still needed to further explore their full potential.

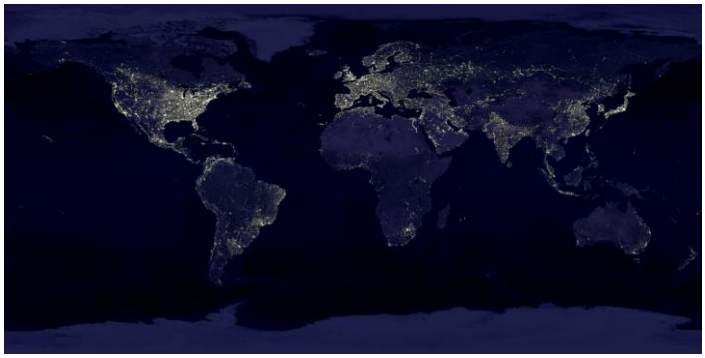

Figure 1.1. View of Earth's city lights from the orbit (courtesy of NASA).

1.1.2 Properties and Characteristics of the Common Light-Emitting Sources

Generation of visible light by the artificial sources can be attributed to the following two processes - incandescence and fluorescence. Incandescence results in the emission of visible light due to increase in the temperature of the emitting material, producing a great amount of heat and infrared (IR) radiation. This principle is widely utilized in the tungsten filament bulbs. As illustrated in Figure 1.2a, only a fraction of the incandescent light bulb's spectral power distribution (SPD) falls within the visible spectrum. Therefore, a typical tungsten filament lamp converts only 1-5 % of electricity into visible light[7] and has a luminous efficacy range of 10-18 lm/W (Figure 1.3) and a lifetime of ~1000 hours.[8] Its emissions produces a characteristic orange-red hue (Figure 1.2d) and the only way of improving it would be to increase its operating temperature (6000-7000 K), which is quite impossible.

Compact fluorescent lamps, or CFLs, operate on the principles of fluorescence, as the name suggests. Such lamps contain mercury in their tubes, and a ballast, which forces electrical current through the mercury gas, generating ultraviolet (UV) radiation. Such UV radiation can be used to excite different fluorescent coatings on the inside of the tube thus generating emission of visible light (Figure 1.2b and d), using several luminescent components. Variations in the composition of such coatings can be used to tune the resulting emission over a broader spectral range. Such lamps usually have higher luminous efficacy (35-60 lm/W)[9] and a longer lifetime (6000-15000 hours),[10] compared to the incandescent light bulbs. The notable downsides include complications with recycling due to mercury, higher initial cost of the device and its potentially low chromaticity due to poor color mixing (Figure 1.2d).[9] Figure 1.2b shows SPD of daylight at noon and its corresponding features are what an ideal source of artificial day light should have - a considerable contribution from the three primary colors over the entire visible range. As indicated in Figure 1.3b, there has been virtually no increase in the efficacy of the above mentioned devices in the past decades and their lifetime parameters are not likely to be improved either. Emergence of the solid-state lighting has presented a new direction toward development of the new types of the energy-saving light sources.

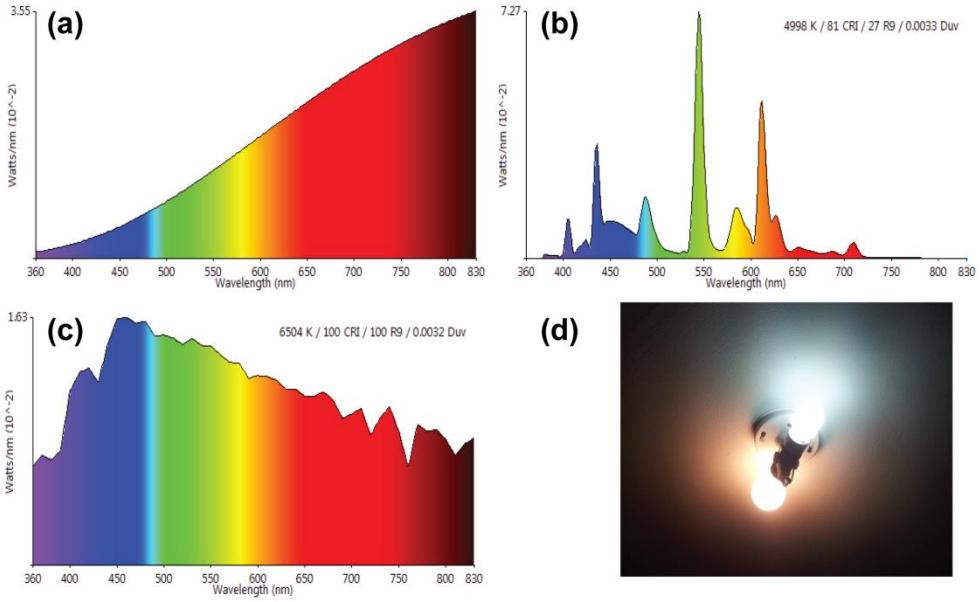

Figure 1.2. (a) SPD of a tungsten filament lamp. (b) SPD of a compact fluorescent lamp. (c) SPD of daylight (sunlight) at noon. (d) Difference in "white" light emitted by a typical incandescent lamp (bottom) and a CFL (top).

Light-emitting diodes (LEDs) have emerged as a more efficient and a cost effective alternative to the conventional light sources.[11] A typical LED requires 90 % less energy to operate, has a higher luminous efficacy, which continues to increase (45 lm/W in 2000 to 92 lm/W in 2009), an impressive 50,000-hour lifetime and a good color mixing.[8,9,11] Such devices may suffer decrease in the performance and operation due to packaging and a possible internal reflection, driver losses, optical losses due to fixtures and lenses, thermal effects and high initial unit cost.[9] Other issues are related to the material utilized in most of the LEDs - InGaN - and lead to the overall decrease in the efficiency of the device. The possible reasons include overflow of the localized states carrier,[12] the p-type semiconductor side being flooded with electrons,[13] Auger recombination,[14] and others such as efficiency reduction at a high current flow due to the defect related contributions leading to a nonradiative parasitic process.[15, 16] Even though LEDs have a great potential, the actual production and applications could further be restricted by a complicated manufacturing process and the device's structure, a poor color mixing and a low color quality of the LED, or a low stability and the overall performance of the phosphors.

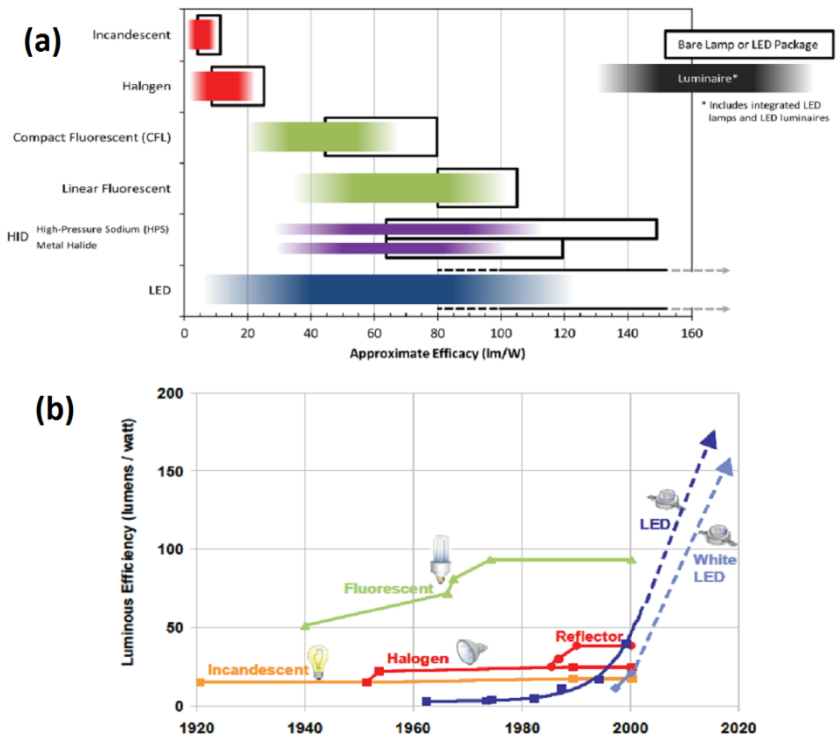

Figure 1.3. (a**)** Average efficacy of some of the light-emitting devices (box border) and their corresponding luminaires (shaded region).[8] (b) Increase in the efficacy of some devices over time, dashed lines indicate pedicted trend.[9]

1.1.3 Principles of Operation and Structure of a Basic LED

Basic principle of luminescence found in a typical LED is not as new as Figure 1.3-B may suggest, and has been reported in 1907 by H. J. Round, who conducted experiments on carborundum.[17] Decades later, Oleg Losev conducted research specific to the development of LEDs, but his work went largely unnoticed due to the onset of World War II.[18] The year 1962 is significant because it witnessed the emergence of the first LED within the visible spectrum by Nick Holonyak, leading to a significant expansion in the past 50 years.[19] The principle of operation of a typical LED relies on the process known as electroluminescence and depends heavily on the material.

In general the emission of light in LED originates from the radiative electron-hole recombination in the *pn*-junction under the applied bias (Figure 1.4). The emissive layer consists of the heavily doped semiconductors forming *n*-type and *p*-type carriers. Under zero applied voltage the built-in potential V_0 prevents electrons and holes from recombining. When voltage is applied, this

potential barrier is decreased and electron-hole recombination occurs within the device, resulting in the emission of photons. Control over the wavelength of the resulting emission is achieved through changes in the band gap energy of the material.[20] Once emission occurs, these photons need to escape the device without being reabsorbed or reflected so the actual LED structure is more complex than the *pn*-junction shown in Figure 1.4.

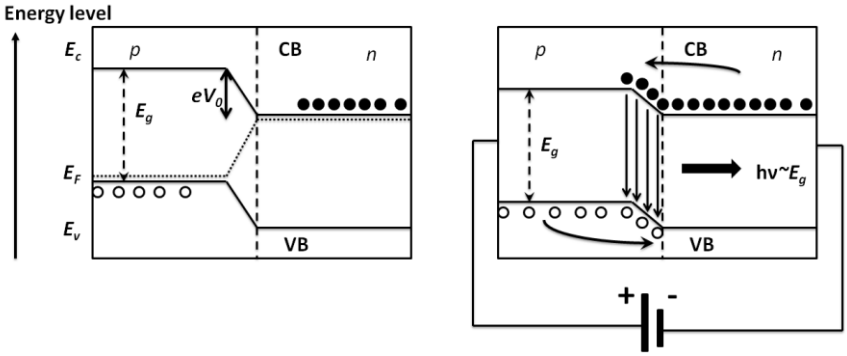

Figure 1.4. Schematic representation of the energy band diagram of a *pn*-junction without any bias (left) and with an applied voltage (right), resulting in the electron-hole recombination with the emission of photons.

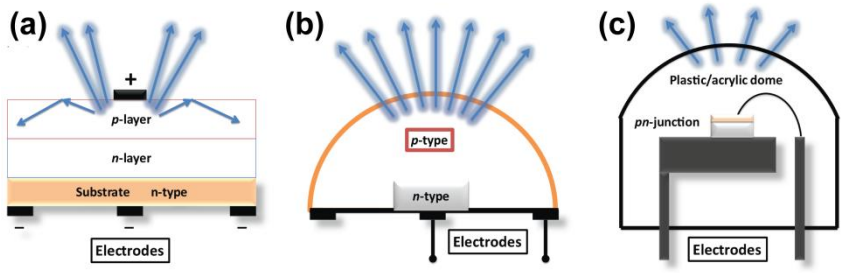

Figure 1.5. (a) Device structure with a flat top where light suffers TIR. (b) *p*-type semiconductor is shaped as a dome to overcome some of the TIR. (c) The emissive centre and the electrodes are encapsulated in the transparent acrylic dome.

As mentioned above, the possibility of light suffering a total internal reflection (TIR) is a serious concern. Figure 1.5a shows a very basic sketch of a flat top LED with a very small critical angle. Upon emission, numerous photons in such a device would not be able to escape the LED due to TIR, reducing its efficiency. To counter it, the p-type semiconductor can be engineered as a dome (Figure 1.5b), but that would lead to an increased manufacturing cost. A cheaper alternative would be

encapsulation of the device in an acrylic dome (Figure 1.5c) or to apply a patterned sapphire substrate. The surface of such a substrate is modified through etching to introduce surface distortions, which scatter the emitting light and thus improve the efficiency of the LED.[21]

When it comes to generating white light, most white-light-emitting diodes (WLEDs) work on the principles shown in Figure 1.6. Usually a narrow UV or blue emission from an LED is used in conjunction with various phosphors to generate multiple emission bands, jointly resulting in white light.[22] Using a phosphor downconversion, it is possible to produce white light by a careful mixing of two components in a complementary spectral range.[23] Several methods have been reported, where generation of white light has been achieved by mixing of the three primary colors, originating from the red, blue and green LEDs.[24-26] Applications of the various rare-earth elements,[27,28] organic materials in conjunction with precious metals,[29] and quantum dots (QDs)[30,31] have all been reported. Such devices may be too complex to manufacture, have a high initial cost or a poor performance as some luminescent components may degrade faster than the others. Additionally, the current/voltage dependence of the LED components may vary, therefore undermining its full potential and the external quantum efficiency (EQE). Other limiting factors may include lack of the efficient green, yellow and orange-red emitters that are necessary for the proper color mixing. As a result such devices may have poor chromaticity, color temperature and color rendering.

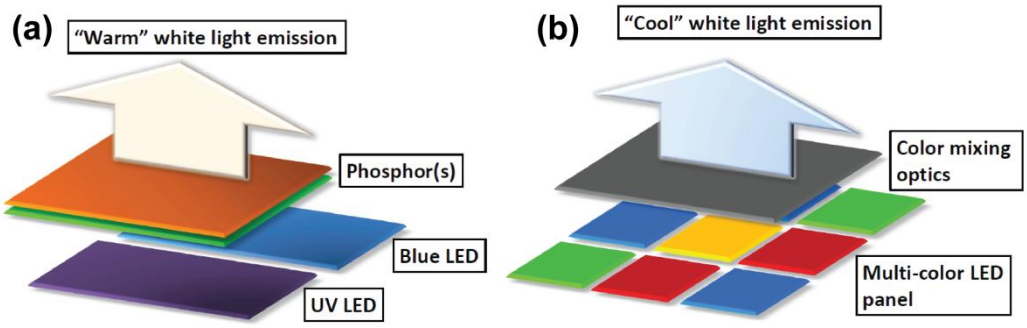

Figure 1.6. (a) Generation of white light by a phosphor downconversion using a UV/blue LED. (b) Generation of white light by a controlled and selective color mixing from the multiple emitters. Note: "warm" and "cool" here simply show the complexity of an ideal color mixing in the LED and not the resulting emission under a given configuration.

1.1.4 Characterization of the LEDs

When discussing light-emitting sources, it is important to understand how such devices are characterized. For example, both incandescent and fluorescent lamps emit "white" light, but as seen in Figure 1.2d the resulting emission hues are quite different. In order to avoid any confusion in characterization of light, *Commission Internationale de l'Eclairage* (CIE, International Commission on Illumination) has established a set of standards and a mathematically defined color space (Figure 1.7a),[32] which allow any emission to be classified in terms of two chromaticity coordinates, *x* and *y*.

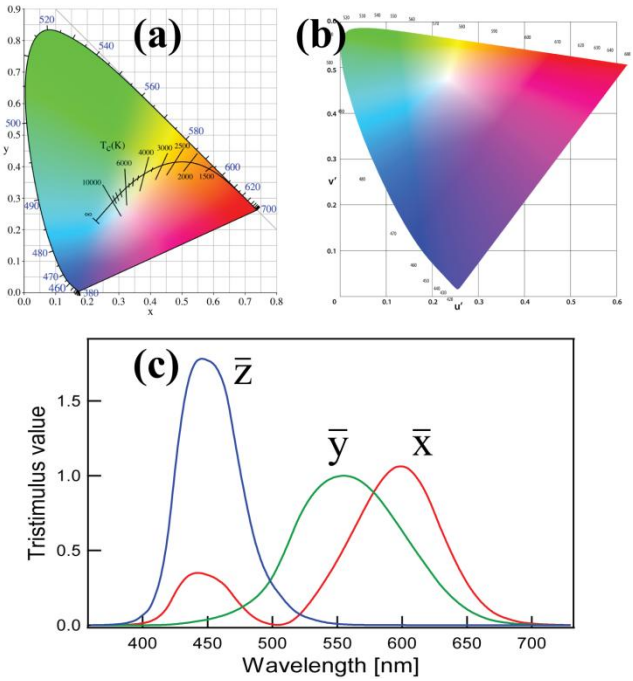

Figure 1.7. (a) 1931 CIE color space also showing Planckian locus (curved line). (b) 1976 CIE color space. (c) A set of CMFs for the 1931 CIE color space.

Such mathematically defined chromaticity diagram is based on the works of Wright[33] and Guild[34] conducted in the 1920's and is, perhaps, the most widely used method of defining color. It is based on a set of three primaries (red, blue and green), the human eye response to color, and a set of other principles, such that any color can be represented as a sum of the three primaries. The relationship to the sensitivity of the human eye is achieved with the use of three color matching functions (CMFs, Figure 1.7c), whose values have been derived theoretically.[35] Using this set of

CMFs and any given standard illuminant, the characteristic tristimulus values *X*, *Y* and *Z* can be calculated as follow:

$$X = \int_0^\infty I(\lambda)\bar{x}(\lambda)d\lambda \quad \text{(Equation 1)}$$

$$Y = \int_0^\infty I(\lambda)\bar{y}(\lambda)d\lambda \quad \text{(Equation 2)}$$

$$Z = \int_0^\infty I(\lambda)\bar{z}(\lambda)d\lambda \quad \text{(Equation 3)}$$

where λ is the wavelength in nanometers, *I(λ)* is the SPD of a specific light source at a certain wavelength and $\bar{x}(\lambda)$ is the value of the corresponding CMF at that wavelength. Finally, the chromaticity coordinates are calculated by normalizing the tristimulus values:

$$x = \frac{X}{X+Y+Z} \quad \text{(Equation 4)}$$

$$y = \frac{Y}{X+Y+Z} \quad \text{(Equation 5)}$$

The full list of concepts outlined by the CIE is rather complicated and includes numerous additions and reviews, like the 1976 color space (Figure 1.7b), and is the scope of colorimetry; actual parameters are commonly derived from photoluminescence (PL) spectra using computer software.

Another frequently used characteristic of the white light source is correlated color temperature or CCT, which is reported in Kelvin. CCT refers to the temperature of an ideal blackbody whose color most closely represents the one emitted by the given test source.[36] Blackbody radiation curve is shown on the CIE diagram in Figure 1.7a, and is derived from Planck's radiation law. Colors that appear red-orange (2700 - 3000 K) are classified as "warm" and the ones that are more blue (above 5000 K) are called "cool".[37]

Another parameter often used to evaluate lighting devices is the color rendering index (CRI). It represents the ability of a test light source to render colors as close as possible compared to a given reference source. It is usually reported on a 0-100 scale, though negative values are also possible.[38] A reference source could be an ideal blackbody with the same or similar CCT, or sunlight at a particular time of day. A tungsten filament lamp has a CRI of 100 as it is a blackbody, while other devices can usually score anywhere between 40 and 95. A score of 85 and above is considered acceptable for a device to be used for indoor applications. In order to obtain the CRI parameter, the 1931 CIE

chromaticity coordinates of the test source need to be converted to the 1976 CIE color space. The test source should ideally be close to the Planckian locus (or the reference source) in order for the CCT to have meaning. The actual separation is calculated using the following expression:

$$\Delta_{uv} = \sqrt{\left(u_t^{'} - u_p^{'}\right)^2 + \frac{4}{9}\left(v_t^{'} - v_p^{'}\right)^2} \qquad \text{(Equation 6)}$$

In the above equation *t* and *p* subscripts denote chromaticity coordinates for the test and reference light sources on the 1976 CIE color space and the difference should not exceed 0.05 coordinate units. Then the 8 reference color samples are illuminated and the chromaticity coordinates of their corresponding reflection spectra are calculated. The difference between the two values is then calculated for each reference color standard using the following relationship:

$$R_i = 100 - 4.6\Delta E_i \qquad \text{(Equation 7)}$$

R_i denotes a particular CRI value for any given reference color and ΔE_i is the Euclidean distance between the pair of coordinates. Finally, CRI for the given test source is found by calculating the arithmetic mean:

$$R_a = \frac{1}{8}\sum_{i=1}^{8} R_i \qquad \text{(Equation 8)}$$

The CRI system has been criticized for its poor ability to represent true characteristics of light sources with CCT below 5000 K.[39] Additionally, having only 8 reference colors was quite inadequate, as well as the inability of some of the reference light sources to render light perfectly at extreme CCTs. Thus an alternative system called color quality scale (CQS) has been proposed.[40] CQS aims to introduce more reference colors, especially in the red region, in order to provide a better assesment of the device's color rendering ability.

Another parameter often included in characterization of LEDs is luminous efficacy. It relates to the ability of a given light source to produce light in the visible spectrum that can be detected by the human eye.[41] It is derived from the ratio of the luminous flux to power and is reported in lm/W. Based on the human eye response to visible light, a theoretical maximum luminous efficacy of 683 lm/W is possible for a monochromatic light at 555 nm. The sensitivity to all other wavelengths decreases gradually toward UV and IR spectral ranges. For the WLEDs the value of 683 lm/W is impossible since two or more color components are usually used. It was estimated that WLEDs could potentially reach luminous efficacy of 250-370 lm/W based on their structure and configuration.[41]

1.2 Specific Examples of the WLEDs

The actual "white light" range covers a large section of the color space, therefore *x*/y coordinates with values of 0.3 to 0.4 are acceptable.[42-44] Variations in the CCT and CRI values are also noted and can be anywhere between 3000-7500 K and 70 to 95, respectively. Complexities of a typical WLED associated with the layout, doping concentration and thicknesses of the material layers could result in different performance even between LEDs of the same type. Furthermore, the excitation wavelength of the base UV and blue chips can vary from 330 nm to 460 nm,[44] which requires the development of new and efficient yellow and orange-red emitting phosphors to match the chromaticity of such emission. Usage of multiple red, blue and green LEDs to produce white light is complicated by variations in the driving current required to facilitate the emission, thermal stability, and efficiencies of the phosphors. All of these factors can potentially increase the manufacturing and retail costs of the device limiting its applicatons.

Perhaps one of the best known WLEDs is the GaN-based blue LED coated with the yellow-emitting yttrium aluminum garnet (YAG, $Y_3Al_5O_{12}$) doped with Ce^{3+}. White light is generated by the combination of blue (LED) and yellow light from YAG:Ce, resulting from downconversion of the blue emission by the phosphor.[22,24] The device suffers a few drawbacks due to the lack of red in its emission spectrum, which leads to its overall low CRI and chromaticity coordinates. Additionally, dopants often used to modify properties of the nanomaterials are rare earth metals, which are scarce and expensive.

Several attempts have been made to generate white emission with the help of quantum dots.[45] A combination of red, blue and green-emitting QDs was incorporated into a monolayer and white light was generated through electroluminescence. The emission could be tuned by changing the ratios of the QDs without changing the device's structure. EQE of 0.36 % was achieved, chromaticity coordinates of (0.35, 0.41) and CRI of 86 (5500 K reference) were also reported. This approach showed great promise, if not for a low EQE and luminous efficacy, partially related to different band structures of the various QDs. Multiple other attempts have been made to generate white light by using nanocrystals (NCs) and magic-sized QDs with good results.[46,47,31]

Another interesting approach for generation of white light was reported to include Eu(III) doped Y_2O_3 NCs that were surface passivated by acetylacetonate and 1-hexadecylamine.[48] The addition of acetylacetonate resulted in some strong ground to excited electron transitions and Eu(III) ligand to metal charge transfer. Excitation of such phosphor has led to the emission of white light due

to energy transfer to the Y_2O_3 surface defects and Eu f-f transitions. EQE of 19 %, CIE chromaticity coordinates of 0.33 and 0.35 (based on Eu concentration), and luminous efficacy of 100 lm/W were obtained. Another type of WLED based on Mn and Cu co-doped ZnSe QDs was reported as well. In that case, the combination of excitonic emission with emissions from multiple dopants gave rise to white light.[49]

In some other reported cases, emission was achieved utilizing only one component capable of emitting at multiple wavelengths.[50,51] A single white-light-emitting molecule was developed realizing excited-state intramolecular proton transfer materials based on hydroxyphenyl imidazole and its naphthalene derivatives.[50] Another approach was based on a single polymer (polyfluorene backbone) with singlet (benzothiadiazole) and triplet (iridium (III) complex) chromophores attached to it. A single molecule approach holds many advantages over other methods as a potentially simpler, cheaper and efficient way to generate white emission. On the other hand, it could be really complicated from a synthetic point as significant molecular modifications are required to obtain a broad emission.[51]

Particularly interesting is the ability to generate white light through energy transfer between two or more chromophores. Several approaches have been reported where energy transfer was achieved between molecules and dopants with reasonable success.[52-55] This principle is rather intriguing and holds great potential, however, it has not yet been fully developed and explored. Such method could be applied to nanoparticles like QDs and transparent conducting oxides (TCOs), and is worthy of further development. The energy-transfer-mediated emission of white light between inorganic and organic components of a single chromophore forms the basis of this project. It could lead to the development of a new type of potentially cheaper and equally efficient WLEDs.

1.3 Scope of the Research

1.3.1 Controlling Properties of the Nanomaterials

Nanomaterials such as QDs and TCO nanocrystals possess a great variety of useful applications based on their intrinsic properties like size dependent luminescence, optical transparency and conductivity.[56-58] The range of applications includes optoelectronics, displays, LEDs, molecular sensors, photocatalysts, bioimaging and others.[59-63] Numerous applications have been made possible

as a result of careful and meticulous modifications to either crystal lattice compositions and/or surfaces of these materials.

Introduction of another element in the lattice may lead to new modes of luminescence through different excitation mechanisms of QDs and TCOs. For example, incorporation of lanthanide metals in the lattice of the nanoparticles (NPs) can lead to the photon upconversion due to the f-f transitions from the metal ions.[64] Such NPs have found application as biocompatible labelling agents for upconversion fluorescence microscopy.[63,65] Additional extensive surface modifications have also been applied in order to make such NPs compatible with polar solvents. Considering the extremely small sizes of the NPs, they are very susceptible to the Brownian diffusion.[66] To counter that, the NP surface can be treated with various ligands, enhancing their overall stability.[67,68] Such surface modifications can help stabilize NPs in polar or non-polar media, prevent agglomeration, allow binding to substrates and enhance luminescence.[69-71]

A ligand exchange at the metal sites of the NP surfaces has been demonstrated, leading to the formation of stable bonds.[72,73] Subsequently, QDs have been shown to form a stable bond with Rhodamine B (RB), which could potentially be used as an orange emitter complementary to the blue LED and/or TCO nanoparticle.[74] Such conjugates have also shown the ability to undergo emission from the dye component based on resonance energy transfer upon excitation of the QD.[75] An efficient and fast defect-mediated energy transfer has been demonstrated between ZnO nanoparticles and AlexaFluor 594 dye, as well as a QD and a polymer.[76,77] Both steady-state and time-resolved photoluminescence (PL) spectra were analyzed, indicating a remarkable degree of interaction between NPs and the dye even when only one molecule was attached. A suitable TCO-dye pair can potentially result in an efficient energy transfer, leading to the generation of white light from a quasi-single chromophore.

1.3.2 Introduction to the Förster Resonance Energy Transfer Formalism

Fluorescence resonance energy transfer (FRET) between two luminescent molecules in solution has been described by Theodor Förster in 1948[78] and since then it has gained popularity as an effective scientific analytical method.[79] FRET is based on the electrodynamic interactions between the two species through space closely resembling a long-range dipole-dipole interaction. Upon excitation of the donor species, a portion of its energy can be transferred to the acceptor without emission or reabsorption of a photon (Figure 1.8). The process is distance-dependent, usually

occurring within 1 to 10 nm, and does not involve any molecular collisions or energy conversions.[79] FRET efficiency depends on the spectral overlap between the donor emission and the acceptor absorption (Figure 1.9), as well as the mutual spatial orientation of the two species.

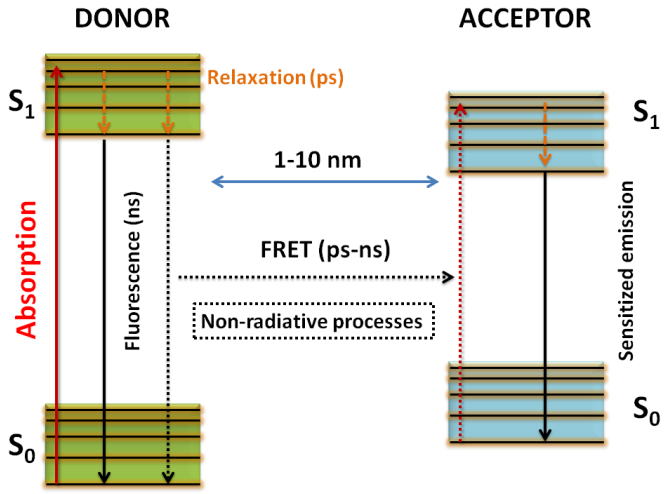

Figure 1.8. Jablonski diagram showing the process of non-radiative energy transfer between a donor and an acceptor.

Spectral overlap integral J (Figure 1.9) is an important characteristic of a FRET donor and acceptor interaction. It relates to the critical distance parameter R_0 (also called the Förster radius), which determines the distance at which the efficiency of the energy transfer E is 50 %. Value of J can be calculated from the following equation:[79]

$$J = \int F_{\mathrm{D}}(\lambda)\varepsilon_{\mathrm{A}}(\lambda)\lambda^4 d\lambda \qquad \text{(Equation 9)}$$

In the above equation, F_{D} is the donor emission integral normalized to 1 and is usually expressed in nanometers with respect to the wavelength, and ε_{A} is the acceptor molar extinction coefficient at the wavelength λ (in $M^{-1}cm^{-1}$). The value of J usually has units of $M^{-1}cm^{-1}nm^4$ but can also be expressed in $M^{-1}cm^3$. Magnitude of the molar extinction coefficient plays a big role in the determination of the value of J, so it must be derived correctly for the given FRET acceptor.

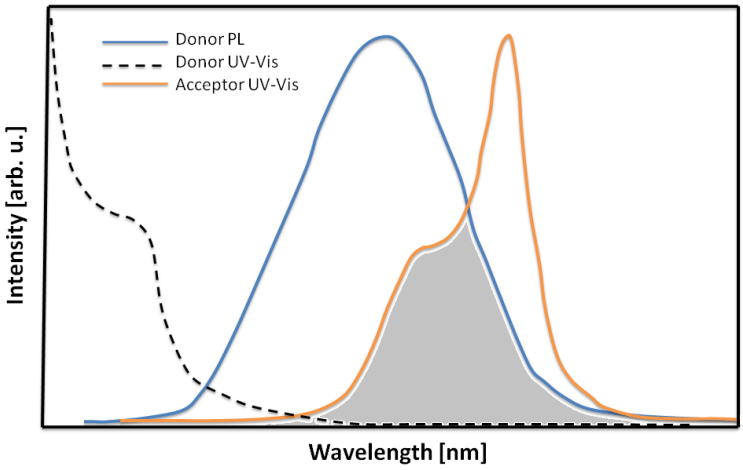

Figure 1.9. Schematic diagram showing a generic spectral overlap (shaded grey area) between donor emission and acceptor absorption spectra.

The critical distance R_0 is defined by the following equation:[79]

$$R_0 = \left[\frac{9000 Q_0 (\ln 10) \kappa^2 J}{128 \pi^5 n^4 N_A} \right]^{1/6}$$

simplified form (Equation 10)

$$R_0 = (8.79 \times 10^{-25} \times \kappa^2 \times n^{-4} \times Q_0 \times J)^{1/6}$$

In the above equation, Q_0 is the quantum yield (QY) of a donor in the absence of an acceptor, n is the refractive index of the medium, N_A is Avogadro's constant, κ^2 is the dipole orientation factor. The energy transfer efficiency E relates to the critical distance and actual donor-acceptor separation, R_{DA}, through the following expression:[79]

$$E = \frac{1}{1 + \left(\frac{R_{DA}}{R_0} \right)^6} \quad \text{(Equation 11)}$$

The energy transfer efficiency can be determined from the PL or lifetime measurements and is expressed as follows:[79]

$$E = 1 - \frac{F_{DA}}{F_D} \qquad \text{(Equation 12)}$$

In the above equation, F_{DA} and F_D are the integrated donor emission with and without the presence of the acceptor, respectively. In the case of the time-resolved measurements, corresponding lifetime values are used. Finally, to determine the donor-acceptor separation Equation 11 can be rearranged to solve for R_{DA}:[79]

$$R_{DA} = R_0 \times \left(\frac{1-E}{E} \right)^{\frac{1}{6}} \qquad \text{(Equation 13)}$$

The above equation describes an ideal case where energy transfer occurs between one donor and one acceptor separated by a certain distance. In the case of a homogeneous donor-acceptor conjugate with *n* acceptor species per one donor a slightly different equation should be used:[75,83]

$$R_{DA} = R_0 \times \left(\frac{n(1-E)}{E} \right)^{\frac{1}{6}} \qquad \text{(Equation 14)}$$

In this case, *n* represents the number of the energy accepting species of the same type allocated around one donor. Such approximation is acceptable in cases where the resulting stoichiometry can be clearly controlled or the majority of the biding sites are occupied, so the donor-acceptor ratio remains fairly constant.[75,83] When dealing with hybrid conjugates based on the NPs such as QDs coupled with dyes, it is fairly hard to maintain a perfect homogeneity. To account for a possible distribution of the acceptor molecules, a model describing FRET in the restricted geometries should be applied; additional details on this subject will be discuss in the follow-up sections.

In theory derivations of all parameters appear fairly straightforward and FRET donor-acceptor distances can be accurately obtained experimentally. PL measurements yield *E*, then *J* can be calculated, leading to the determination of R_{DA}. Based on this, FRET has gained popularity in the 1960s as an analytical tool and has been dubbed a "spectroscopic ruler".[80,81] In reality, however, things are a lot more complicated and the actual distance measurement with FRET instead produces an approximation.[82] The first obvious complication is that classical FRET formalism treats both donor and acceptor species as points in space. If large NCs act as energy donors they can hardly be approximated as points in space. Another source of error could be the value of the donor's QY. The

molar extinction coefficient for the acceptor can change upon binding, further contributing to the experimental uncertainty. The number of the donor NCs could also be underestimated and lead to the incorrect donor-acceptor ratios.[76,83] Finally, the dipole orientation factor κ^2 is usually approximated as 2/3, mostly because it is nearly impossible to determine accurately in many cases.[83,84] Figure 1.10 shows the graphical definition of κ^2 and the range of its possible values.

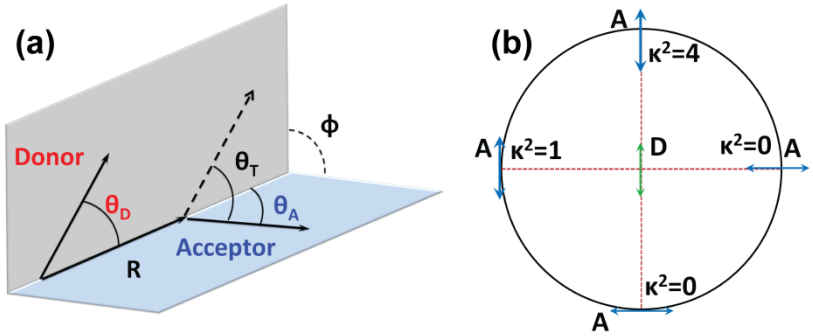

Figure 1.10. (a) Donor emission and acceptor absorption dipole moments defining the orientation factor κ^2. (b) Possible magnitude of κ^2 based on the donor-acceptor orientation, 0 for an orthogonal systems and 4 if both D and A are aligned in-line. A denotes Acceptor and D - Donor, R - separation vector.

Numerical value for the dipole orientation factor can be obtained through the following expression:[79]

$$\kappa^2 = \left(\cos\theta_T - 3\cos\theta_D \cos\theta_A\right)^2 \qquad \text{(Equation 15)}$$

Additionally, $\cos\theta_T$ is defined as:[79]

$$\cos\theta_T = \sin\theta_D \sin\theta_A \cos\phi + \cos\theta_D \cos\theta_A \qquad \text{(Equation 16)}$$

In the above equations, *A* and *D* denote angles associated with acceptor and donor respectively, and ϕ is the angle between the donor and acceptor planes. Methods commonly employed to determine κ^2 include molecular dynamic simulations, binding and distribution modeling for a given system of FRET donors and acceptors, or time-resolved anisotropy experiments.[85-88] Therefore, the dynamic average of 2/3 is often used in calculations since no other alternative could be obtained. In the case of QDs such value was deemed to be acceptable due to the numerous possible surface binding sites for the multiple acceptors.[75,83] There have also been reports where FRET occurred between orthogonal donor and acceptor.[89,90] Experiments with the labeled DNA (deoxyribonucleic acid) molecule also demonstrated the importance of knowing the correct value of κ^2. In this instance DNA segments with

larger donor-acceptor separation exhibited greater energy transfer efficiency solely based on the spatial orientation of the donor and the acceptor based on the DNA twists.[91] FRET is a very good technique for detecting changes in the system and is widely used to analyze protein and DNA binding dynamics.[88,91]

1.3.3 Choosing Energy Donor and Acceptor for an Efficient FRET

The choice of an appropriate FRET donor and acceptor pair typically depends on the experimental conditions and objectives. Both donor and acceptor should have a considerable spectral overlap to provide efficient energy transfer, and the resulting emission colors should be complementary to each other. A good degree of control and tunability of the resulting emission should also be maintained, as well as a good overall stability of the conjugate. For that purpose TCOs can be used as energy donors and a source of blue emission. Of a particular interest is the gamma phase gallium oxide (γ-Ga_2O_3), which exhibits a strong defect induced luminescence as a result of the oxygen and gallium vacancies.[92] Among other TCOs, Ga_2O_3 has one of the largest band gaps of ~4.9 eV and five different crystal structures have been reported (α, β, γ, δ and ε).[93] Owing to its high thermal stability, β-Ga_2O_3 has been the focus of numerous studies and the nature of its luminescence has been closely examined.[92,94] Excitation of gallium oxide in the band gap can result in the emission in the UV or blue spectral ranges. UV emission is attributed to the recombination of a self-trapped exciton; blue emission originates from an electron trapped on the donor and a hole trapped on the acceptor sites, which are formed as a result of oxygen vacancies and gallium and/or gallium-oxygen vacancies respectively (Figure 1.11).[92,95,96]

Such process is referred to as the donor-acceptor pair (DAP) recombination. In order to avoid any possible confusion with the FRET donor and acceptor, DAP will be addressed as trap recombination further on, while FRET donor and acceptor will be referred to as such. Figure 1.11 shows the processes leading to the DAP recombination and the resulting emission of a photon. Upon excitation, electrons are promoted from the valence band (VB) to the conduction bad (CB). Such electrons can be trapped by the ionized donors while holes can be trapped by the ionized acceptors. Electrons can then undergo quantum tunneling from donor toward the acceptor sites and recombine radiatively, with the resulting emission wavelength being governed by the separation between the donor and acceptor levels.

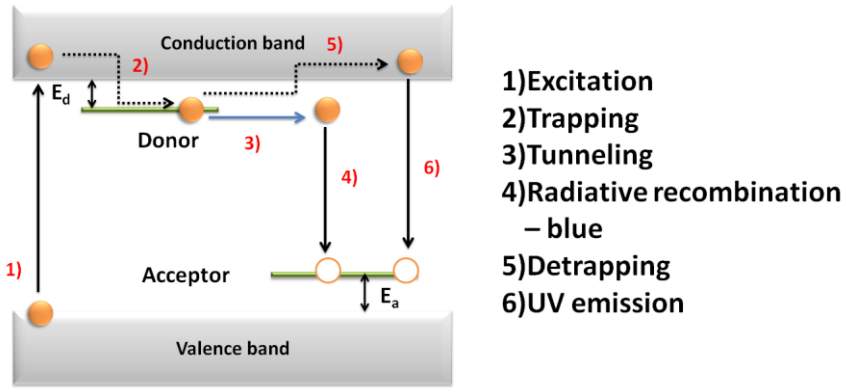

Figure 1.11. Schematic diagram showing nature of the defect induced luminescence in gallium oxide as a result of the DAP recombination.

Because ionization persists, there will be Coulombic interactions between the two and the overall energy of the resulting emission can be expressed as such:[97]

$$E = E_g - (E_d + E_a) + \frac{e^2}{4\pi\varepsilon r} \pm nE_{phonon} \qquad \text{(Equation 17)}$$

where E_g is the band gap energy, E_d and E_a are the donor and acceptor binding energies, followed by the Coulombic interaction term, and finally E_{phonon} is the energy of phonons responsible for the radiative transitions.

Previously a new and simple method of preparation of colloidal γ-Ga_2O_3 NCs has been reported,[98] followed by additional studies on explaining and controlling luminescence through sample preparation methods and doping.[97,99-101] Cubic γ-Ga_2O_3 has a defect spinel crystal structure with the unit cell dimensions of 8.23760 Å, where Ga^{3+} ions occupy 21and 1/3 of the available 24 cation sites.[102,103] The new synthetic method allows for control of the NC size and the resulting emission wavelength through variations in temperature. So far, particles with the average sizes of 3.0 to 6.0 nm have been reported, resulting in the emission covering violet-blue (410 nm) to blue-cyan (460 nm) range. The emission itself is broad, partially due to a large particle size distribution, and generally has a high quantum yield (up to 25 % for smaller particles). Overall, such NCs provide a good base for an efficient FRET donor with a strong blue luminescence. Variations in particle sizes can potentially be used to control the spectral overlap with the FRET acceptor or to allow for more acceptor molecules

to bind on the surface of the same nanocrystal. These properties can be used to tune the resulting FRET-mediated emission and color complementarity.

When it comes to FRET acceptors, the Rhodamine family of organic dyes can potentially make for a good starting model system. Figure 1.12a shows the absorption and emission spectra of a typical Rhodamine B (RB) cation in water and Figure 1.12b shows its molecular structure. RB and its derivatives like the ATTO dyes (Figure 1.13) generally contain a free carboxylic group, which can be further modified. An extended π network can give rise to a strong fluorescence upon transition from π to π* levels due to the formation of the singlet state, but triplet states are also possible.[104] The numbers for QY, lifetime and ε vary from 70 %, 2.8 ns and 106000 $cm^{-1}M^{-1}$ in ethanol to 30 %, 1.6 ns and ~90000-106000 $cm^{-1}M^{-1}$ in water, respectively. It should be noted that the above mentioned parameters vary more sharply for RB in water due to dimerization.[105-107]

Structurally, RB dye is a relatively big molecule and its free carboxylic group allows it to be attached to the surfaces of NCs.[108] It is a good fluorescent label and, based on its absorption and emission spectra, it should provide a considerable spectral overlap with the blue emission of Ga_2O_3 NCs. Rhodamine 6G is rather similar to RB and it is reported to be 1.38 nm long (along the xanthene group), 1.15 nm across, and ~0.90 nm "thick" since it is not planar.[109] Considering the size of the NCs and the distribution of the defects, there should be a considerable probability for FRET to occur. When it comes to the orientation of the absorption and emission dipole moments in the dye molecules, it is usually aligned along the xanthene moiety in its plane, but various deviations have been reported.[110]

Another particular feature of RB and its derivatives is the ability to undergo intramolecular cyclization and lactone ring formation upon deprotonation of the carboxylic group.[111-113] Figure 1.12d shows the structural changes in the molecule as a result of such transformation. The extended π network shifts through the xanthene group, resulting in virtual disappearance of the strong absorption peak at 553 nm (Figure 1.12a). Its absorption spectrum is dominated by the three peaks at 309, 274 and 240 nm, with ε at 309 nm varying between 13700 and 16000 $cm^{-1}M^{-1}$ based on the solvent. Excitation at 230 nm results in the emission peak centered at 380 nm (Figure 1.12c).[111-113] Such property can be viewed as both a drawback and an advantage as the molecule loses its luminescence in the visible range, but at the same time it allows for a clear distinction between the two forms.

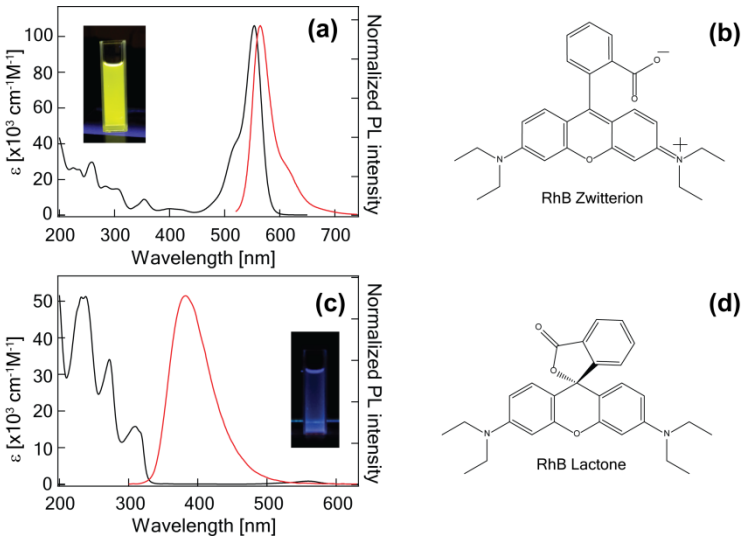

Figure 1.12. (a) Absorption (black) and PL (red) spectra of zwitterionic form of RB in water. (b) Molecular structure of RB cation. (c) and (d) show the same type of spectra and molecular structure but for the lactone form of RB in hexane. Insets in (a) and (c) show emission colors under the 254 nm UV lamp.

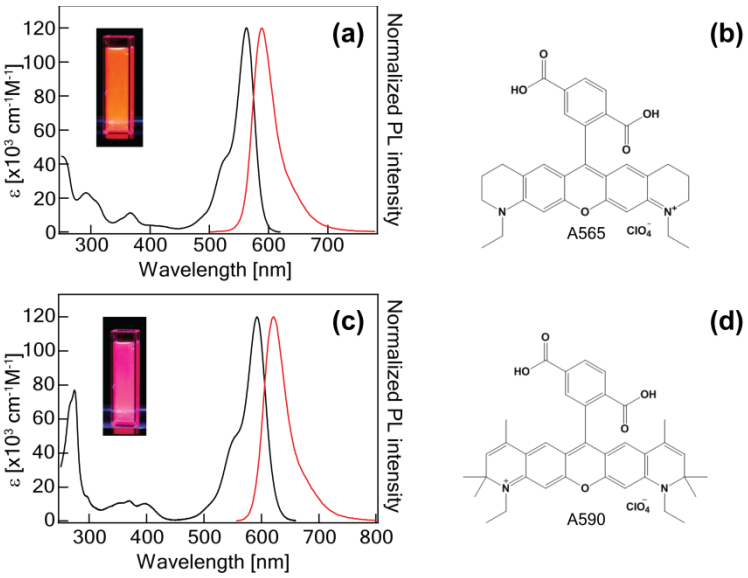

Figure 1.13. (a) Absorption (black) and PL (red) spectra of A565 in water. (b) Molecular structure of A565. (c) and (d) show the same type of spectra and molecular structure but for A590 in water. Insets in (a) and (c) show emission colors under the 254 nm UV lamp.

ATTO dyes like ATTO-565 (A565, Figure 1.13a and b) and ATTO-590 (A590, Figure 1.13c and d) can potentially be used as an alternative to RB based on their similar structures and properties. As stated by the manufacturer, these dyes are more stable with respect to the medium and other environmental factors, and have a high photo and thermal stability.[114] The properties of A565 and A590 are quite similar - molar extinction coefficient of 120000 $cm^{-1}M^{-1}$ in water or ethanol, QY of 80-90 %, lifetime of 3.7-4.0 ns and emission in the orange-red region.[114] Both A565 and A590 offer a potential expansion to the study of FRET in the TCO-dye conjugates and their increased stability could make them better candidates for the fabrication of WLED.

1.3.4 Project Outline

The main objective of the research project was the development and characterization of a single white-light emitting chromophore based on the Förster resonance energy transfer between the TCO nanoparticles and the organic dyes, and its application in the WLEDs. This project was aimed to further expand the recently reported data[115] by providing a more in-depth study of the FRET-mediated luminescence in the Ga_2O_3-RB hybrid nanoconjugates. A multitude of experiments were carried out using ultraviolet-visible (UV-vis) spectroscopy, steady-state, time-resolved and delayed PL measurements, time correlated single photon counting (TCSPC), and inductively coupled plasma (ICP) methods to analyze and characterize the synthesized hybrid nanoconjugates.

Previously, it was hypothesized that it should be possible to facilitate binding of the dye molecules to the surfaces of the NPs using solvents of different polarity.[115] It was expected that RB dissolved in water would displace surfactant ligands on the NC suspension in hexane. It was expected that all of the bound molecules would be luminescent in the orange range, while free RB would convert to RBL and not participate in the energy transfer. Such an approach would also allow the two forms of the dye to be distinguished easily. The degree of the spectral overlap and FRET efficiency could then be controlled through the NC size, donor-acceptor ratio or the use of a different dye.

As a starting model, a series of hybrid conjugates based on the γ-Ga_2O_3 NCs of variable sizes coupled with RB (Figure 1.14) were selected for the analysis. As-synthesized, NCs were treated with trioctylphosphine oxide (TOPO) and suspended in hexane, so they could maintain their emissive properties for a prolonged time. It was theorized that the relatively large size of the NCs would allow for their further surface modification by substituting some of the TOPO surfactant with the RB

molecules (Figure 1.14, right). An efficient non-radiative energy transfer from the Ga_2O_3 NCs to the dye molecules was expected to occur upon excitation in the UV range.

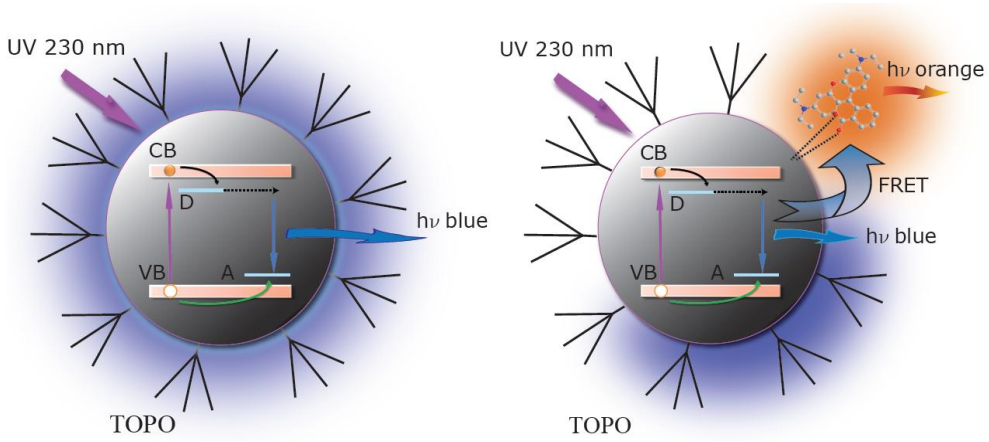

Figure 1.14. Proposed mechanism of emission in the Ga_2O_3 nanocrystals without (left) and with (right) RB molecules bound on the surface.

Variations in the NCs average size, number of the bound dye per NC or the type of the dye were used to control the degree of FRET and the resulting combined TCO-dye emission. Analysis of the chromaticity and the tunability of that emission formed the second objective of the research. Any suitable colloidal white-light-emitting samples were then expected to be subjected to the deposition on the UV LEDs for further analysis. It was hypothesized that such an approach would allow for an efficient emission of white light to occur by downconversion of the narrow UV radiation from the chip by the quasi-single TCO-dye hybrid nanoconjugates. Stability and overall performance of the resulting devices were not the subject of a detailed study at this time, and the WLEDs were expected to be used to demonstrate the proof of concept only. Based on the blue-orange color complementarity a series of ZnO-based nanostructures were also prepared and analyzed.

In order to analyze FRET in the Ga_2O_3-RB hybrid nanoconjugates, the number of the NCs in the sample was determined using ICP. Then ε of the bound RB in hexane was experimentally derived based on the UV-vis measurements. These parameters were then used to determine the donor-acceptor ratio, to calculate a more accurate spectral overlap integral and to derive the average FRET donor-acceptor distances. Both steady-state and time-resolved PL measurements were used to obtain the required data. Similar methodology was then applied to the Ga_2O_3-A590 nanoconjugates to supplement and verify the results obtained with RB. Additional control experiments were also

considered to determine the optimal starting dye concentrations and to analyze the binding efficiency. The second series of the objectives were directed toward the analysis of the chromaticity of the FRET-mediated emission. Both γ-Ga_2O_3 and ZnO were used as the sources of the blue luminescence for that purpose. RB, A565 and A590 were all applied as the energy accepting species to analyze the color matching of the chromophores, and the tunability of the emission. Surface deposition of the hybrid conjugates on the commercially available UV LEDs was then used to analyze the emission in the powder state.

As stated in Section 1.3.2 Equations 11-14 are suitable for a scenario representing one donor species interacting with one or *n* acceptors of the same type separated by a distance R_{DA}. Such approach provides a good analysis of the conjugates where the donor-acceptor ratio can be closely controlled, otherwise it gives a possible approximation, considering an average condition.[75,83,116-118] This is similar to the system proposed by Stryer and Haugland,[80] however, considering the use of NCs as the energy donors, such approach may not be entirely accurate. Generally if a donor NC has 15- 20 binding sites per acceptor, then the distribution of the bound dye will follow the Poisson statistic.[119] In that case the influence of the restricted geometry on FRET should be considered to provide better results for derivation of the FRET efficiency.[120-124] Under such conditions the energy transfer efficiency *E* is expressed as:[117,121]

$$E = \sum_{n=0}^{\infty} E(n)P(n) \qquad \text{(Equation 18)}$$

where *E(n)* is the energy transfer efficiency of the specific NC donors with *n* dye acceptors and *P(n)* is the probability of having *n* acceptors per one donor NC, expressed by the Poisson equation:[117,121]

$$P(n) = \frac{e^{-\lambda}\lambda^{n}}{n!} \qquad \text{(Equation 19)}$$

where λ is the mean number of the dye acceptors bound to each donor NC. Combining Equation 11 and 19 produces the relationship describing the observed energy transfer efficiency for a given heterogeneous system of donors and acceptors:[117,121]

$$E = \sum_{n=0}^{\infty} \frac{nR_0^6}{nR_0^6 + R_{DA}^6} \frac{e^{-\lambda}\lambda^{n}}{n!} \qquad \text{(Equation 20)}$$

The above equation provides a more accurate analysis of FRET occurring in the hybrid conjugates comprised of QDs and dyes, rather than dye-dye pairs. Statistical distribution of acceptors plays an important role in extracting FRET parameters, but it can still be limited.[77] Other factors to consider

are approximation of the NCs as point dipoles, degree of mobility of the conjugated dye, and the determination of an accurate donor-acceptor ratio. Additional concerns may arise from the possibilities of undergoing charge transfer and interactions between the bound dye molecules at high binding concentrations. The preliminary evaluation of the TCO-dye hybrid nanoconjugates was carried out assuming a constant (average) NC size, κ^2 value of 2/3 and accounting for both the average and the statistical distribution of the dye molecules per NC. There are reports of estimating the possible value of κ^2,[125-127] but derivation of the parameter was not considered at this point.

Both statistical distribution and the average concentration of the dye was considered in calculations, with the latter being a more preferable fitting model. Dipole orientation factor was assumed to be 2/3, since it is commonly approximated as such for conjugates like dye-labeled QDs.[75,82,83,85] There are reports that bound dyes exhibit κ^2 closer to 4/3 when bound on the QDs,[127] however, a spherical NC may have a wide arrangement of the possible binding sites, as well as luminescent defects. Steady-state PL measurements were chosen for measuring FRET efficiency, since Ga_2O_3 NCs follow a complex recombination probability described by the DAP model.[97] It was understood that in this case additional processes could contribute to the PL quenching as well. At this stage it was decided to analyze the general trends for both Ga_2O_3-RB and Ga_2O_3-A590 hybrid conjugates and to propose directions for further investigation of FRET in such chromophores.

Chapter 2
Materials and Experimental Procedures

2.1 Materials

All reagents and solvents were used as purchased without further purification. Gallium acetylacetonate ($Ga(acac)_3$, 99.99 %) and gallium nitrate hydrate ($Ga(NO_3)_{3*}xH_2O$, 99.99 %) were purchased from Strem Chemicals. Oleylamine (OAm, 70%), tri-*n*-octylphosphine oxide (TOPO, 90 %), zinc acetate ($Zn(OAc)_2$, 99.99 %), [9-(2-carboxyphenyl)-6-diethylamino-3-xanthenylidene]-diethylammonium chloride (Rhodamine B, 90 %) and 6-(2,5(6)-dicarboxyphenyl)-1,11-diethyl-2,2,4,8,10,10-hexamethyl-2,10-dihydro-1*H*-pyrano [3,2-*g*:5,6-*g*'] diquinolin-11-ium perchlorate (ATTO 590, ≥ 90 %) were purchased from Sigma-Aldrich Co. Lithium hydroxide (LiOH, ≥98 %) and potassium hydroxide (KOH, ≥85 %) were purchased from Fisher Scientific. Both hexane and ethanol (HPLC grade) were purchased from Alfa Aesar.

2.2 Synthetic Procedures and Data Analyses

2.2.1 Synthesis of Ga_2O_3

The synthesis of colloidal Ga_2O_3 NCs was performed according to a previously reported method.[98] In a typical synthesis, 0.5 g $Ga(acac)_3$ and 7.0 g OAm were placed in a 100 mL three-necked round bottom flask. The temperature of the mixture was then increased to 80 ºC to completely dissolve the precursor. The solution was then degassed for about 5 minutes with continued stirring, and the reaction flask was then filled with argon. The size of the resulting NCs was controlled by the final reaction temperature (200-310 ºC) and a heating rate of ~3 ºC/min. The reaction mixture was kept at the desired temperature for 1 hour under argon with stirring and then gradually cooled down to room temperature (RT). By varying the reaction temperature, NCs with the average sizes of 3.3 - 5.8 nm were obtained. The final product was extracted with the addition of ethanol followed by centrifugation at 3000 rpm for 10 min; the washing step was repeated three times. The NCs were then capped with TOPO by adding ~2.5 g of melted TOPO and stirring the solution for 1 hour at 70 ºC. This step was followed by ethanol extraction and centrifugation repeated twice. QY of the synthesized NCs was determined using a previously outlined procedure,[128] and a solution of quinine bisulfate (QBS) in 1 N H_2SO_4 as a reference (QY = 0.55).[129]

2.2.2 Synthesis of ZnO

Colloidal ZnO nanocrystals were prepared at RT using a modified sol-gel method. In a typical synthesis, 367 mg of $Zn(OAc)_2$ were dissolved in 20 mL of ethanol to make up a 0.1 M solution. The solution was then refluxed at 70 ºC until the solid was dissolved and cooled down to RT. To facilitate formation of ZnO NCs, solution of either LiOH or KOH in ethanol were added to the dissolved Zn precursor. A 3:1 molar ratio of hydroxide to $Zn(OAc)_2$ was used to obtain smaller particles, while for larger NCs a 1:1 mixture was used. Basic solution was added slowly to the Zn(II) precursor and stirred for 1 hour. The resulting product was precipitated with either ethyl acetate or ether, followed by centrifugation at 3000 rpm for 10 minutes. The washing cycle was repeated 3 times. Finally, ZnO NCs were redispersed in ethanol and stored in the refrigerator. QY of the synthesized NCs was determined using a previously outlined procedure,[128] and a solution of quinine bisulfate (QBS) in 1 N H_2SO_4 as a reference (QY = 0.55).[129]

2.2.3 Determination of the Molar Extinction Coefficient of RB and A590 Bound to γ-Ga_2O_3

In order to collect data necessary to determine the molar extinction coefficient of the bound RB, a polar to non-polar bilayer solution approach was utilized. Stock solutions of 3.6 and 5.3 nm γ-Ga_2O_3 NCs were prepared based on the absorbance of 1.0 at 230 nm in hexane. Stock solution of RB in water was set to 1.0 μM based on the absorption at 553 nm. A series of samples were prepared in triplicate for each nanoparticle size by depositing 4 mL of stock RB solution and 6 mL of γ-Ga_2O_3 in hexane into a 20 mL glass vial to form a clear bilayer. All samples were allowed to bind for only 1 hour before the non-polar phase was extracted, sonicated for 1 minute, and followed by the instrumental analysis. In order to determine the molar extinction coefficient of RB bound on γ-Ga_2O_3 in hexane, the absorbance readings of RB in water were collected before and after binding. Any difference was correlated to the binding of the dye, in other words - all RB molecules no longer present in the water part were assumed to be bound on the surface of γ-Ga_2O_3 in hexane. The absorption of hexane part was then measured and the molar extinction coefficient at 560 nm was calculated based on the Beer-Lambert law ($A=\varepsilon cl$, where A is the absorbance, ε is the molar extinction coefficient, c is the concentration and l is the path length of light). A low starting RB concentration and a short binding time insured minimal interference from RBL during measurements. Additional samples of higher starting RB concentrations (3, 5 and 10 μM), as well as increased time of binding (4, 8 and 24 hours), were also used to monitor any possible changes in the molar extinction

coefficient. A similar procedure was carried out for A590 as well. All starting volumes and concentrations of the NCs were identical to RB, and the starting concentration of A590 was set to 2.5 μM. Sample measurements of the water and hexane portions were taken after 4, 6, 11 and 13 hrs.

2.2.4 Determination of the Number of γ-Ga_2O_3 Nanoparticles in the Stock Solutions

Ga_2O_3 NCs with the average sizes of 3.6 and 5.3 nm were selected for the ICP analysis to determine the Ga^{3+} ion content required to calculate the donor-acceptor ratio. Stock samples of 6 mL each were standardized using UV-vis spectroscopy and the absorbance reading of 1.0 at 230 nm. The solvent (hexane) was then evaporated from the vials and the total sample mass was determined to be 2.6 and 5.0 mg for the 3.6 and 5.3 nm NCs, respectively. These samples were then digested with *aqua regia* made with 4 parts concentrated HCL and 1 part concentrated HNO_3. Actual measurements were conducted at Chemisar Inc. in Guelph, Canada. Ga^{3+} ion content for the other NC sizes (4.1 and 5.0 nm) were estimated using the average of the two measurements. Concentration of Ga^{3+} in ppm was converted to the moles of Ga^{3+} ions and then to the number of Ga^{3+} ions in that sample. Then the number of Ga^{3+} ions per one nanocrystal was calculated with the following assumptions and considerations: particle size distribution was ignored and all of the particles were treated as having the average size, all of the NCs were assumed to be perfect spheres with the volume $V=4/3\pi r^2$, the possible defects were not accounted for, and the crystal structure was assumed to be a perfect spinel. Using the crystal cell parameters outlined previously,[102,103] volumes of the unit cell and a single nanoparticle were calculated together with the number of Ga^{3+} ions per one unit cell. Then number of the unit cells per one NC was derived, followed by the total number of Ga^{3+} ions per one NC. Finally, the number of Ga_2O_3 NCs in a given stock sample was estimated by dividing the total number of the Ga^{3+} ions by the number of Ga^{3+} ions found in one NC of a particular size.

2.2.5 Effects of RBL on the Photoluminescence of the Ga_2O_3 Nanocrystals in Hexane

Ga_2O_3-RB samples were prepared from water-hexane bilayer as previously outlined. In a typical sample 4 mL of the 7 μM RB solution was used in conjugation with 6 mL of the 3.6 and 5.3 nm stock Ga_2O_3 NCs (absorbance 1.0 at 230 nm) in hexane; samples were left for 6 hours to allow sufficient binding to occur. additionally, two samples of Ga_2O_3-RBL were prepared with the similar NCs. To do so, 15 μL of the stock RBL solution was added directly to the suspension of the 3.6 nm Ga_2O_3 NCs in hexane and sonicated for 10 seconds; for the 5.3 nm NCs a 50 μL volume of the same

stock RBL solution was added. All measurements were taken within 3 minutes after the addition of the RBL.

2.2.6 Determination of the FRET Parameters for the γ-Ga_2O_3-RB Hybrid Conjugates

In order to analyze the energy transfer efficiency and the donor-acceptor separations, four stock solutions of RB in water were prepared, having the concentrations of 2.13, 5.16, 7.20 and 10.40 μM. Colloidal suspensions of the Ga_2O_3 NCs with the average particle sizes of 3.6, 4.1, 5.0 and 5.3 nm were standardized based on the absorbance of 1.0 at 230 nm. A conjugate was formed by depositing 6 ml of the Ga_2O_3 stock solution on top 4 mL of each of the RB stock solution, forming a bilayer; each sample was left undisturbed for 6 hrs. After binding the non-polar phase was extracted and sonicated for 1 minute, followed by the instrumental measurements. A statistical analysis of the data was then carried out to measure the averages and the standard deviations for all parameters. Donor-acceptor ratio was calculated using the ICP data and the molar extinction coefficient of the bound dye, and reported as a number of the RB molecules per Ga_2O_3 NC for each size group. FRET efficiencies *E* for each of the samples were calculated using Equation 12. Spectral overlap integral *J* was calculated using Equation 9 and the Förster radius R_0 was calculated using Equation 10. Average FRET donor-acceptor distances were obtained using Equation 14. Analysis of the Ga_2O_3-A590 hybrid conjugates was carried out in a similar manner. For that purpose, five stock solutions of A590 were prepared. The starting concentrations were as follow: 2.17, 2.92, 5.00, 6.75 and 9.08 μM. Two additional samples with the starting concentrations of 6.25 and 10.24 μM were added to the series with the 5.3 nm Ga_2O_3 NCs. Samples were prepared as outlined above except the binding time was set to 24 hr. The rest of the data collection and analyses were carried out in the same way as for RB.

2.2.7 Chromaticity Analysis of the Colloidal Samples

To assess the chromaticity of the resulting emission four stock solutions of the Ga_2O_3 NCs were prepared based on the absorbance of 1.0 at 230 nm. Then three stock solutions of RB and A590 in water, and A565 in ethanol were prepared with the starting concentrations of 15.5, 8.3 and 24.7 μM, respectively.

Samples with RB and A590 were prepared using the water-hexane bilayer approach, where the starting concentration of the dye sample was set as a percentage of the stock solution in increments of 10 %. In other words, a 100 % sample would have a 15.5 μM RB starting concentration

and a 10 % sample only ~1.6 μM. Starting volumes were set to 4 mL and 6 mL for the dye and the Ga_2O_3 stock solutions, respectively. Binding times were set to 6 hrs for RB and 24 hr for A590. The CIE chromaticity coordinated and the CCT were determined based on the steady state PL spectra using the ColorCalculator software version 4.85 provided by Osram Sylvania, Inc.

A typical sample with A565 was prepared by the addition of 10 - 120 μL of the stock A565 solution in ethanol to 5.5 mL of the colloidal suspension of NCs in hexane. The total sample volume was set to 6 mL by the addition of the corresponding amount of hexane. A series of samples were prepared by changing the starting volume of the added dye solution in increments of 10 μL to a maximum of 120 μL. Vials were then sonicated for 1 hour and then left undisturbed for 5 hours, followed by the instrumental measurements and data analysis. Chromaticity analysis was carried out using the ColorCalculator software version 4.85 provided by Osram Sylvania, Inc.

A stock solution of ZnO nanoparticles (λ_{em} = 460 nm) was prepared based on the absorbance of 1.0 at 300 nm in ethanol. A series of stock dye solutions of RB, A565, and A590 in ethanol were prepared with the following respective concentrations: 32.7, 17.5 and 15.8. All samples were set to a total volume of 4 mL with 3.5 mL of the stock ZnO solution, 50-500 μL of the stock RB and 450-50 μL of ethanol. The amount of RB added was varied in the 50 μL increments. Samples were then mixed in the ultrasonic bath for 1 hour, followed by the instrumental measurements. Samples based on A565 and A590 were prepared in a similar way except the amount of the dye solution added was varied in the 10 μL increments and did not exceed 120 μL. Chromaticity analysis was carried out using the ColorCalculator software version 4.85 provided by Osram Sylvania, Inc.

2.2.8 Development and Characterization of the Prototype WLEDs

UV LEDs designated UVTOP255TO39FW and UVTOP300TO39FW were purchased from Sensor Electronic Technology, Inc. and used without additional modifications. The purchased LEDs had the emission wavelength maxima centered at around 255 nm and 300 nm and a flat top quartz surface. The top surface of the LEDs was initially cleaned with ethanol, followed by the sample deposition. A suitable white-light-emitting sample was deposited on the top surface of the LED in 20 μL portions, followed by air drying at RT. The deposition was regulated by periodical checks of the resulting emission by applying a voltage of 6.0-8.0 V. The actual amount of the deposited material was difficult to determine and actual sample thickness was unknown. Analysis of the emission was carried out in a dark room using Konica Minolta CL-500A illuminance spectrophotometer.

2.3 Instrumental Measurements

2.3.1 UV-Vis and PL Spectroscopic Measurements

All absorption measurements were performed on the Varian Cary 5000 UV-vis-NIR spectrophotometer in air at RT in a quartz cuvette with the path length of 1 cm. All PL measurements were performed with the Varian Cary Eclipse fluorescence spectrometer in air and at RT. Steady state PL measurements were collected over the range of 230 - 700 nm with both the excitation and the emission slit widths set to 5 nm. All measurements were carried out in a quartz cell with a 1 cm path length at the right angle geometry. Samples based on Ga_2O_3 were excited at 230 nm and the samples based on ZnO were excited at 300 nm.

2.3.2 Time-Resolved Photoluminescence Measurements

Time gated fluorescence decay measurements were taken on the Varian Cary Eclipse fluorescence spectrometer in air and at RT. In a typical experiment the delay and gate times were set to 3 μs and 1 μs respectively. Both the excitation and emission slit widths were set to 10 nm. All measurements were carried out in a quartz cell with a 1 cm path length at the right angle geometry. Intensity was monitored at the emission peak maxima. Fitting of the resulting decay curves was done with multi-exponential fitting scripts using OriginPro 8.5.0 SR1 software package.

All TCSPC measurements were obtained with the IBH Ltd. time-resolved fluorometer equipped with the IBH 563 nm NanoLED excitation source located at the University of Waterloo (Waterloo, Canada). All samples were placed in a 1 cm x 1 cm quartz cuvette and excited at 565 nm with the right angle geometry. The resulting fluorescence was monitored at the maximum of the emission bands, which were determined to be 575 nm for RB and 620 nm for A590. Both excitation and emission slits were set to 16 nm. All TCSPC decays were acquired over the range of 1024 channels using a 1 MHz repetition rate and 0.059 ns/channel. The maximum intensity for the channel was 20000 counts for both the instrument response function (IRF) and the decay curves. To obtain the IRF a Ludox solution was used. An iterative reconvolution method was employed to analyze all decays using IBH DAS 6.2 software. An experimental curve was fit with a program generated curve, which was convoluted numerically with the IRF. All of the collected decay curves were fitted independently with either a mono- or a multi-exponential equation, and the goodness of fit was assessed with the reduced χ^2 values (0.9-1.2) and the overall randomness of the weighted residuals.

Chapter 3
Characterization of the Distance-Dependent FRET in the TCO-Dye Chromophores

3.1 Characterization of the FRET Donor Nanoparticles

A series of gallium oxide (Ga_2O_3) colloidal nanocrystals (NCs) were synthesized as described in Section 2.2.1 using temperature as the primary means of controlling the particle size. Figure 3.1a shows XRD patterns of the NCs synthesized at different temperatures. All patterns are well matched to the reference pattern of γ-Ga_2O_3 (vertical black lines, JCPDS 20-0426), which is a metastable phase of Ga_2O_3. We have recently demonstrated that metastable phases of the transparent metal oxide NCs can be stabilized in situ during NC synthesis by controlling their sizes and growth kinetics, owing to the surface energy and surface stress contributions.[98-100] Overview transmission electron microscopy (TEM) image of the typical Ga_2O_3 NCs synthesized at 310 °C is shown in Figure 3.1b as an example. These nanocrystals have nearly ideal spherical morphology with an average size of 6.0±1.1 nm. The average sizes of the NCs in the samples synthesized at different temperatures were determined from the corresponding TEM images. All NCs form clear colorless suspensions in the nonpolar organic solvents.

Figure 3.1c shows PL emission (shaded area) and excitation spectra (dashed lines) overlaid with the corresponding absorption spectra (solid lines) for the Ga_2O_3 NCs of four different sizes used in the experiments described in this work. Absorption and excitation spectra show virtually no change for different NC sizes, indicating an insignificant quantum confinement effect. This can be attributed to a relatively large effective electron mass and a tight exciton binding in Ga_2O_3. Importantly, the PL spectra in Figure 3.1c exhibit a large shift, which can be attributed to the localized nature of the recombining electrons and holes within the NC band gap. The PL of Ga_2O_3 originates from the recombination of an electron trapped on a donor with a hole trapped on an acceptor state, where the donor is an oxygen vacancy site and the acceptor could be either a gallium vacancy or gallium-oxygen vacancy pair. This mechanism is known as the donor-acceptor pair (DAP) recombination, and to avoid the confusion with the donor and acceptor species associated with FRET, hereinafter I refer to this process simply as a defect trap emission. Previously reported temperature-dependent PL measurements and theoretical analysis suggested that a blue shift of the γ-Ga_2O_3 NC emission with

decreasing NC size, evident in Figure 3.1c, arises from an increase in the Coulomb interactions between charged defect sites involved in the DAP recombination.[97] Figure 3.1d shows the color of the DAP emission for different average NC sizes, covering the entire blue range of the visible spectrum.

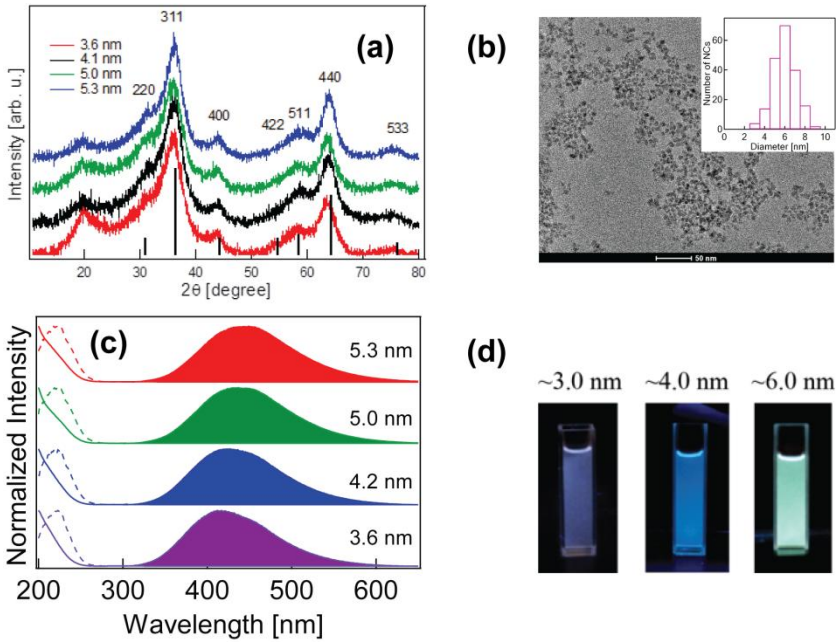

Figure 3.1. (a) Powder XRD patterns for the Ga_2O_3 NCs having various particle sizes, corresponding reference peaks are also indicated as black vertical lines. (b) TEM image of the Ga_2O_3 NCs synthesized at 310 °C having an average size of ~6.0 nm (scale bar, 50 nm), overall size distribution is shown in the histogram (inset). (c) UV-vis (solid line), PL excitation (dashed line) and steady state PL (shaded area) spectra of the Ga_2O_3 NCs of various sizes. (d) Emission of the colloidal Ga_2O_3 samples under the excitation with a 254 nm UV lamp.

The PL decay rate also shows a strong dependence on the average NC size (Figure A1 in the Appendix). The rate of the PL decay increases with decreasing NC size, which is associated with the accompanying decrease in the defect separation. The trap emission dynamics in this system is not governed by the recombination probability, but rather by the rate of the electron transfer between relevant defect sites (from an electron donor to an acceptor site) as the rate-determining step.[97,99,100] As a consequence, this emission persists on a millisecond time scale, and can be used as an important parameter for the characterization of the hybrid nanoconjugates described in this thesis. The key NC parameters obtained for various Ga_2O_3 NCs used in this work are presented in Table 3.1.

Table 3.1. Summary of the data extracted from the absorption, emission, and PL decay analyses of the Ga_2O_3 NCs of variable average sizes.

Temperature of synthesis [°C]	NC diameter [nm]	Emission maximum [nm]	QY* [%]	Lifetime [μs]	Concentration of NCs [mL^{-1}]**
210	3.6	420	15.1	4.80	$4.92x10^{14}$
240	4.1	430	14.0	5.13	$3.14x10^{14}$
270	5.0	440	12.1	5.36	$1.72x10^{14}$
300	5.3	450	13.2	5.52	$1.38x10^{14}$

*determined using a solution of quinine bisulfate (QBS) in 1 N H_2SO_4 as a reference[128,129]

** determined as described in Section 2.2.4

To examine the generality of our approach for generating white light, I also prepared dye-conjugated ZnO NCs. ZnO NCs were synthesized in ethanol at room temperature, as described in Section 2.2.2. The average sizes of nanocrystals were estimated to be between 3.0 and 6.0 nm, depending on the amount of the hydroxide added to the reaction mixture. The absorption and emission spectra of the ZnO NCs having different average sizes are shown in Figure 3.2. The particles were found to have a broad emission range and a relatively high quantum yield of 9-10 %.

The main focus of this work was to examine how the NC parameters presented in Table 1 can be used to generate and control white light emission in the NCs conjugated with organic fluorophores emitting a complementary color.

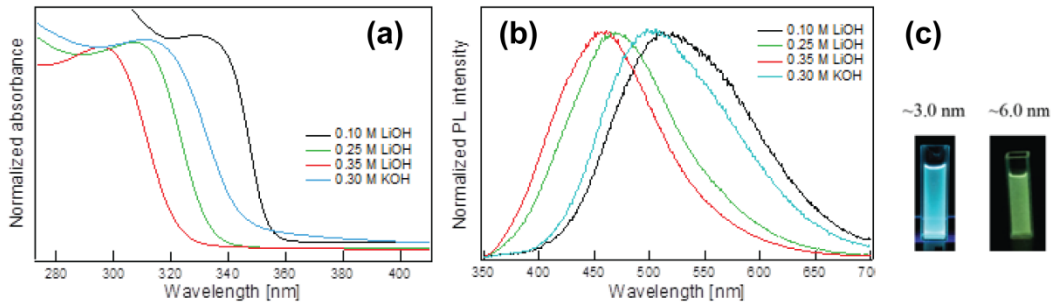

Figure 3.2. (a) Absorption spectra of the ZnO nanocrystals of various sizes (3.0 - 6.0 nm). (b) PL spectra of the same samples, excited at the corresponding absorption maxima. (c) Emission color of the colloidal 3.0 and 6.0 nm ZnO nanoparticles under the excitation with a 254 nm UV lamp.

3.2 Detection and Characterization of FRET in the Ga_2O_3-RB and Ga_2O_3-A590 Hybrid Nanoconjugates

A proposed mechanism of white light generation by energy transfer in the hybrid RB-conjugated Ga_2O_3 NCs is shown in Figure 1.14 (Section 1.3.4). We chose RB dye as a model FRET acceptor that exhibits a strong orange-red PL (Figure A2) with a minimal absorption in the Ga_2O_3 NC (FRET donor) excitation range (ca. 230 nm). The absorption band, arising from π to π^* ($S_0 \rightarrow S_1$) transition, provides a significant overlap with the blue emission of the Ga_2O_3 NCs (Figure A2g), enabling the conditions for the FRET mechanism. Another important feature which makes RB a good model system for this study is its ability to undergo lactone ring formation (RBL) upon deprotonation of the carboxyl group, as stated in Section 1.3.3. Such transformation causes a change in the electronic structure, which allows for the spectroscopic differentiation between the NC-bound RB and its free RBL counterpart. While RB can bind through the carboxyl group to the NCs dispersed in hexane or toluene, any solvated molecules in such non-polar solvents exist in the lactone form, which is distinctly non-emissive in the orange-red (Figure A2b), and does not undergo resonance energy transfer.

Figure 3.3a shows an increase in the PL decay rate of the Ga_2O_3 NC trap emission as a result of binding of RB, which is one of the common characteristics of FRET. The average lifetimes of the NC defect trap emission for different concentrations of RB estimated from fitting the corresponding PL decay curves are given in Figure A3 and Table A1 (Appendix). The change in the PL decay rate of the NC trap emission upon binding of the molecular dyes as energy acceptors appears to diminish with decreasing NC size. The DAP mechanism described above depends on the distribution and separation of defect sites which are, in turn, dependent on the NC size.[97,99] A possible explanation is that a sufficient decrease in the NC size and the corresponding increase in the near-surface defect concentration could lead to the formation of a donor-acceptor complex involving a hole trapping defect (where the NC DAP recombination occurs) and an adsorbed dye molecule. The energy transfer within this

complex-like structure could result in prompt and complete quenching of the NC PL, similarly to the static quenching mechanism.[130,131]

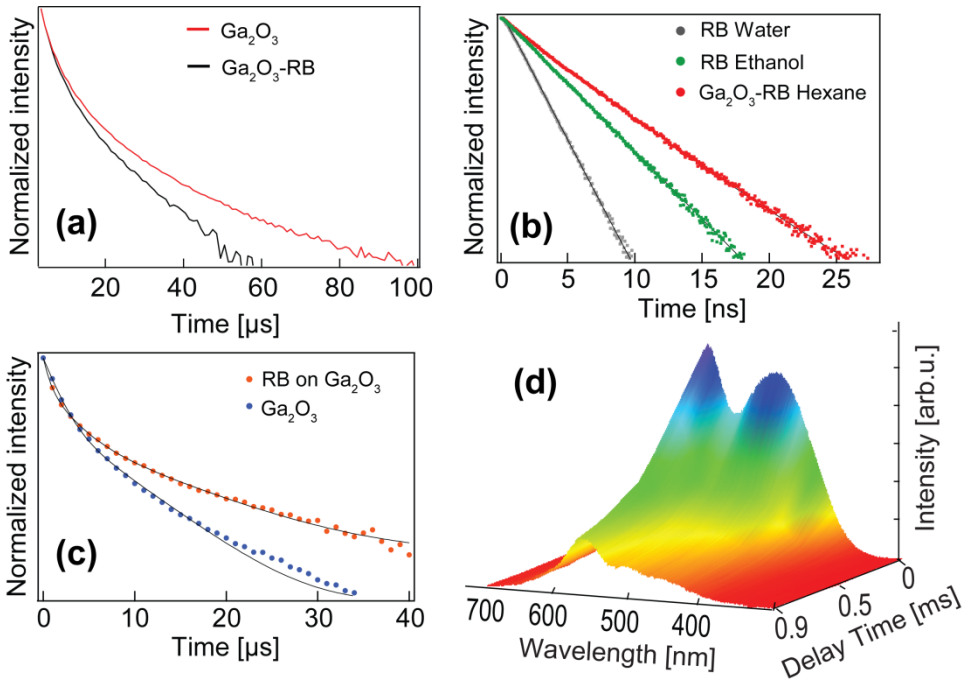

Figure 3.3. (a) Donor Ga_2O_3 NC PL decay curves before and after binding of RB to the 5.3 nm NCs (λ_{ex}, 230 nm; λ_{em}, 450 nm). (b) Normalized PL decay profiles of the free RB molecules in water, ethanol, and RB bound to the 3.6 nm Ga_2O_3 NCs in hexane (λ_{exc}=563 nm; λ_{em} = 575 nm). (d) Normalized PL decay curves of the same sample of the bound RB (red dots) and the 3.6 nm Ga_2O_3 NCs (blue dots) upon excitation at 230 nm. (c) Time-gated PL spectra of the 5.3 nm Ga_2O_3-RB hybrid conjugate in hexane shown as a function of the delay time (0.1, 0.3, 0.5, 0.7, and 0.9 ms), gate time was 5 ms and λ_{exc} = 230 nm. Fitting parameters can be found in Table A2.

Dye molecules also experience profound changes in the emission lifetime upon binding to the NC surface. The inherent lifetime of the RB PL directly excited into $S_0 \rightarrow S_1$ transition increases upon binding to the NC surface (Figure 3.3b), indicating a reduction in the non-radiative relaxation due to the restricted molecular motion. When the same Ga_2O_3-RB nanoconjugate was excited at 230 nm (sensitized emission), the corresponding RB PL

lifetime extended from ca. 3.5 ns to over 5 μs, resembling the PL decay dynamics of the Ga_2O_3 NCs (Figure 3.3c). In this configuration the excitation of RB was governed by the DAP recombination of the Ga_2O_3 NCs as result of FRET. Consequently, the afterglow of the NC-bound RB is also observed upon excitation at 230 nm, even after a delay of ca. 0.9 ms (Figure 3.3d). A590 displayed similar behavior having its inherent emission lifetime of ca. 4 ns extended to ca. 6.2 μs upon conjugation, as a result of the energy transfer from the Ga_2O_3 NCs photoexcited at 230 nm (Figure A4a and b, Table A2). Emission from A590 was also detected after a delay of 0.9 ms upon excitation at 230 nm similarly to the NC-bound RB (Figure A4c). These results indicate an efficient non-radiative energy transfer from the Ga_2O_3 NCs to the bound dye molecules, leading to a characteristic blue-orange emission.

To confirm that the observed FRET is associated with binding of RB to the Ga_2O_3 NCs rather than a simple proximity effect, a series of Ga_2O_3 NC suspensions were treated with RB by water-hexane transfer and by direct addition of the free RBL. Figure 3.4a and b shows the absorption and PL spectra, respectively, of the 3.6 nm Ga_2O_3 NC suspensions containing similar amounts of RB in the bound (green) and lactone (black) forms. Upon excitation into the Ga_2O_3 band gap we observed a decrease in the donor emission by ~ 40 % for Ga_2O_3-RB nanoconjugate accompanied by the appearance of the acceptor emission (Figure 3.4b, green). On the other hand, the donor NC trap emission decreases by less than 8 % in the presence of RBL, while the corresponding acceptor emission is virtually absent (Figure 3.4b, black). This observation suggests that free RBL in solution cannot accept excitation energy from the Ga_2O_3 NCs and generate a sufficient orange emission observed for the Ga_2O_3-RB nanoconjugates. A small decrease in the donor emission for the colloidal sample containing RBL is due to a small fraction of the light source associated with the direct excitation of RBL or minor collisional quenching. Similar results are obtained for other NC sizes and dye molecule concentrations (Figure A5). Taken together, these results indicate that energy transfer in the Ga_2O_3-RB nanoconjugates occurs as a result of binding between the NCs and dye molecules.

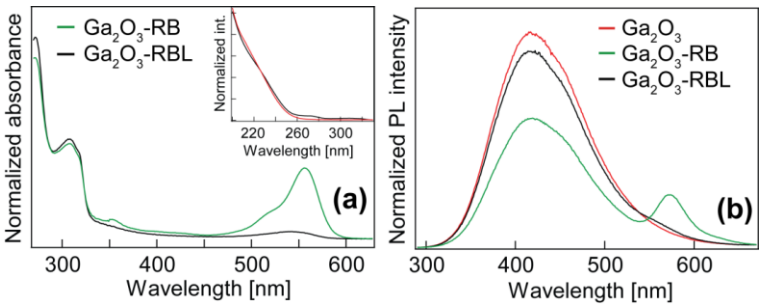

Figure 3.4. (a) Absorption spectra of the hexane suspensions of the 3.6 nm Ga_2O_3 NCs ($4.92x10^{14}$ NCs/mL) containing RBL (black) and bound RB (green) in similar concentrations (ca. 2.7 μM). Inset: normalized absorption spectra of the 3.6 nm Ga_2O_3 NCs (red) and Ga_2O_3-RB hybrid nanoconjugates centered around the excitation wavelength (230 nm). (b) PL spectra of the same two samples after excitation at 230 nm; red spectrum denotes emission of the 3.6 nm Ga_2O_3 NCs with no dye.

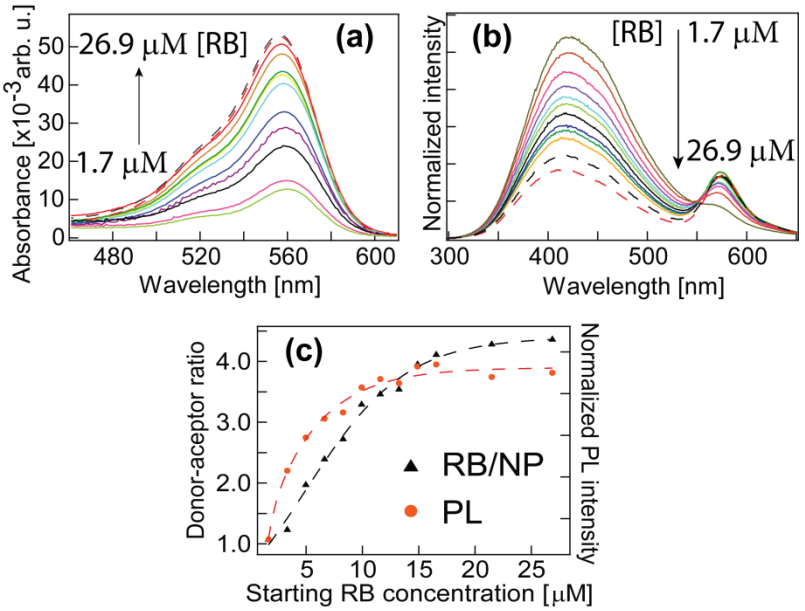

Figure 3.5. Analysis of binding of RB to the surface of the 3.6 nm Ga_2O_3 NCs based on the starting RB concentration. [Ga_2O_3] - $4.92x10^{14}$ NCs/mL, [RB] - 1.65, 3.31, 4.96, 6.62, 8.27, 9.92, 11.58, 13.24, 14.89, 16.55, 21.49, and 26.87 μM. UV-Vis (a) and PL (b) measurements of the Ga_2O_3-RB samples taken in hexane after 6 hours of binding (λ_{ex} = 230 nm). (c) Resulting acceptor to donor ratio (RB/NP) and PL intensity expressed as a function of the RB starting concentration; dashed curves represent fitting curves used for visual enhancement and guidance.

To further analyze the binding of RB to the surfaces of the NCs, a series of samples were prepared with varying RB concentrations (Figure 3.5a). By monitoring the increase in the absorption and PL intensity of the dye molecule with increasing starting concentration (Figure 3.5a and b), it is found that the binding saturation occurs at a starting RB concentration of 13-15 μM (figure 3.5c), which corresponds to 3-4 RB molecules per NC on average. Upon further increase in the concentration of the dye, the excess molecules would simply exist in hexane as RBL. To avoid interference from RBL, it was decided to limit the starting RB concentration to 10 μM.

A590 is structurally similar to RB, but its emission is red-shifted relative to that of RB (Figure A2). This difference allows us to systematically investigate the influence of the spectral overlap integral on the efficiency of the energy transfer and other FRET parameters, providing the opportunity to further tailor and manipulate the chromaticity and other properties of the resulting emission. To quantify the influence of the spectral overlap on the FRET parameters, we first estimated the extinction coefficients (ε) of the dyes bound to the Ga_2O_3 NCs dispersed in hexane. Binding was accomplished using low concentrations of dyes in aqueous solutions to minimize the presence of the free molecules in hexane phase, as described above, and in Section 2.2.3. Under those conditions the difference in absorbance of the dye molecules in water before and after their transfer to the hexane dispersion of NCs (Figure A6) largely corresponds to the amount of the dye molecules bound to the NCs. By correlating the amount of the dyes, transferred to the hexane phase, to the corresponding absorbance measurements we estimated the ε values of the bound RB and A590 to be 11533±377 and 31534±130 $cm^{-1}M^{-1}$, respectively. These values are significantly different from the ones obtained for the free molecules in aqueous solutions reported in Section 1.3.3. Although the organic dyes bound to the NCs are often assumed to have the same extinction coefficients as those in the free form, these results show that they indeed experience dramatic changes upon binding.

Spectral overlap integral J is a key parameter for controlling FRET and is directly determined by the molar extinction coefficient of the acceptor. The magnitude of J determines the critical distance R_0 (or Förster distance) at which the energy transfer efficiency (E) is 50 %. Using Equations 9 and 10 (Section 1.3.2), we obtained the values of J

and R_0 for Ga_2O_3-RB and Ga_2O_3-A590 hybrid nanoconjugates (Table 3.2). In these calculations, we approximated dipole orientation factor κ^2 to 2/3, which is reasonable considering a random distribution of both NC defects and the binding sites on the NC surfaces.[75,83] Even though A590 absorption band is red-shifted compared to RB, and therefore has a smaller spectral overlap with Ga_2O_3 NC PL band, its higher ε results in a longer critical distance, rendering A590 a more effective energy acceptor. Furthermore, higher quantum yield of the NC-bound A590 (81 %) relative to RB (27 %) makes Ga_2O_3-A590 conjugate a more efficient white light-emitting nanophosphor. Spectral overlap integral for a given dye molecule increases with increasing NC size, owing to the red shift of the NC trap emission, and results in the overall longer R_0 for larger NCs.

Table 3.2. FRET parameters for Ga_2O_3-RB and Ga_2O_3-A590 hybrid conjugates prepared from the different NC sizes.

NP size [nm]	Rhodamine B		ATTO-590	
	J [x10^{13}cm^{-1}M^{-1}nm^4]	R_0 [nm]	J [x10^{13}cm^{-1}M^{-1}nm^4]	R_0 [nm]
3.6	8.01	2.41	9.19	2.47
4.1	8.95	2.43	11.86	2.54
5.0	11.00	2.45	15.67	2.60
5.3	12.10	2.51	18.00	2.68

In contrast with the typical semiconductor QD energy donors that exhibit excitonic emission, FRET efficiency in the dye-conjugated Ga_2O_3 NCs is determined not only by the NC size but also by the distribution of the native defects in the NCs. PL of the Ga_2O_3 NCs occurs when an electron trapped in an oxygen vacancy defect state just below the bottom of the conduction band undergoes tunnel transfer to an electron acceptor site (usually described as Ga-O vacancy pair), where it recombines with a trapped hole.[97] The energy donor-acceptor separation (R_{DA}) therefore reflects an average distance between the hole-trapping sites as FRET donors and dyes conjugated on the NC surfaces as FRET acceptors. In order to analyze the energy transfer efficiency and donor-acceptor distances in Ga_2O_3-RB and Ga_2O_3-

A590 conjugates we prepared a series of samples with the variable starting concentrations of the dyes. The energy transfer efficiency E was determined from the steady-state PL data, however, E can also be expressed through the relationship to R_0 and the average donor-acceptor separation R_{DA}:

$$E = \frac{nR_0^6}{nR_0^6 + R_{DA}^6} \qquad \text{(Equation 21)}$$

where n is the number of the acceptors bound to a single donor. This average approximation generally works well for the NC-dye conjugates when the stoichiometric ratio of the donor and acceptor can be controlled, or if all binding sites are predominantly occupied.[75,83,118] It has also been indicated that for the NC-dye conjugates with $R_{DA}>R_0$, Equation 21 provides an accurate estimate of the donor-acceptor distances.[118] If the number of the bound acceptor species is small compared to the number of the possible binding sites (such as 1 acceptor per 20 binding sites), then the distribution of the acceptors per donor NC will obey the Poisson statistics as discussed in Section 1.3.4, and Equation 20 should be used instead.[116,119,122] To estimate the average donor-acceptor distance, Equation 14 was used, and the obtained R_{DA} values were applied for all subsequent data fitting.

The values of n were determined from the number of the NCs in a stock suspension for a given average size (Table 3.1) and the number of the conjugated dye molecules based on their ε values in the bound form, exactly as outlined in Section 2.2.4. This n value represents the upper limit given the possibility of detachment and solvation of some NC-bound dye molecules. By changing the starting concentration of RB from ~ 2 to 10 μM, the average surface coverage of the 3.6 nm Ga_2O_3 NCs varied from 1.0 to 3.3 molecules per NC (Figure 3.6a and Table 3.3).

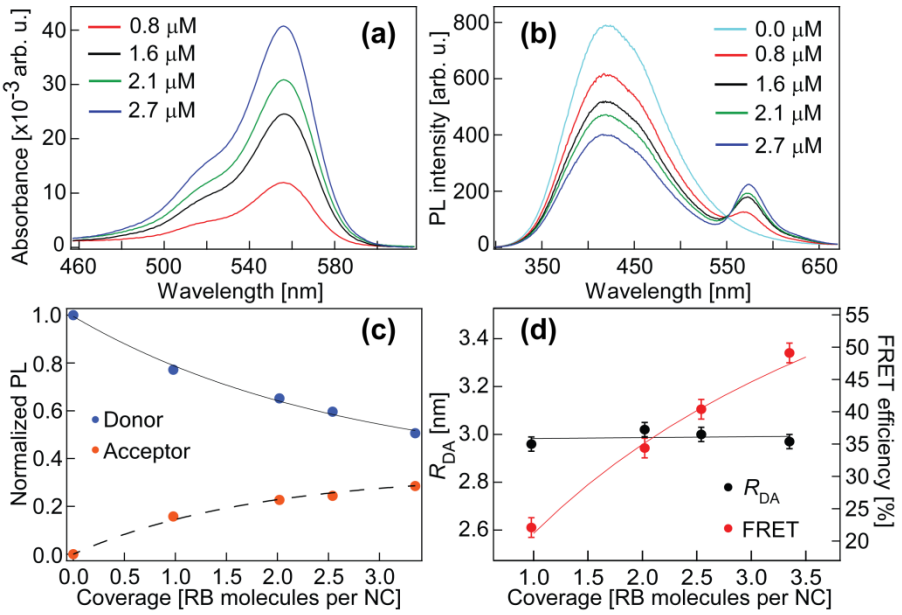

Figure 3.6. (a,b) Absorption (a) and PL (b) spectra of the 3.6 nm Ga_2O_3-RB hybrid conjugates with the variable concentration of the bound RB (0.8 - 2.7 μM). Concentration of the Ga_2O_3 NCs was set to 4.92×10^{14} NCs/mL for all samples, and the excitation wavelength in all cases was 230 nm. (c) Normalized PL intensities of the donor Ga_2O_3 NCs and the acceptor RB molecules as a function of the donor-acceptor ratio *n*. (d) Variations in the FRET efficiency and the donor-acceptor separations as a function of *n*. Solid lines in (c) and (d) show the fits obtained with the corresponding equations, as described in the text; dashed line in (c) is used as a guide to the eye.

Table 3.3. Summary of the FRET parameters extracted from the steady-state PL data for the 3.6 nm Ga_2O_3-RB hybrid nanostructures with the variable surface dye coverage.

Bound RB [μM]	Coverage [RB per NC]	FRET efficiency [%]	R_{DA} [nm]
0.8	1.0	22	2.96
1.6	2.0	34	3.02
2.1	2.5	40	3.00
2.7	3.3	49	2.97

Variation in the dye coverage allows us to control the spectral density distribution by controlling the probability of the sensitized emission of the acceptor via energy transfer (Figure 3.6b). Figure 3.6c plots the relative PL intensities of the Ga_2O_3 NCs (blue dots) and RB (red dots) from Figure 3.6b, as a function of the number of RB molecules per NC. With increasing surface coverage (or RB-to-NC ratio), the NC emission is gradually quenched, which is accompanied by a nearly symmetric increase in the RB emission intensity, consistent with the FRET mechanism. A decrease in the donor and an increase in the acceptor emission intensities level off at high values of the surface coverage in Figure 3.6c, indicating that the maximum surface coverage for the 3.6 nm diameter NCs is attained for approximately three RB molecules per NC. The data for quenching of the PL intensity of the donor were fit using a combination of Equations 12 and 21, and expressing F_{DA}/F_D as a function of n. Data for the FRET efficiency and the donor-acceptor separation with respect to the surface coverage are shown in Figure 3.6d. These data were fit with Equation 21, assuming average coverage (Figure 3.6d) and Equation 20, accounting for a possible statistical distribution of RB (Figure A7). Both equations provide a good overall fit to the experimentally obtained data points for all sample series. The applicability of the average approximation represented by Equation 21 is likely associated with the relatively small number of the binding sites due to the small size of the NCs and the bulkiness of the dye molecules. The energy transfer efficiency gradually increases from 22 to 49 % with increasing RB/NC ratio, while calculated R_{DA} values are nearly constant. The constant R_{DA} for the different surface coverage reflects largely a random distribution of the defect sites and the dye molecules on the NC surfaces. Additional analysis of the Ga_2O_3-RB conjugates for the 5.3 nm NCs produced similar results (Figure 3.7 and Table 3.4). Hybrid conjugates based on the 4.1 and 5.0 nm Ga_2O_3 NCs also displayed similar trends (Figure A8/Table A2 and Figure A9, Table A3, respectively). Increase in the average NC size resulted in more RB molecules per NC, facilitating a more efficient FRET, while at the same time leading to longer estimated donor-acceptor distances.

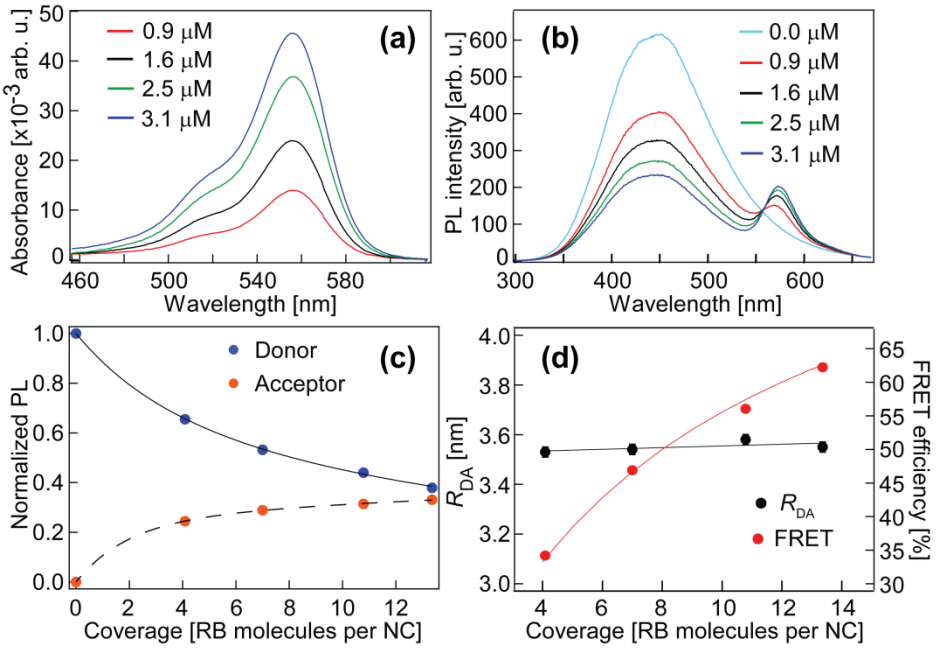

Figure 3.7. (a) Absorption and (b) PL spectra of the 5.3 nm Ga_2O_3-RB hybrid conjugates with the variable donor-acceptor ratio, determined from the concentration of the bound RB shown in the graph (0.9 - 3.1 μM). Concentration of the Ga_2O_3 NCs was set to 1.38×10^{14} NCs/mL for all samples, and the excitation wavelength in all cases was 230 nm. (c) Normalized PL intensities of the donor Ga_2O_3 NCs and the acceptor RB molecules as a function of the donor-acceptor ratio *n*. (d) Variations in the FRET efficiency and the donor-acceptor separations as a function of *n*. Solid lines show fits obtained with the corresponding equations, as described in the main text. Dashed line in (c) is a guide to the eye. Error bars in (d) are smaller that the size of the data points.

Table 3.4. Summary of the FRET parameters extracted from the steady-state PL data for the 5.3 nm Ga_2O_3-RB hybrid nanostructures with the variable surface dye coverage.

Bound RB [μM]	Coverage [RB per NC]	FRET efficiency [%]	R_{DA} [nm]
0.9	4.1	34	3.53
1.6	7.0	47	3.54
2.5	10.8	56	3.58
3.1	13.4	62	3.55

A series of the Ga_2O_3-RB nanoconjugate samples prepared with the different NC sizes and having a 3:1 RB-to-NC ratio were prepared to quantify the efficiency of the energy transfer and the corresponding donor-acceptor distances as a function of the NC size. Figure 3.8a plots the spectral overlap integral (left ordinate) and the donor-acceptor separation (right ordinate) as a function of NC size. Both quantities display a linear dependence as expected for the FRET mechanism. Given the unique nature of the energy donors in the Ga_2O_3 NCs described above, the increase in the R_{DA} with increasing NC size is a consequence of the two cooperating phenomena: *i*) smaller defect density in the larger NCs owing to their lower surface-to-volume ratio and higher synthesis temperature, as demonstrated in our previous studies,[97,99] and *ii*) reduced surface density of RB for the same number of the molecules per NC. In addition to the observed increase in the R_{DA}, increasing the NC size also results in a longer R_0 due to the enhancement in the spectral overlap. Figure 3.8b shows FRET efficiency, calculated using Equation 12, as a function of J integral. Surprisingly, the data in Figure 3.8b are well represented by a straight line with a negative slope. This seemingly counterintuitive trend can be associated with the fact that the conjugates involving smaller NCs tend to have shorter donor-acceptor distances as indicated in Figure 3.8a. Considering a similar acceptor-to-donor ratio for all NC sizes, the likelihood of a dye molecule residing in the immediate vicinity of the defect site acting as the FRET donor increases with decreasing NC size. Overall comparison of all sample series revealed a nearly constant value of R_{DA} with respect to the FRET efficiency (Figure 3.8c) which is governed by the RB:NC ratio. The results of this analysis are summarized in Table 3.5. These results quantitatively describe the control of the FRET parameters involving NC defect states. Controlling the efficiency of the energy transfer via various FRET parameters is crucial for generating the desirable emission spectrum, chromaticity, and the color temperature. It can be achieved through variations in the average NC size and manipulation of the configuration and number of the acceptor dye molecules with respect to the donor NC.

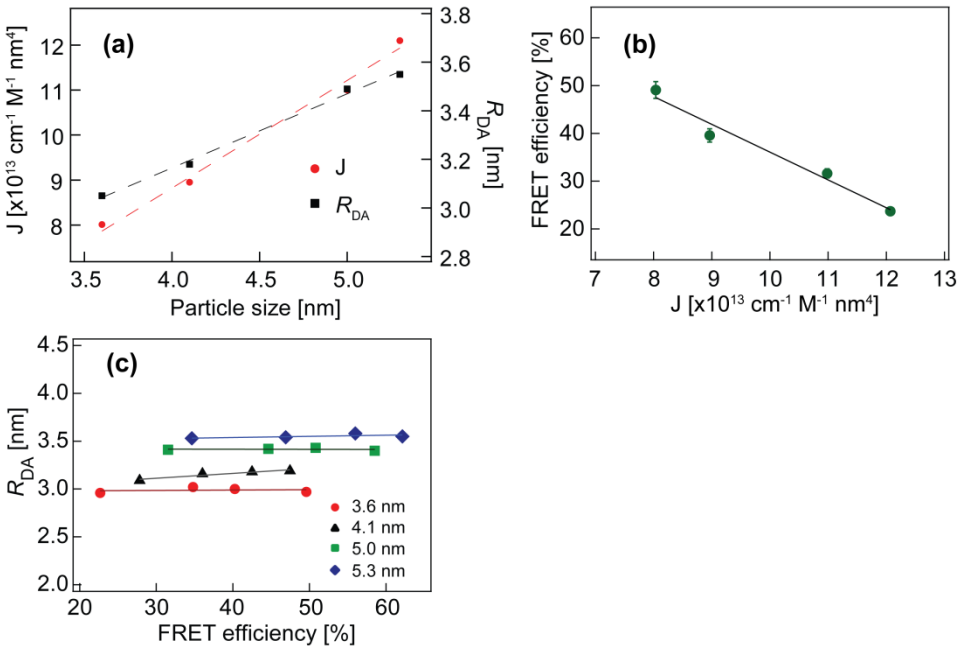

Figure 3.8. Summary of the FRET analysis for the Ga_2O_3-RB hybrid nanoconjugates. (a) Spectral overlap integral (J) and the average donor-acceptor separation (R_{DA}) values with respect to the average NC size. (b) FRET efficiency as a function of J for the Ga_2O_3-RB nanoconjugates prepared using different average NC sizes with a similar RB to Ga_2O_3 NC ratio (3:1). (c) Variation in the R_{DA} as a function of the FRET efficiency governed by the number of the bound RB molecules in the Ga_2O_3-RB conjugates prepared using different average NC sizes.

Table 3.5. Summary of the FRET parameters extracted from the steady-state PL data for the samples of the Ga_2O_3 NCs with similar RB surface coverage for the primary NC size groups.

Particle size [nm]	R_0 [nm]	Coverage [RB per NC]	FRET efficiency [%]	R_{DA} [nm]
3.6	2.41	3.3±0.1	49.5±1.5	2.97±0.05
4.1	2.43	3.2±0.1	40.2±1.1	3.16±0.02
5.0	2.45	3.3±0.2	32.4±0.6	3.41±0.01
5.3	2.51	3.1±0.1	24.0±0.0	3.67±0.00

To gain further insights into FRET in this type of hybrid white light-emitting nanoconjugates, we conducted a similar set of experiments for the Ga_2O_3-A590 system. Considering the structure and properties of A590 (Figure A2), similar trends were expected for FRET efficiency and the donor-acceptor separations to those observed for the Ga_2O_3-RB system. Figure 3.9 shows the results for the Ga_2O_3-A590 nanoconjugates based on the 3.6 nm NCs having a variable A590 surface coverage. Intensities of the A590 absorption peaks in Figure 3.9a indicate a relatively small amount of the A590 molecules bound to the NCs, which could be related to the lower binding affinity of A590 compared to RB. The highest A590/NC ratio for the 3.6 nm Ga_2O_3 NCs was determined to be 0.8, even after a 24 hour binding period (Table 3.6). As a result, weaker donor emission quenching and a lower intensity of the sensitized acceptor emission were observed relative to the Ga_2O_3–RB (Figure 3.9b), although they exhibit a similar symmetric behavior (Figure 3.9c). The maximum FRET efficiency was found to be ca. 26 % even for the highest A590:NC ratio (Figure 3.9d). However, given that the average A590 coverage does not exceed one molecule per NC, it is indeed performing as an efficient energy acceptor relative to the bound RB. The higher efficiency can readily be associated with a higher ε value of A590 in the NC-bound form. In contrast to Ga_2O_3-RB, a small negative slope is observed for a plot of R_{DA} as a function of surface coverage (Figure 3.9d). This small deviation from the constant R_{DA} value could potentially be attributed to some aggregation of the Ga_2O_3 NCs at the water-hexane boundary as a result of the increased binding time needed to achieve the desired surface coverage. Such a phenomenon would effectively reduce the concentration of the NCs in the hexane phase, leading to a lower intensity of the corresponding PL peak. Since PL measurements were used to determine the efficiency of FRET, such decrease in intensity would falsely contribute to the value of E. Nevertheless, the overall R_{DA} values were found to be within the expected range and comparable to those obtained with Ga_2O_3-RB (Table 3.6). The results for A590 bound to the NCs having different sizes are summarized in Figure 3.10 and Table 3.7, generally demonstrating the same trend as for the 3.6 nm NC. Additional data for the hybrid

conjugates based on the 4.1 and 5.0 nm NCs is presented in Figure A10/Table A5, and Figure A11/Table A6, respectively, depicting similar trends.

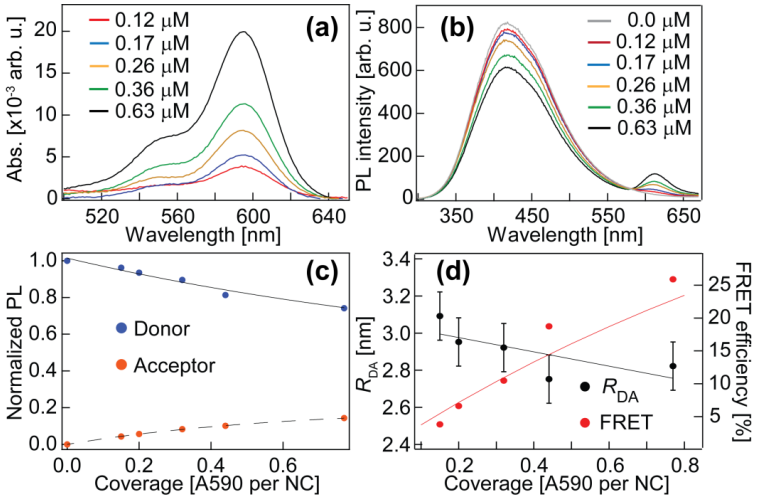

Figure 3.9. (a,b) Absorption (a) and PL (b) spectra of the 3.6 nm Ga_2O_3-A590 hybrid conjugates with the variable concentration of the bound A590 (0.12 - 0.63 μM). Concentration of the Ga_2O_3 NCs was set to 4.92×10^{14} NCs/mL for all samples, and the excitation wavelength in all cases was 230 nm. (c) Normalized PL intensities of the donor Ga_2O_3 NCs and the acceptor A590 molecules as a function of the donor-acceptor ratio *n*. (d) Variations in the FRET efficiency and the donor-acceptor separations as a function of *n*. Solid lines in (c) and (d) show fits obtained with the corresponding equations, as described in the text; dashed line in (c) is used as a guide to the eye.

Table 3.6. Summary of the FRET parameters extracted from the steady-state PL data for the 3.6 nm Ga_2O_3-A590 hybrid nanostructures with the variable surface coverage.

Bound A590 [μM]	Coverage [A590 per NC]	FRET efficiency [%]	R_{DA} [nm]
0.12	0.1	4	3.09
0.17	0.2	7	2.95
0.26	0.3	10	2.92
0.36	0.4	19	2.75
0.63	0.8	26	2.82

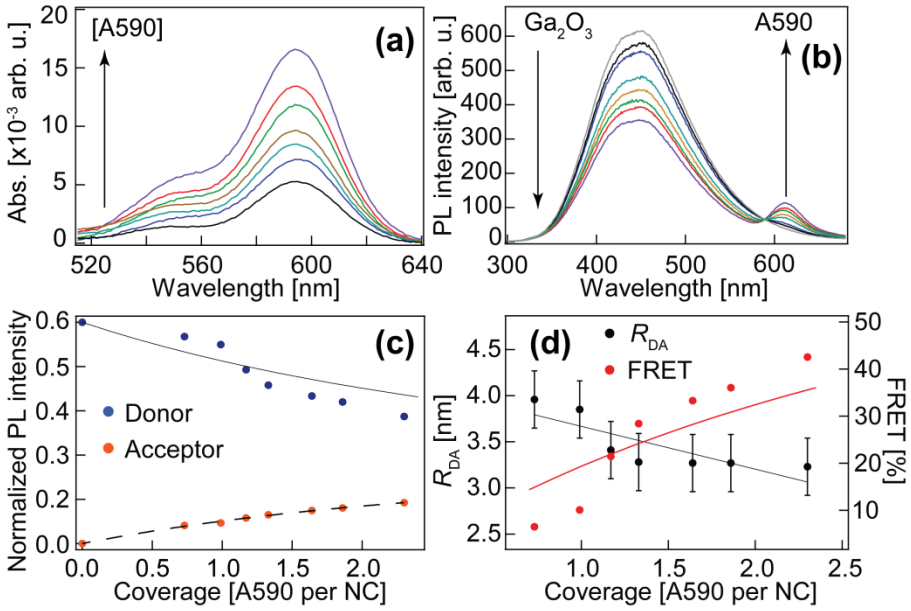

Figure 3.10. (a) Absorption and (b) PL spectra of the 5.3 nm Ga_2O_3-A590 hybrid conjugates with the variable donor-acceptor ratio, determined from the concentration of the bound A590 (0.17-0.53 μM). Concentration of the Ga_2O_3 NCs was set to 1.38×10^{14} NCs/mL for all samples, and the excitation wavelength in all cases was 230 nm. (c) Normalized PL intensities of the donor Ga_2O_3 NCs and acceptor A590 molecules as a function of the donor-acceptor ratio *n*. (d) Variations in the FRET efficiency and the donor-acceptor separations as a function of *n*. Solid lines show fits obtained with the corresponding equations, as described in the main text. Dashed line in (c) is a guide to the eye.

Table 3.7. Summary of the FRET parameters extracted from the steady-state PL data for the 5.3 nm Ga_2O_3-A590 hybrid nanostructures with the variable surface dye coverage.

Bound A590 [μM]	Coverage [A590 per NC]	FRET efficiency [%]	R_{DA} [nm]
0.17	0.7	6	3.96
0.23	1.0	10	3.85
0.27	1.2	21	3.41
0.31	1.3	28	3.28
0.38	1.6	33	3.27
0.42	1.9	36	3.27
0.53	2.3	43	3.23

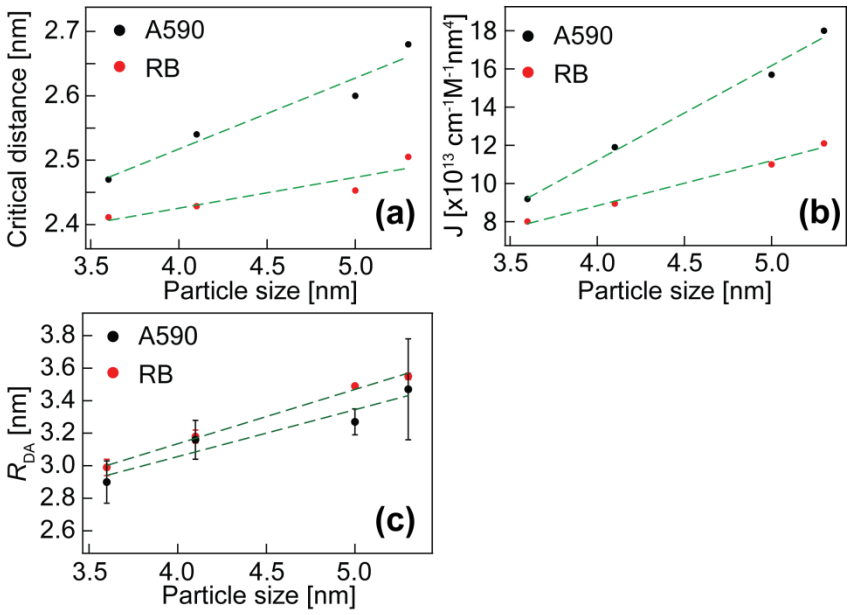

Figure 3.11. (a-c) Dependence of the FRET parameters on the average NC size for both the Ga_2O_3-RB and Ga_2O_3-A590 nanoconjugates: (a) critical (Förster) distance, (b) spectral overlap integral, and (c) donor-acceptor separation values.

Table 3.8. Summary of the FRET donor-acceptor separation distances for the Ga_2O_3-RB and Ga_2O_3-A590 hybrid nanostructures for all particle sizes.

Nanoparticle size [nm]	**R_{DA} RB [nm]**	**R_{DA} A590 [nm]**
3.6	2.99±0.03	2.90±0.13
4.1	3.18±0.04	3.16±0.12
5.0	3.49±0.01	3.27±0.08
5.3	3.55±0.02	3.47±0.31

These results show that both RB and A590 are suitable energy acceptors when bound to the surface of the Ga_2O_3 NCs. However, the comparison between the FRET parameters for the Ga_2O_3-RB and Ga_2O_3-A590 nanoconjugates reveals some important differences, allowing for a targeted design of a broad wavelength range emitters with a tunable

chromaticity. The critical distances (Figure 3.11a) and spectral overlap integrals (Figure 3.11b) for the Ga_2O_3-RB and Ga_2O_3-A590 nanoconjugates follow linear dependence on the NC size, but exhibit significantly different values and slopes. Although Ga_2O_3-RB has a larger normalized spectral overlap owing to the blue shift of the $S_0 \rightarrow S_1$ absorption band of the NC-bound RB relative to A590, the latter has nearly three times higher ε value. Larger ε of the bound A590 results in the increased J integral, in spite of the smaller spectral overlap on the normalized basis. This finding indicates that a fluorophore having a high ε in the NC-bound form could serve as an efficient energy acceptor, allowing for an increased optical density in the red part of the spectrum to generate a softer white light. The average donor-acceptor distances in RB and A590-based nanoconjugates were found to be very similar and in the expected range. The data reflect the average distribution of the defects in the NCs, as well as the dimensions or the acceptor molecules and their distribution on the NC surfaces (Figure 3.11c and Table 3.8). The conjugated systems described here demonstrate a high aptitude to generate a broad blue-orange spectrum, as a result of FRET, by a single excitation wavelength. Careful tailoring of the resulting emission chromaticity could potentially be achieved by variations in the average NC size, ratio of the dye molecules per NC, and the type of the acceptor species. Combining blue luminescence from the 3.6 nm Ga_2O_3 NCs with a complementary orange-red sensitized emission from RB could allow for the generation of the near-ideal white light in a colloidal suspension or powder form. Results related to the chromaticity analysis of the combined TCO-dye luminescence are presented in Chapter 4.

3.3 Conclusions

In summary, we investigated the electronic structure and properties of the Ga_2O_3 NCs conjugated with the organic dyes to facilitate and control a distance-dependent FRET, as a means of generating a tunable white light. We prepared a series of hybrid conjugates using different sizes of the Ga_2O_3 NCs as energy donors, functionalized with the orange-red-emitting organic dyes, as energy acceptors, by transfer across polar-non-polar solvent interface. The NC size, spectral overlap integral, molar extinction coefficient of the bound acceptor moiety, and the donor-to-acceptor ratio all play an integral role in the efficiency of the energy transfer and spectral properties of the nanoconjugate.

Binding of the organic dye molecules to the NC surfaces leads to a significant change in their electronic structure and the extinction coefficients compared to the non-bound molecules in solution, which determines the spectral overlap integral, characteristic donor-acceptor (Förster) distance, and ultimately FRET efficiency. Furthermore, we obtained other key parameters, including average number of the dye molecules bound to the NCs and the average donor-acceptor distances in the Ga_2O_3-RB and Ga_2O_3-A590 hybrid conjugates for varying NC sizes, which are also directly related to the FRET efficiency. While donor-acceptor distance is constant for the same NC size regardless of the surface coverage, it increases with size for the same dye/NC ratio. The results of this work illustrate how careful selection of the NC size and variation in the number of the acceptor dye molecules bound to each NC could be used to control FRET parameters and tune the resulting emission over a large chromaticity range. The analysis reported in this thesis demonstrates a potential for developing the new type of a single-phased white-light-emitting hybrid nanophosphor based on the dual emission resulting from the FRET coupling between functional native defects in the inorganic NCs and organic fluorophores.

Chapter 4

Analysis of the Tunable Emission from the TCO-Dye Hybrid Nanostructures

4.1 Chromaticity Analysis of the Colloidal Samples Based on the Ga_2O_3 and ZnO Nanocrystals

Since both gallium and zinc oxide NCs emit in the desired blue-green range, it was decided to examine hybrid nanostructures based on both metal oxides. Basic control over the resulting emission could be achieved by several means. Changing size or type of the nanocrystals would change the wavelength of the blue emission and, therefore, would allow for some control over the resulting chromaticity along the *y*-axis of the color space (CIE diagram). Same is true for using different dye molecules as their emission shifts from yellow-orange to red. Alternatively, variations in the number of the fluorescent dye molecules attached to the surface of the NCs would dictate the degree of the energy transfer and the resulting blue-orange color mixing. That would give control over the *x*-axis of the color space. Using all of these approaches could give a complete control over the tunability of the resulting emission. By using Ga_2O_3 or ZnO NCs of the proper sizes it was theorized that a stable white-light-emitting chromophore could be obtained based on the color complementarity with some of the dyes.

First to be studied were a series of samples based on the Ga_2O_3 NCs of variable sizes coupled with RB. The analysis was used to observe changes in the chromaticity of the emission based on changes in the particle size. Series of samples were prepared as outlined in Section 2.2.7 and the results are presented in Figure 4.1 and Table 4.1. As seen from Figure 4.1a and b, changes in the RB coverage based on the starting concentration result in a clear variation of the blue-orange emission. Intensities of said emissions vary based on the donor-acceptor ratio, and are governed by the probability of undergoing FRET from the Ga_2O_3 NCs to RB. Chromaticity analysis (Figure 4.1c and d) reveal a close complementarity of the blue DAP emission of the 3.6 nm Ga_2O_3 NCs and the orange emission from RB, with chromaticity points passing virtually through the centre of the diagram.

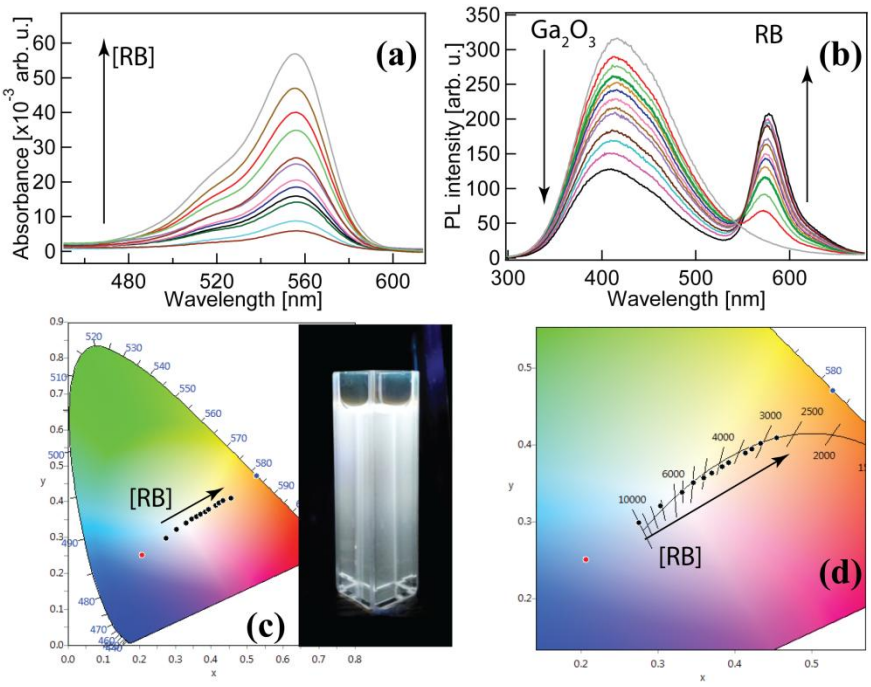

Figure 4.1. (a) UV-vis spectra of samples based on the 3.6 nm Ga_2O_3 with various amounts of RB molecules bound on the surface, exact sample concentrations are provided in Table A7. (b) Steady-state PL spectra of the same samples showing a characteristic blue-orange emission, λ_{ex} = 230 nm. (c) 1931 CIE color space depicting chromaticity of the resulting combined emission from the same samples, inset shows a colloidal white-light-emitting sample under the illumination with a 254 nm UV lamp. (d) Zoomed in section of the 1931 CIE color space including Planckian locus and CCT values, showing the same chromaticity points as in (c).

Upon UV excitation, a steady emission of white light with the chromaticity coordinates (0.332, 0.339), CCT of 5528 K and Duv of -0.001 was achieved. The resulting color of the emission can be observed in the inset of Figure 4.1c. Furthermore, a magnified section of the 1931 CIE color space with the included Planckian locus (Figure 4.1d) shows a close allocation of the resulting chromaticity points to the blackbody curve. Such important property could lead to the development of the high quality WLEDs with potentially high CRI values. Such devices could have the potential to render colors as perceived by the human eye in daylight, or mimic different artificial light sources like CFLs and incandescent bulbs. Stability and quality of the emission over time was not studied at this point.

Table 4.1. Summary of the data extracted from the chromaticity analysis of samples based on the 3.6 nm Ga_2O_3-RB hybrid nanostructures with variable amount of the bound dye.

Sample	CIE *x*	CIE *y*	CCT, K	Duv*
1.55 µM	0.275	0.298	10027	0.0084
2.56 µM	0.304	0.321	7090	0.0033
4.65 µM	0.332	0.339	5528	-0.001
5.12 µM	0.346	0.350	4946	-0.0012
6.20 µM	0.360	0.357	4471	-0.0033
7.75 µM	0.370	0.364	4203	-0.0032
9.30 µM	0.384	0.372	3870	-0.0033
10.85 µM	0.393	0.377	3682	-0.0032
13.95 µM	0.414	0.390	3295	-0.0024
15.36 µM	0.423	0.395	3171	-0.0016
20.48 µM	0.434	0.402	3030	-0.0004
25.60 µM	0.455	0.410	2759	0
3.6 nm Ga_2O_3	0.207	0.251	>100000	0.0326
RB	0.528	0.471	2343	0.0164

* Denotes distance from the Planckian locus, values less than ±0.02 coordinate units are considered acceptable for indoor applications of a given light source.

Near ideal white-light emission was obtained with the 3.6 nm Ga_2O_3 NCs, but it was decided to proceed with the analyses of other NC sizes as well. Figure 4.2b and Table 4.2 contain the data summary for the chromaticity analysis of the 4.1 nm Ga_2O_3-RB hybrid nanostructures. As expected, the resulting chromaticity coordinates moved up on the *y*-axis, since larger particles emit at longer wavelengths. Respectable CIE coordinates of (0.322, 0.347), CCT of 5961 K and Duv of 0.0078 could still be obtained.

Further analysis of the 5.0 nm Ga_2O_3-RB chromophores revealed an even greater deviation from the centre of the CIE diagram (Figure 4.2c). The closest point to the white light region of the diagram has CIE coordinates of (0.332, 0.364), CCT of 5509 K and Duv of 0.0113 (Table 4.2). Overall *y*-axis coordinates exhibit a noticeable shift toward higher values compared to the smaller Ga_2O_3 NCs. Furthermore, an even greater deviation from the blackbody curve is observed, making such chromophores potentially useful only in the narrow section of the 'warm' white range.

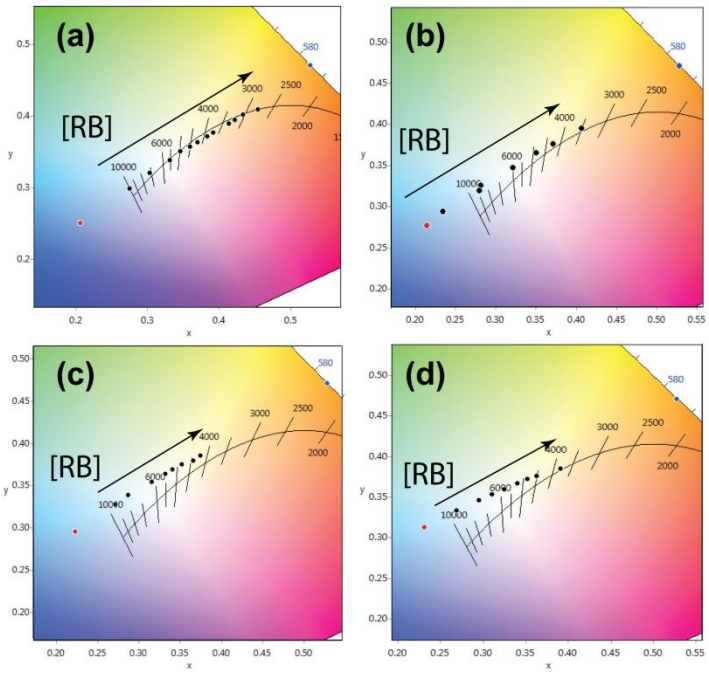

Figure 4.2. Summary of the CIE chromaticity coordinates resulting from the emission of the Ga_2O_3-RB hybrid conjugates based on the average NP size. (a) 3.6 nm NPs. (b) 4.1 nm. (c) 5.0 nm. (d) 5.3 nm. Exact sample concentrations are provided in Table A7; excitation wavelength in all cases was 230 nm.

Table 4.2. Exact chromaticity coordinates and the corresponding CCT values obtained from the analysis of the Ga_2O_3-RB hybrid conjugates based on the average NP size.

NP size	CIE x	CIE y	CCT, K	Duv
3.6 nm	0.332	0.339	5528	-0.001
4.1 nm	0.322	0.347	5961	0.0078
5.0 nm	0.332	0.364	5509	0.0113
5.3 nm	0.325	0.370	5798	0.0125

Lastly, the 5.3 nm NCs were subjected to a similar analysis. The results followed a predictable trend with the chromaticity coordinates deviating significantly from the blackbody curve and the white light centre of the color space. CIE diagram in Figure 4.2d shows points passing above the white light region, but still in a relatively close proximity of the point of equal energy. As with the

5.0 nm nanostructures, the resulting Ga_2O_3-RB chromophores could potentially be applied to the fabrication of WLEDs within the 'warm' white range.

Samples with A565 were analyzed to verify color complementarity of the dye's emission with that of the Ga_2O_3 NCs. The resulting chromaticity coordinates for the 3.6 nm Ga_2O_3-A565 (Figure 4.3a and c, and Table 4.3) appear almost identical to the ones obtained for the 3.6 nm Ga_2O_3-RB hybrid conjugates. Such similarity could be attributed to the synthetic approach in preparation of the chromophores for both RB and A565 (Section 2.2.7). Results indicate a stable emission of white light with CIE coordinates of (0.327, 0.336), CCT of 5104 K and Duv of -0.003. Using the 3.6 nm Ga_2O_3 NPs either a clear white or 'warm' white tunable emission could be generated, making A565 suitable for further examination.

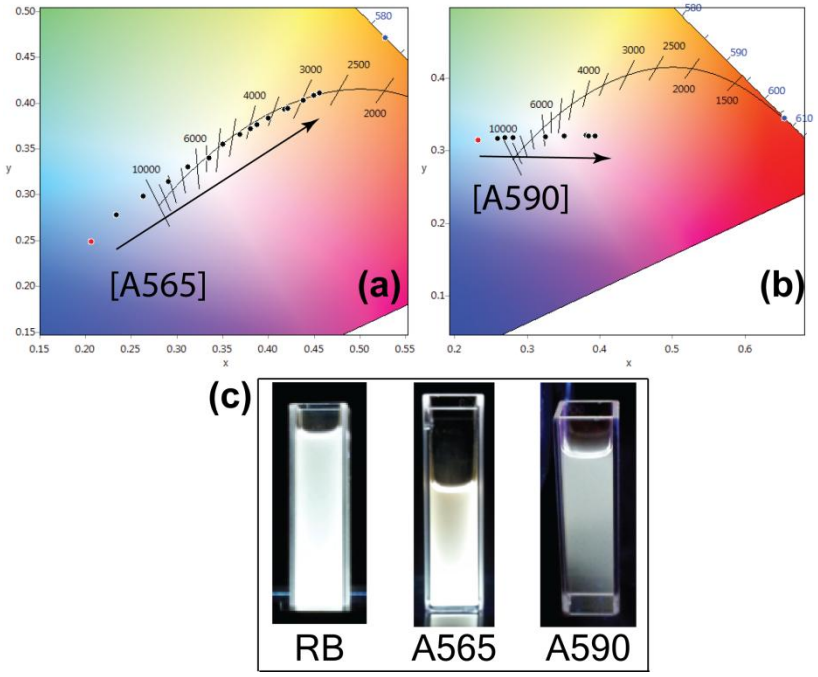

Figure 4.3. Summary of the CIE chromaticity analysis of the few samples based on the 3.6 nm Ga_2O_3-A565 (a) and 5.3 nm Ga_2O_3-A590 (a). (c) Resulting emission under the 254 nm UV lamp. Exact sample concentrations are provided in Table A7; in all cases excitation wavelength was 230 nm.

Table 4.3. Summary of the white light CIE chromaticity coordinates for the samples of the Ga_2O_3-A565 and Ga_2O_3-A590 hybrid conjugates compared to the ones obtained with RB.

Type of hybrid conjugate	CIE *x*	CIE *y*	CCT, K	Duv
3.6 nm Ga_2O_3-RB	0.332	0.339	5528	-0.001
3.6 nm Ga_2O_3-A565	0.327	0.336	5104	-0.003
5.3 nm Ga_2O_3-A590	0.326	0.319	5839	-0.0088

The last series of the Ga_2O_3-based chromophores were prepared using A590. Based on the color complementarity, it was concluded that only the largest of the Ga_2O_3 NCs could potentially result in the emission of white light. Data summary is presented in Figure 4.3b and Table 4.3. The chromaticity analysis reveals a rather poor tunability and quality of the resulting simultaneous emission compared to the other chromophores. Only a handful of points in Figure 4.3b are allocated close to the centre of the color space or the blackbody curve, therefore limiting the possible applications of such chromophores. A rather 'cool' white emission with a considerable blue tint was generated in that case (Figure 4.3c). Any subsequent adjustments to the surface coverage of the NCs resulted in either blue or blue-purple emission, which substantially deviated from the Planckian locus.

In order to expand the dataset and to further analyze the capabilities of the blue-emitting TCOs, a series of samples based on ZnO were also prepared. Based on the color complementarity, the blue-emitting ZnO nanoparticles (λ_{em} = 450-460 nm) were selected for the analysis. Upon first examination, no significant binding of RB, A565 or A590 could be obtained based on the synthetic approach (Section 2.2.7). Such conjugates were examined for color complementarity only and the emission was most likely generated by a combination of the direct excitation and FRET. Figure 4.4a, b and c and Table 4.4 contain chromaticity analysis summary for RB, A565 and A590, respectively.

Excitation of the ZnO-RB and ZnO-A565 nanostructures at 300 nm generally result in the emission passing close the point of equal energy on the CIE diagram (Figure 4.4a and Figure 4.4b). Chromaticity coordinates are allocated above the blackbody curve, similar to the 5.3 nm Ga_2O_3-RB conjugates. Figure 4.4d shows emission from the ZnO-based samples illuminated with a 254 nm UV lamp, depicting a bright white luminescence. Analysis of the ZnO-A590 hybrid nanostructures reveal similar trends as previously observed (Figure 4.4c and Table 4.4) by passing across the blackbody curve. Such characteristics make this chromophore potentially limited to a narrow range if applied in

LEDs. Overall emission was comparative to the ones observed for ZnO-RB and ZnO-A565. Chromaticity analysis of the numerous samples based on Ga_2O_3 and ZnO showed that Ga_2O_3-RB and Ga_2O_3-A565 conjugates based on the 3.6 nm NCs, as well as ZnO-A565 and ZnO-A590 chromophores have the potential to be used as phosphors in WLEDs. A series of the prototype devices were then prepared to verify the possibility of generating white light by downconverting a narrow UV emission form the commercially available UV LEDs.

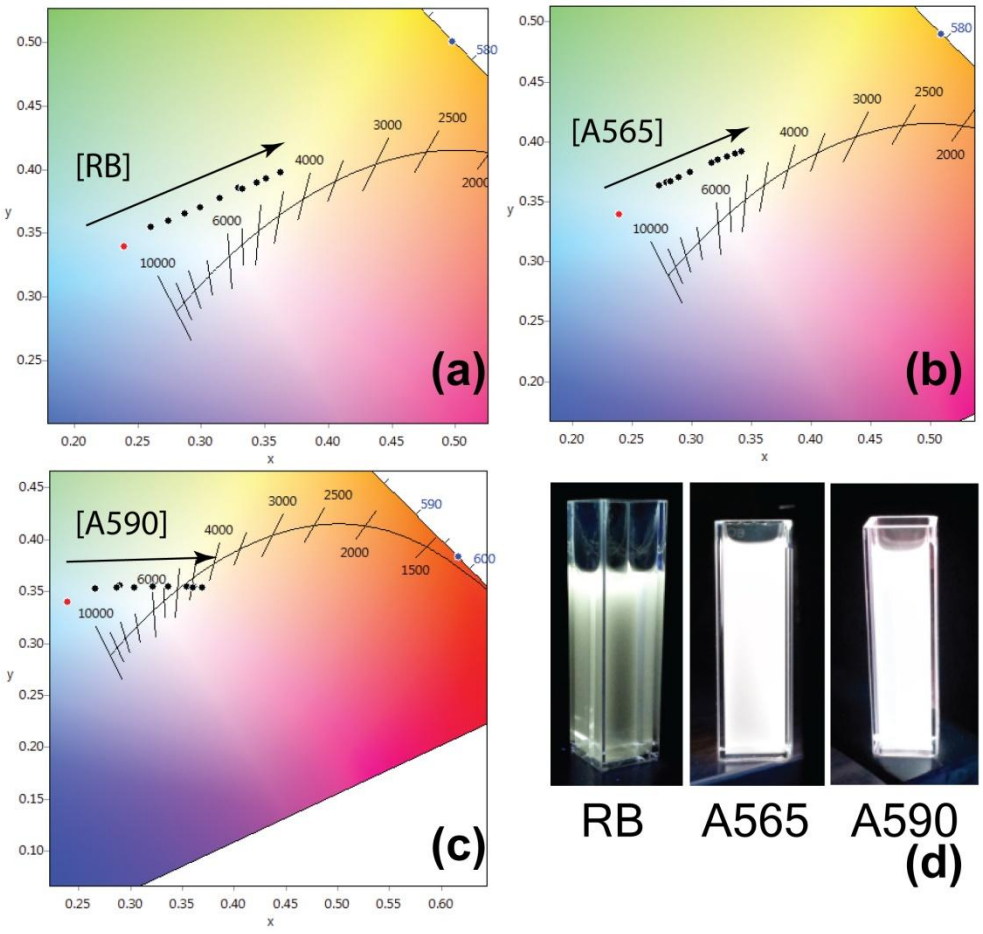

Figure 4.4. Summary of the chromaticity analysis of samples based on ZnO-RB (a), ZnO-A565 (b) and ZnO-A590 (c). Corresponding emission colors under excitation with the 254 nm UV lamp. Exact sample concentrations are provided Table A7; in all cases excitation wavelength was 300 nm.

Table 4.4. Summary of the chromaticity analysis of various ZnO-based samples emitting in the white light range.

Type of hybrid conjugate	CIE *x*	CIE *y*	CCT, K	Duv
ZnO-RB	0.333	0.385	5499	0.0205
ZnO-A565	0.330	0.387	5608	0.0230
ZnO-A590	0.337	0.355	5334	0.0049

4.2 Preparation and Characterization of the Prototype WLEDs

Based on the data obtained with the chromaticity analysis of the multiple light-emitting chromophores, it was decided to use both 255 and 300 nm UV LEDs. The use of a single white-light-emitting chromophore rather than a mix of red, green and blue phosphors could potentially allow for a greater degree of control and reproducibility of the emission. Such approach could also allow for a cheap and effective way of generating day light equivalent or any other combination of 'cool' or 'warm' white-light emission. Furthermore, if multiple chromophores based on both Ga_2O_3 and ZnO possess similar chromaticity in the powder form, such LEDs could be packaged in the same panel, further expanding the application range of the devices. Such light sources could allow a clear rendering and perception of natural colors by the human eye indoors at any point in time.

As the final objective of the current stage of the research, it was decided to use the commercially available LEDs designated UVTOP255 and UVTOP300 (Figure A12) and to deposit any given white phosphor on their surface. Design and manufacturing of a proper device was not considered at this time, so the objective was to rather demonstrate the proof of concept. Even though both LEDs have a narrow emission peak in the UV range, a faint blue radiation can still be detected (Figure A12a and c). It should be noted that the devices were not designed to serve as potential white-light emitters and did not have a suitable heat dissipation system. An additional source of the blue emission could make a proper color mixing more difficult, therefore requiring adjustments in the orange-red range. Also, the devices have a flat quartz surface (5-6 mm in diameter) suitable for deposition of the sample, which could potentially introduce some TIR. Correct thickness of the deposition layer and its uniformity were also considered, as they could reduce the quality of the

emission. Controlling these parameters was rather difficult at this point so they were not rigorously optimized to enhance the performance of the LEDs. Lastly, LEDs are known to generate a significant amount of heat, so temperature stability of the chromophores was also an issue and was considered for future studies.

Data for Ga_2O_3-RB and Ga_2O_3-A565 coated on the 255 nm LEDs is shown in Figure 4.5. The obtained chromaticity, CCT and CRI are presented in Table 4.5. The numbers indicate a rather poor CRI score for the red reference (Figure 4.5a and b) since RB lacks a broad emission in that range (610-640 nm and longer wavelengths). Overall good quality and stable white light emission is achieved for both Ga_2O_3-RB, and Ga_2O_3-A565 (Figure 4.5d and f). The tuning ability is found to be quite low and unpredictable, as indicated by the scattered points on the chromaticity diagrams in Figure 4.5c and e. During the analysis the UV chip was producing a bright spot in the centre, interfering with the measurements. That was countered by the deposition of a thick layer of the sample. Such approach, however, reduced the brightness of the emission due to possible self-absorption and reflection of the emissive layer, and introduced an uneven surface. This, in turn, further reduced the chromaticity and the CRI of the device. It was then decided to increase sample thickness only at the centre of the device where the emissive component was allocated; such approach alleviated most of the issues allowing for a continuous generation of a near perfect white light as seen in the pictures of the LEDs. Furthermore, upon storage for 2-4 days under standard atmospheric conditions the deposited white samples started to turn pink and the resulting emission developed a stronger red hue. However, considering that the experimental conditions and the preparation method of the WLED, the resulting chromophores and prototype WLEDs performed relatively well. A clear demonstration of the FRET-mediated emission of the near-perfect white light was achieved and demonstrated. Designing a proper LED could eliminate most of the issues currently encountered.

ZnO-A565 and ZnO-A590 chromophores performed better when deposited on either 255 or 300 nm LED (Figure 4.6 and Figure 4.7) resulting in a near-perfect white light emission (Table 4.5). Samples were found to be more stable with regard to the operating temperature and storage in air. Actual luminous efficacies of the devices were not measured at this point but the visual brightness of the ZnO-based devices was noted to be greater than that of the Ga_2O_3-based ones. Also, the tunability of the emission for ZnO-A565 and ZnO-A590 was found to be better, resulting in the chromaticity points allocated along the blackbody curve. Such properties could allow the devices to be fine tuned

to emit light in either 'cool' or 'warm' spectral regions based on the requirements, making ZnO-based chromophores a quite promising future development.

In conclusion, a series of white-light-emitting chromophores based on metal oxide NCs and organic dyes demonstrated a clear and stable emission of white light in both colloidal and powder forms upon UV excitation. Simple synthetic approach resulted in a relatively stable and tunable single chromophores capable of downconverting a narrow UV emission into visible light covering both cool and warm ranges. Design of a proper LED or a pair of completely inorganic phosphors could make such devices more efficient and stable for general lighting applications.

Table 4.5. Summary of the key chromaticity parameters for the few WLEDs prepared using various Ga_2O_3 and ZnO-based white-light-emitting chromophores coated on the 255 nm and 300 nm UV LEDs.

Material	LED type	CIE *x*	CIE *y*	CCT, K	Duv	CRI
Ga_2O_3-RB	255 nm	0.323	0.320	5953	-0.0070	88
Ga_2O_3-A565	255 nm	0.326	0.319	5796	-0.0091	83
ZnO-A565	255 nm	0.332	0.334	5500	-0.0034	88
ZnO-A565	300 nm	0.323	0.346	5937	0.0068	86
ZnO-A590	255 nm	0.333	0.345	5476	0.0019	92
ZnO-A590	300 nm	0.334	0.338	5416	-0.0021	91

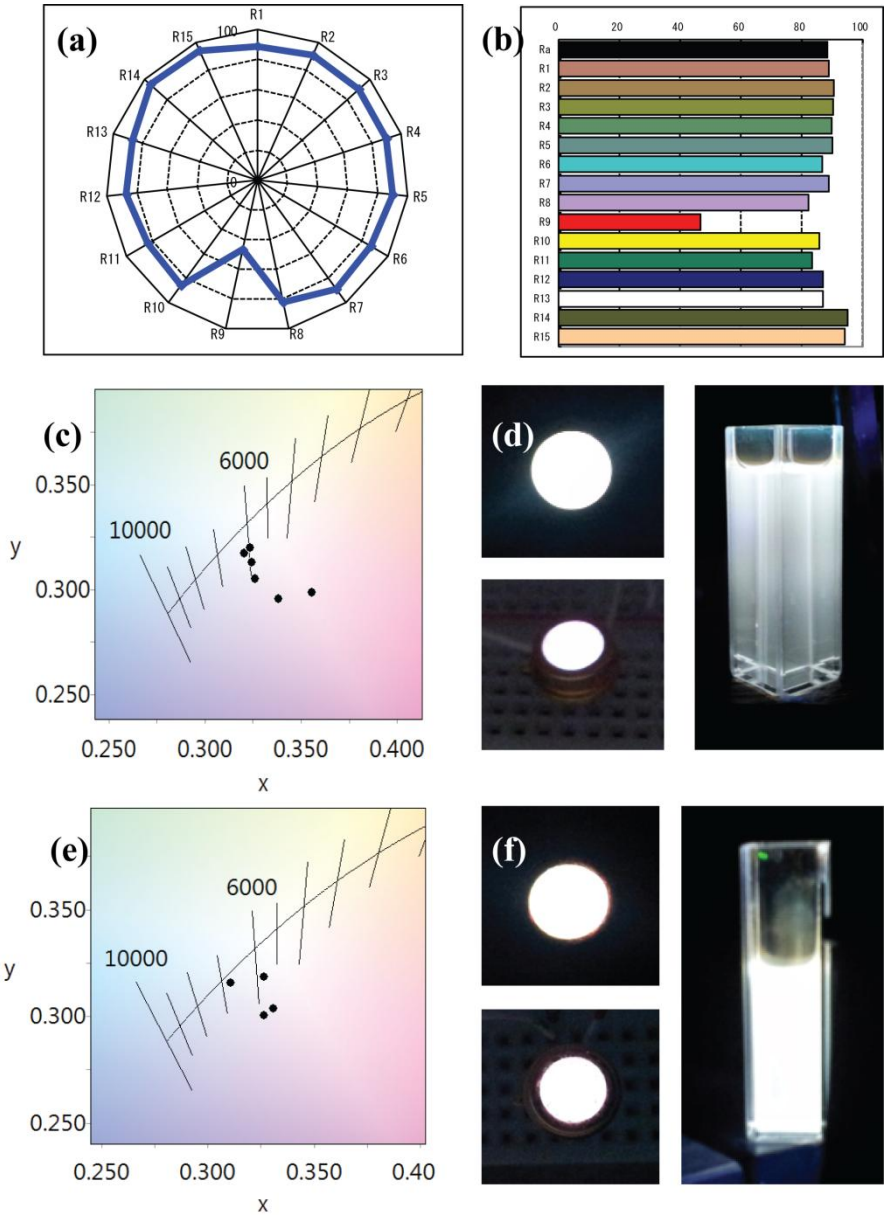

Figure 4.5. (a) CRI diagram for LEDs based on the 3.6 nm Ga_2O_3-RB and Ga_2O_3-A565 white-light-emitting chromophores. (b) Representations of the corresponding color reference samples *R1-R15* used in determining the final CRI score of the devices. (c) 1931 color space showing chromaticity of the emission from the Ga_2O_3-RB based WLEDs. (d) Emission from the 255 nm UV LED (left) coated with a white-light-emitting sample (right) operating at 6.5 V. (e) and (f) Similar type of data and images for the Ga_2O_3-A565 based WLEDs.

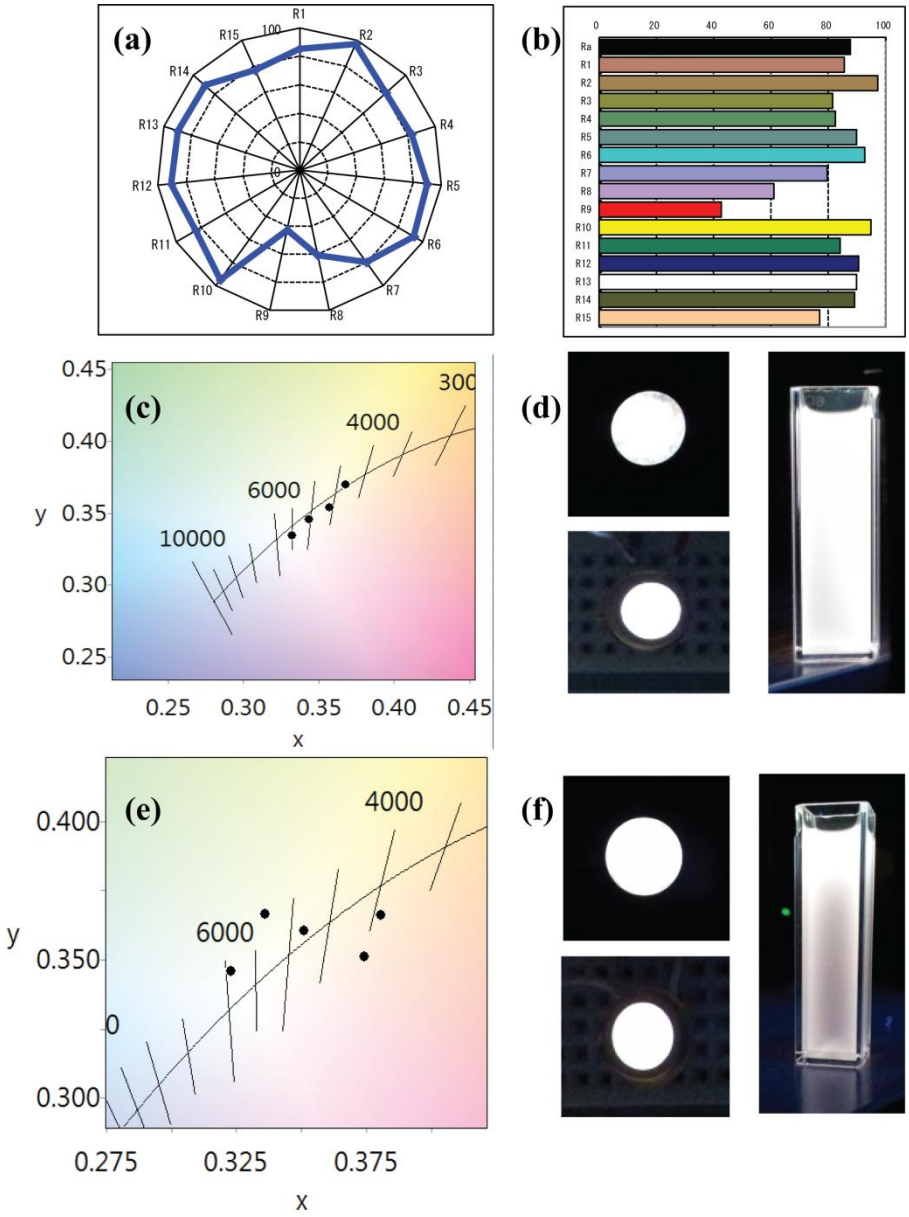

Figure 4.6. (a) CRI diagram for LEDs based on the 3.0 nm ZnO-A565 white-light-emitting chromophore. (b) Representations of the corresponding color reference samples *R1-R15* used in determining the final CRI score of the devices. (c) 1931 color space showing chromaticity of the emission from the ZnO-A565 based 255 nm WLEDs. (d) Emission from the 255 nm UV LED (left) coated with a white-light-emitting sample (right) operating at 7.0 V. (e) and (f) Similar type of data for the ZnO-A565 coated on the 300 nm UV LED.

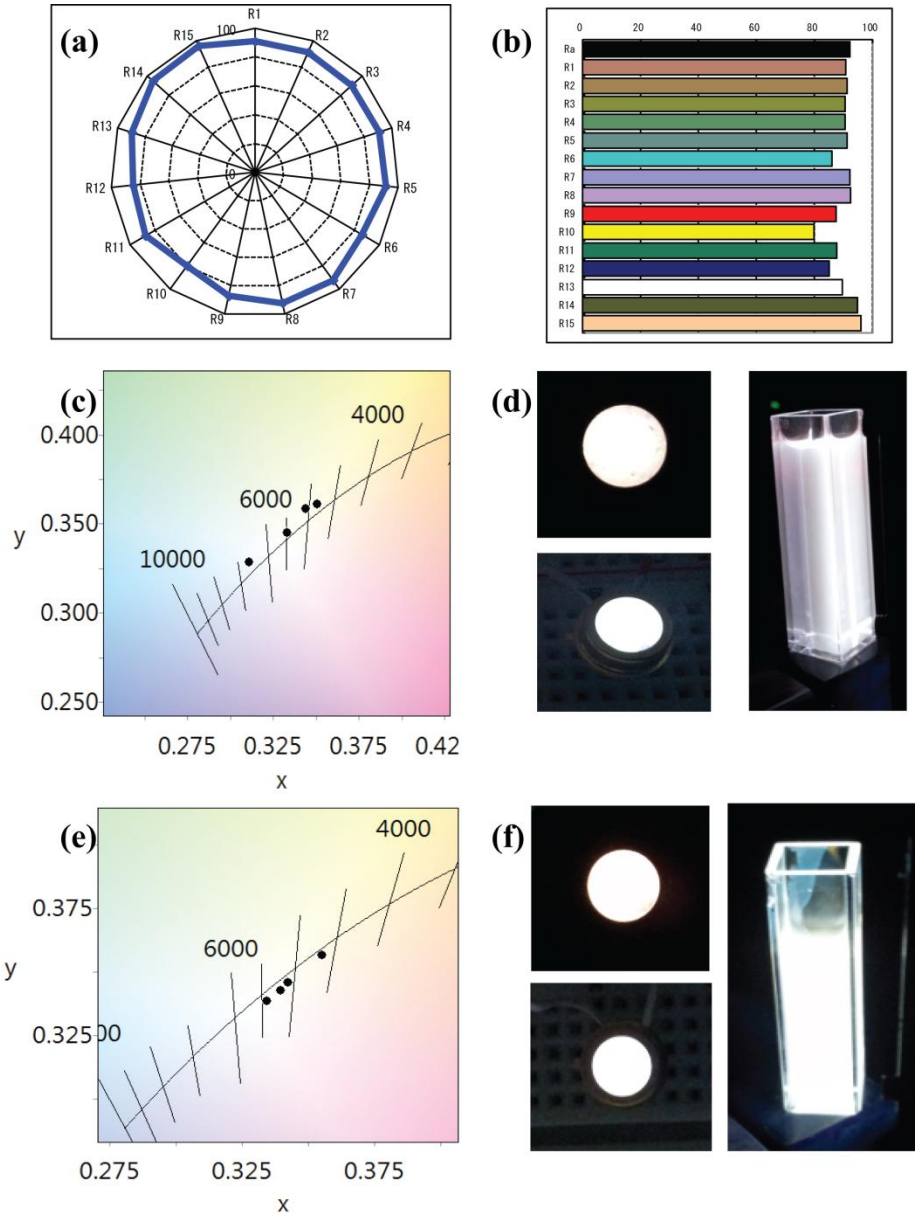

Figure 4.7. (a) CRI diagram for LEDs based on the 3.0 nm ZnO-A590 white-light-emitting chromophore. (b) Representations of the corresponding color reference samples *R1-R15* used in determining the final CRI score of the devices. (c) 1931 color space showing chromaticity of the emission from the ZnO-A590 based 255 nm WLEDs. (d) Emission from the 255 nm UV LED (left) coated with a white-light-emitting sample (right) operating at 7.0 V. (e) and (f) Similar data for the ZnO-A590 coated on the 300 nm UV LED.

4.3 Conclusions

A series of white-light-emitting chromophores based on the Förster resonance energy transfer between TCOs and organic dyes were prepared, analyzed and applied in preparation of several WLEDs. A simple hybrid nanostructure based on γ-Ga_2O_3 and RB was selected as a model system based on the broad tunable blue emission, originating from the defect sites on the NCs and a complementary yellow-orange emission from the dye. Additionally, Ga_2O_3-A590 hybrid conjugates were also analyzed to demonstrate the generality of the synthetic approach.

Efficient FRET between Ga_2O_3 NCs and RB dye could be used to generate a tunable blue-orange emission covering a wide range of the color space. Subsequent analysis of the colloidal samples in hexane produced a near-perfect white light luminescence with the chromaticity coordinates of (0.332, 0.339) and CCT of 5528 K. Similar high quality emission was achieved in the powder form as well upon deposition of such phosphor on the surface of a UV LED. Chromaticity as high as (0.323, 0.320), CCT of 5953 K and CRI of 88 were obtained with Ga_2O_3-RB deposited on the 255 nm UV LED. Even a simple device preparation approach resulted in an efficient downconversion of a narrow UV emission to a visible white luminescence. The outlined approach showed a great potential behind the FRET-mediated chromophores as cheaper, tunable and potentially equally effective phosphors for WLEDs. Designing a properly structured WLED or developing a completely inorganic chromophore could potentially greatly increase the existing properties and performance of such devices.

4.4 Future Work

Additional FRET analysis should be conducted on the Ga_2O_3-RB hybrid conjugates taking into the account particle size distribution, NC defect distribution and the statistical distribution of the acceptors on the surface of the donor NCs. Further binding analysis should be conducted by modeling a specific sample size distribution. Such results may indicate the maximum theoretical number of the binding sites and the maximum amount of dye a certain NC size group can have in the bound state. It would be beneficial to know the theoretical upper limit for the NC surface coverage with the RB molecules for any future data analysis. Design and fabrication of a proper prototype LED is also of benefit, though such project would require an engineering approach. The full potential of RB as a complementary WLED phosphor and performance of such LEDs should be further examined.

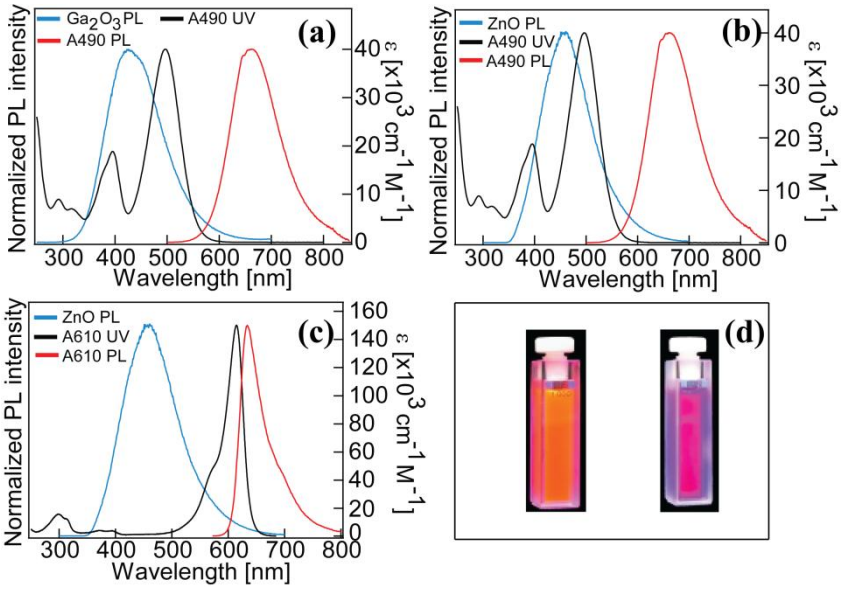

Figure 4.8. (a) Spectral overlap between the blue emission from the 3.6 nm Ga_2O_3 NPs and absorption of the red-emitting A490 dye. (b) Spectral overlap between the blue-cyan emission from the ZnO NPs and absorption of the red-emitting A490 dye. (c) Spectral overlap between the blue-cyan emission from the ZnO NPs and absorption of the red-emitting A610 dye. (d) A490 (left) and A610 (right).

The obtained set of data could also be expanded with the use of other ATTO dyes. Possible candidates could include ATTO-490LS (A490, LS denotes large Stokes shift) and ATTO-610 (A610). UV-vis, PL and corresponding spectral overlaps with Ga_2O_3 and ZnO NCs are shown in Figure 4.8. Both molecules have smaller dimensions that could potentially simplify and improve binding to the NCs. They seem to provide a good degree of spectral overlap with both types of the metal oxides, though A490 may be more susceptible to the direct excitation under UV light. If they maintain their spectral properties in the bound state, then the efficiency of the potential FRET could be high. Downside may include the potentially narrow tunability of the resulting combined emission as both dyes emit in the red region.

Additionally, a completely inorganic approach to development of the white-light-emitting chromophore is also an option. Possible combination of inorganic phosphors may include TCO-QD. Other potential solutions could be light-emitting polymers or transition-metal-based coordination compounds of Os or Ru emitting in the orange-red. Main limitation of such approaches could be the

generally small dimensions of the Ga_2O_3 and ZnO NCs and long polymer chains. Attachment of either QDs or Os/Ru-based compounds could require the use of linkers such as silane bridging agents, which may impact QY of the nanoparticles. Coordination compounds are generally incorporated into a polymer matrix, which later forms an emissive layer in the LED, so their attachment to the surfaces of the NCs could be challenging. Generally, emission in such complexes is facilitated through electron-hole injection and not through the energy transfer. Polymers would also most likely require larger NC to be applied effectively and even then a possible core/shell synthetic route could be taken. Another approach could be directed toward improving the QY of the donor NCs to facilitate a more efficient energy transfer to the donor species.

Appendix: Additional Figures and Tables

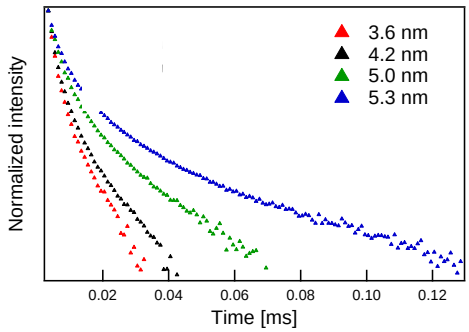

Figure A1. PL decay curves of the Ga_2O_3 colloidal NCs having different average particle sizes

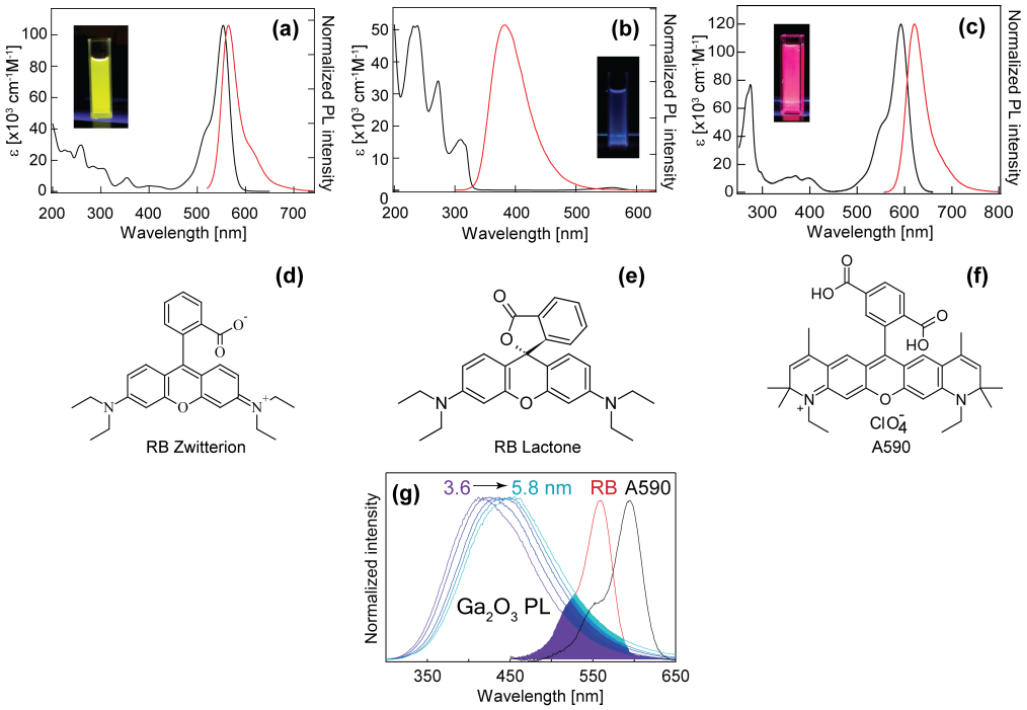

Figure A2. (a-c) Absorption (black) and PL (red) spectra of (a) RB zwitterion ($\lambda_{ex.}$ = 550 nm), (b) RB lactone ($\lambda_{ex.}$ = 230 nm), and (c) A590 ($\lambda_{ex.}$ = 590 nm). Insets: Photographs showing the emission of the corresponding fluorophores. (d-f) Molecular structures of (d) RB zwitterion, (e) RB lactone, and (f) A590. (g) Overlap between the PL spectra of the Ga_2O_3 NCs of variable sizes with the absorption spectra of RB and A590, used to calculate the values of the spectral overlap integral *J*.

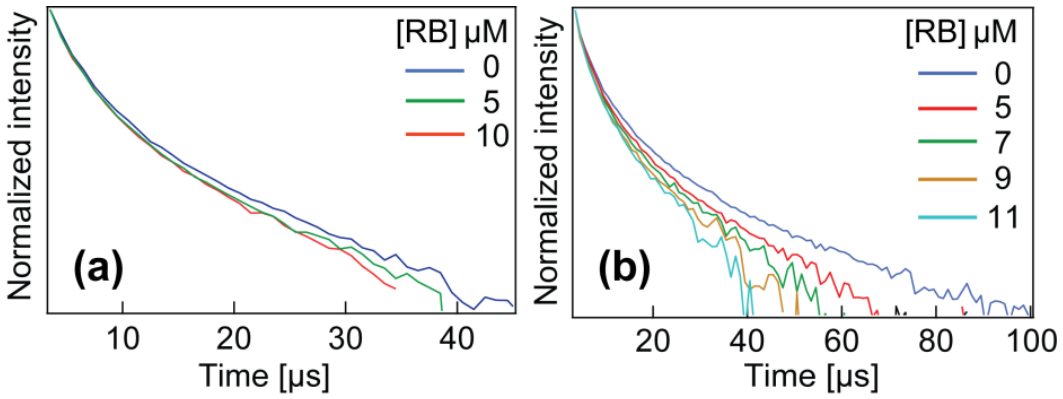

Figure A3. (a) PL decay curves of the 4.1 nm Ga_2O_3 NCs with increasing coverage of RB (excitation wavelength 230 nm; emission monitored at 420 nm). (b) Similar data for the 5.3 nm NCs, but the emission was monitored at 450 nm. The starting RB concentrations corresponding to different decay curves are indicated in the graphs. Fitting parameters are summarized in Table A1.

Table A1. Summary of lifetimes for the 4.1 and 5.3 nm Ga_2O_3 NCs with increasing RB surface coverage, estimated using exponential fitting approximation.

4.1 nm Ga_2O_3		**5.3 nm Ga_2O_3**	
Starting dye concentration [μM]	**Lifetime [μs]**	**Starting dye concentration [μM]**	**Lifetime [μs]**
0	5.20	0	6.66
5	5.08	5	6.00
10	4.97	7	5.86
		9	5.66
		11	5.35

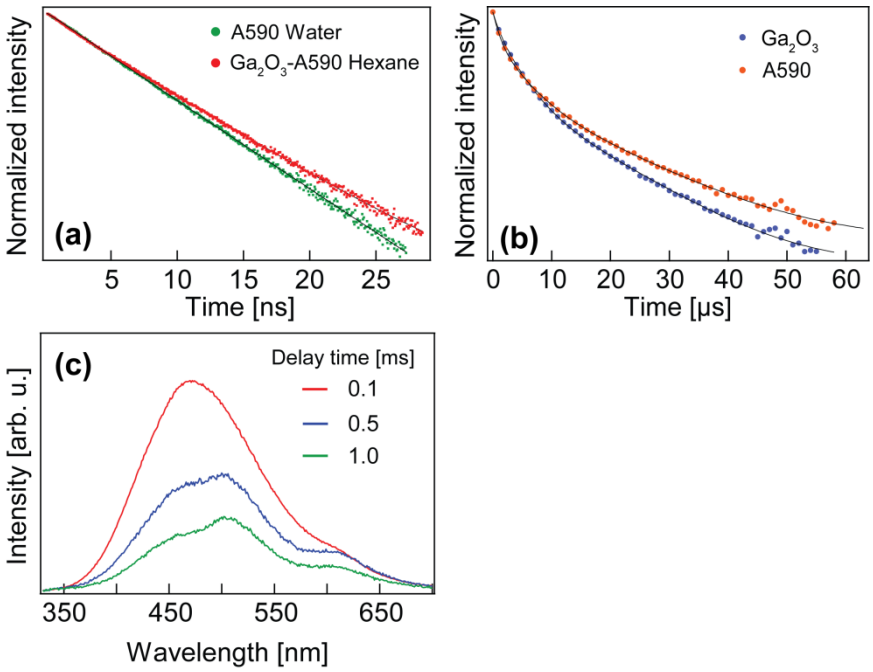

Figure A4. (a) Normalized PL decay profiles of the free A590 in water, and A590 bound to the 5.3 nm Ga_2O_3 NCs in hexane (λ_{exc}=563 nm; λ_{em} = 620 nm). (b) Normalized PL decay curves of the same sample of the bound A590 (red dots) and the 5.3 nm Ga_2O_3 NCs (blue dots) upon excitation at 230 nm. Solid lines indicate exponential fits. Fitting parameters can be found in Table A2. (c) Time-gated PL spectra of the 5.3 nm Ga_2O_3−A590 conjugates in hexane as a function of the delay upon excitation (gate time, 5 ms; λ_{exc}, 230 nm).

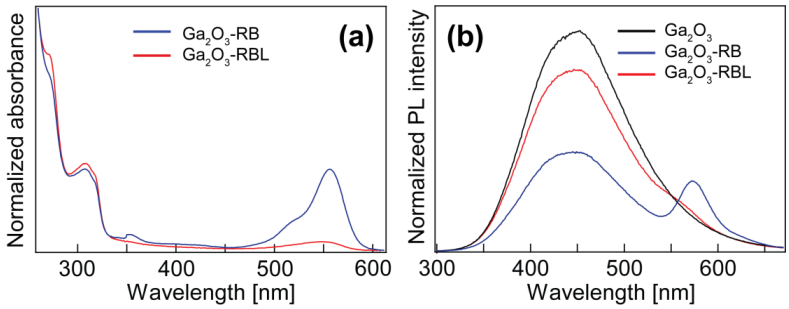

Figure A5. (a) Absorption spectra of the samples having RBL (red) and RB (blue) on the 5.3 nm Ga_2O_3 ($1.38x10^{14}$ NCs/mL) with similar concentrations in hexane (3.01 μM). (b) PL spectra of the same two samples after excitation at 230 nm, black spectrum denotes emission of the 5.3 nm Ga_2O_3 with no dye.

Table A2. Summary of the lifetime parameters obtained from exponential fitting of the decay curves of RB and A590 under direct (dye absorption maximum) and FRET-mediated excitation. Values in brackets indicate normalized fractional intensity for the corresponding lifetime component.

Sample	τ_1 [ns]	τ_2 [ns]	τ_3 [ns]	$\tau_{average}$ [ns]
RB in water (direct excitation)	1.50 (100.0 %)			1.50
RB in ethanol (direct excitation)	2.78 (100 %)			2.62
RB bound to NCs (direct excitation)	2.25 (29 %)	4.01 (71 %)		3.50
RB bound to NCs (sensitized emission)	523.20 (61 %)	2085.20 (31 %)	8018.10 (8 %)	5105
A590 in water (direct excitation)	4.17 (100 %)			3.54
A590 bound to NCs (direct excitation)	1.11 (18 %)	4.51 (80 %)	8.96 (2 %)	3.96
A590 bound to NCs (sensitized emission)	3441.80 (34 %)	11604.80 (9 %)	887.60 (57 %)	6235

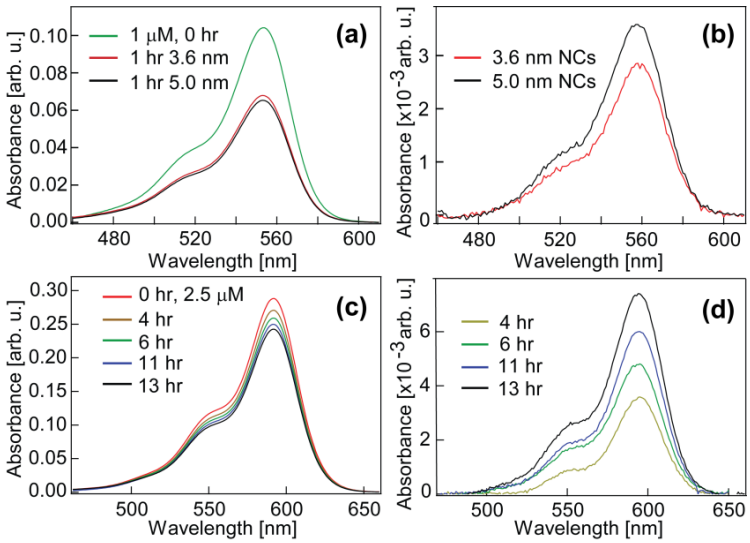

Figure A6. Determination of the molar extinction coefficient of the NC-bound dyes. (a) Absorption spectra of the aqueous solution of RB before (green) and after binding to the 3.6 and 5.0 nm NCs (red and black, respectively) for 1 hour. (b) Absorption spectra of the NC-bound RB in hexane taken after 1 hour of binding from the water solution to the 3.6 and 5.0 nm Ga_2O_3 NCs having the same band gap absorbance. (c) Absorption spectra of the aqueous solution of A590 before (red) and after binding to the 3.6 nm Ga_2O_3 NCs over time. (d) Absorption spectra of A590 bound to the NCs in hexane.

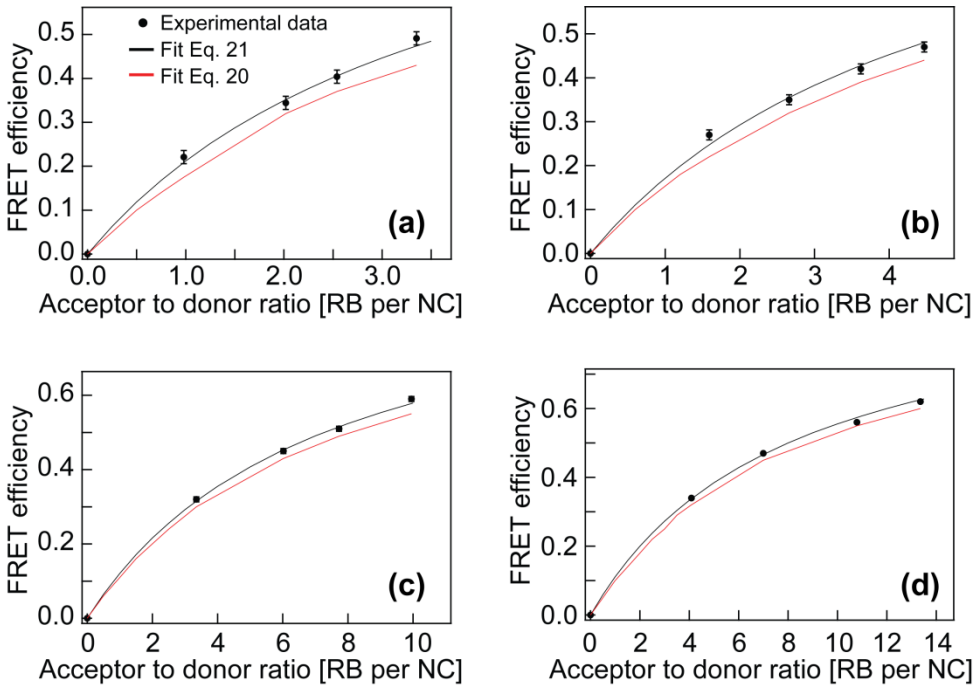

Figure A7. Comparison of the experimental data fitting for the FRET efficiency, assuming a constant (average) number of the acceptor molecules per NC (Equation 21) and accounting for a possible Poisson distribution of the acceptors (Equation 20) for the hybrid conjugates based on the 3.6 (a), 4.1 (b), 5.0 (c) and 5.3 nm (d) Ga_2O_3 NCs, expressed as a function of the acceptor-to-donor ratio. In all cases black dots denote experimental data, black curve - fitting to Equation 21, red curves - fitting to Equation 20. Error bars in (c) and (d) are too small and are obscured by the markers.

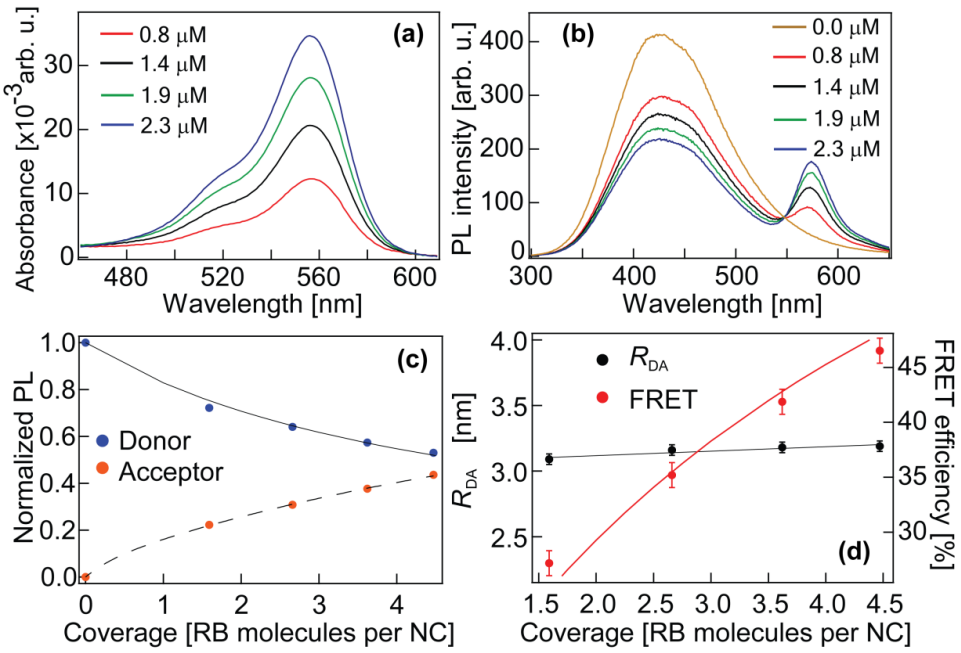

Figure A8. UV-Vis (a) and PL (b) spectra of the 4.1 nm Ga_2O_3-RB hybrid conjugates with the variable donor-acceptor ratios based on the concentration of the bound RB (0.8 - 2.3 μM). Concentration of the Ga_2O_3 NCs was set to $3.14x10^{14}$ NP/mL for all samples, excitation wavelength in all cases was 230 nm. (c) Normalized PL intensities of the donor Ga_2O_3 NCs and acceptor RB molecules as a function of the donor-acceptor ratio *n*. (d) Variations in the FRET efficiency and the donor-acceptor separations as a function of *n*. Solid lines show data fit obtained with the corresponding equations as described in the text, dashed line in (c) is used as a guide to the eye.

Table A3. Summary of the FRET parameters extracted from the steady-state PL data for 4.1 nm Ga_2O_3-RB hybrid nanostructures with the variable surface coverage.

Bound RB [μM]	Coverage [RB per NC]	FRET efficiency [%]	R_{DA} [nm]
0.8	1.6	27	3.09
1.4	2.7	35	3.16
1.9	3.6	42	3.18
2.3	4.5	47	3.19

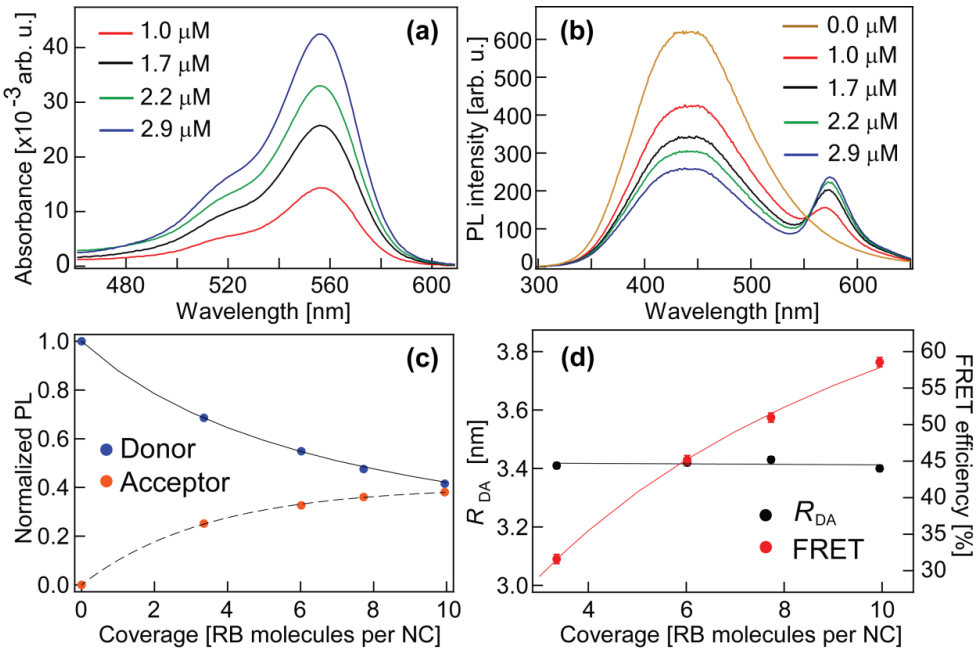

Figure A9. UV-Vis (a) and PL (b) spectra of the 5.0 nm Ga_2O_3-RB hybrid conjugates with the variable donor-acceptor ratios based on the concentration of the bound RB (1.0 - 2.9 μM). Concentration of the Ga_2O_3 NCs was set to 1.72×10^{14} NP/mL for all samples, excitation wavelength in all cases was 230 nm. (c) Normalized PL intensities of the donor Ga_2O_3 NCs and acceptor RB molecules as a function of the donor-acceptor ratio *n*. (d) Variations in the FRET efficiency and the donor-acceptor separations as a function of *n*. Solid lines show data fit obtained with the corresponding equations as described in the text, dashed line in (c) is used for guidance, error bars in (d) are too small and are obscured by markers.

Table A4. Summary of the FRET parameters extracted from the steady-state PL data for the 5.0 nm Ga_2O_3-RB hybrid nanostructures with the variable surface coverage.

Bound RB [μM]	Coverage [RB per NC]	FRET efficiency [%]	R_{DA} [nm]
1.0	3.3	32	3.41
1.7	6.0	45	3.42
2.2	7.7	51	3.43
2.9	10.0	59	3.40

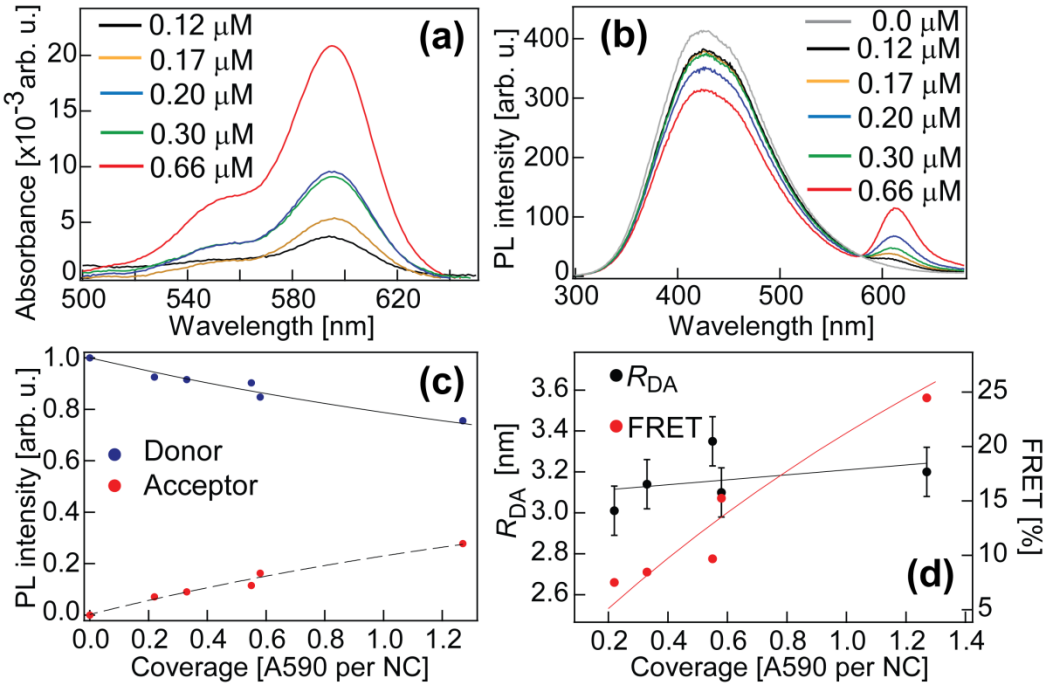

Figure A10. UV-Vis (a) and PL (b) spectra of the 4.1 nm Ga_2O_3-A590 hybrid conjugates with the variable donor-acceptor ratios based on the concentration of the bound A590 (0.12 - 0.66 μM). Concentration of the Ga_2O_3 NCs was set to $3.14x10^{14}$ NC/mL for all samples, excitation wavelength in all cases was 230 nm. (c) Normalized PL intensities of the donor Ga_2O_3 NCs and acceptor A590 molecules as a function of the donor-acceptor ratio *n*. (d) Variations in the FRET efficiency and the donor-acceptor separations as a function of *n*. Solid lines show data fit obtained with the corresponding equations, dashed line in (c) shows fit to a biexponential equation.

Table A5. Summary of the FRET parameters extracted from the steady-state PL data for the 4.1 nm Ga_2O_3-A590 hybrid nanostructures with the variable surface coverage.

Bound A590 [μM]	Coverage [A590 per NC]	FRET efficiency [%]	R_{DA} [nm]
0.12	0.2	8	3.01
0.17	0.3	9	3.14
0.29	0.5	10	3.35
0.30	0.6	15	3.10
0.66	1.3	24	3.20

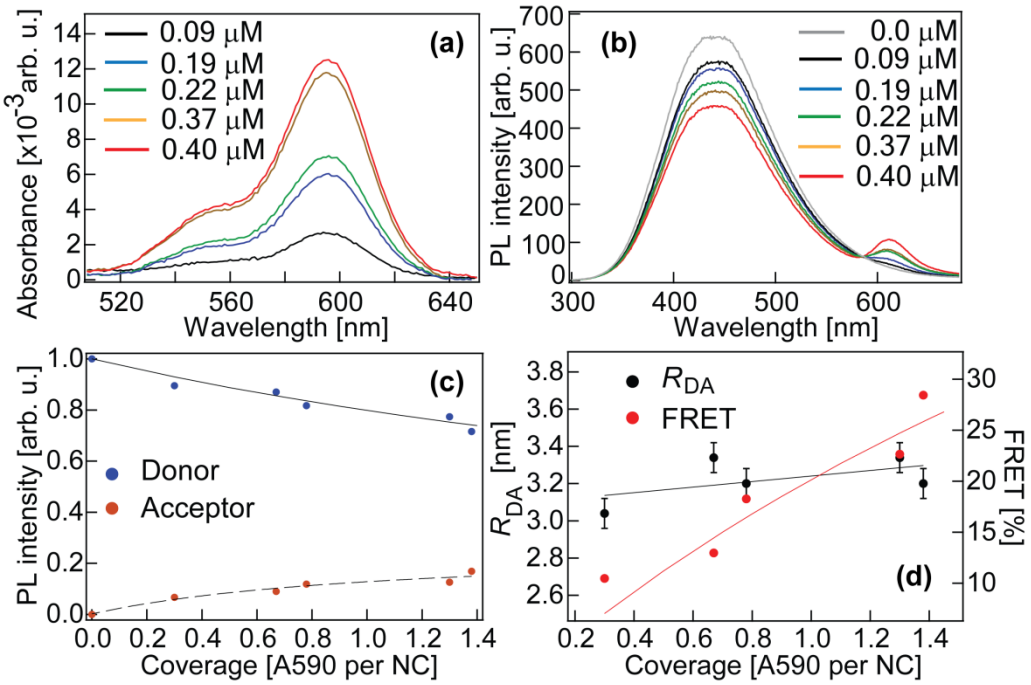

Figure A11. UV-Vis (a) and PL (b) spectra of the 5.0 nm Ga_2O_3-A590 hybrid conjugates with the variable donor-acceptor ratios based on the concentration of the bound A590 (0.09 - 0.40 μM). Concentration of the Ga_2O_3 NCs was set to 1.72×10^{14} NC/mL for all samples, excitation wavelength in all cases was 230 nm. (c) Normalized PL intensities of the donor Ga_2O_3 NCs and acceptor A590 molecules as a function of the donor-acceptor ratio *n*. (d) Variations in the FRET efficiency and the donor-acceptor separations as a function of *n*. Solid lines show data fit obtained with the corresponding equations, dashed line in (c) shows fit to a biexponential equation.

Table A6. Summary of the FRET parameters extracted from the steady-state PL data for the 5.0 nm Ga_2O_3-A590 hybrid nanostructures with the variable surface coverage.

Bound A590 [μM]	Coverage [A590 per NC]	FRET efficiency [%]	R_{DA} [nm]
0.09	0.3	10	3.04
0.19	0.7	13	3.34
0.22	0.8	18	3.20
0.37	1.3	23	3.34
0.40	1.4	28	3.20

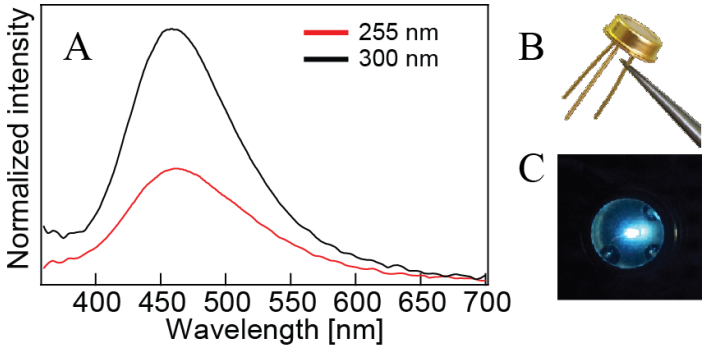

Figure A4. (a) Normalized emission spectra in the visible light range from the 255 nm and 300 nm UVTOP LEDs. (b) A typical flat top UV device used in fabrication of the WLEDs. (c) Blue emission from a standard 300 nm flat top UV LED as it appears in complete darkness.

Table A7. Summary of the dye concentrations of samples used for the CIE analysis of the emission originating from the Ga_2O_3 and ZnO-based hybrid conjugates.

Dye concentration [µM]								
3.6 nm Ga_2O_3-RB	4.1 nm Ga_2O_3-RB	5.0 nm Ga_2O_3-RB	5.3 nm Ga_2O_3-RB	3.6 nm Ga_2O_3-A565	5.3 nm Ga_2O_3-A590	ZnO-RB	ZnO-A565	ZnO-A590
1.55	1.55	1.55	1.55	0.04	0.83	0.41	0.09	0.08
2.56	4.65	4.65	3.10	0.08	1.67	0.82	0.13	0.12
4.65	6.20	6.20	4.65	0.12	2.50	1.23	0.18	0.16
5.12	9.30	9.30	6.20	0.17	3.33	1.64	0.22	0.20
6.20	12.40	10.85	7.75	0.21	4.17	2.04	0.24	0.22
7.75	13.95	12.40	9.30	0.25	5.00	2.45	0.26	0.24
9.30	15.50	13.95	12.40	0.37	6.67	2.86	0.31	0.28
10.85		15.50	15.50	0.41	8.33	3.27	0.35	0.32
13.95				0.58		3.68	0.44	0.40
15.36				0.66		4.09	0.53	0.48
20.48				0.83				
25.60								

Bibliography

1. Oeppen, J.; Vaupel, J. *Science* **2002**, *296,* 1029.
2. Pearson, P. N.; Palmer, M. R. *Nature* **2000**, *406,* 695.
3. Feely, R. A.; Sabine, C. L.; Lee, K.; Berelson, W.; Kleypas, J.; Fabry, V. J.; Millero, F. J. *Science* **2004**, *305,* 362.
4. Riebesell, U.; Zondervan, I.; Rost, B.; Tortell, P. D.; Zeebe, R. E.; Morel, F. M. M. *Nature* **2000**, *407,* 364.
5. Brown, L. R. *World on the Edge: How to Prevent Environmental and Economic Collapse;* W.W. Norton & Company: New York, N.Y., 2011.
6. Azevedo, I. L.; Morgan, M. G.; Morgan, F. The Transition to Solid-State Lighting. *Proceedings of the IEEE* **2009**, *97,* 481.
7. U.S. Department of Energy, *Energy Efficiency & Renewable Energy*, *PNNL-SA-94206* **2013**, 4.
8. Navigant Consulting, Inc. *Solid-state Lighting Research and Development Portfolio: Multi-year program plan FY'07-FY'12*, 2006.
9. Osram. *The economical alternative: Osram Dulux El Electronic Energy Saving Lamps*, 2006.
10. Khan, N.; Abas, N. *Renewable and Sustainable Energy Reviews* **2011**, *15,* 296.
11. Yang, Y. *IEEE Transactions on Electron Devices* **2008**, *55,* 1771.
12. Xie, J.; Ni, X.; Fan, Q.; Shimada, R.; Özgür, Ü.; Morkoç, H. *Appl. Phys. Lett.* **2008**, *93,* 121107.
13. Gardner, N. F.; Müller, G. O.; Shen, Y. C.; Chen, G.; Watanabe, S.; Götz, W.; Krames, M. R. *Appl. Phys. Lett.* **2007**, *91,* 234506.
14. Monemar, B.; Sernelius, B. E. *Appl. Phys. Lett.* **2007**, *91,* 181103.
15. Kim, M. H.; Schubert, M. F.; Dai, Q.; Kim, J. K.; Schubert, E. F.; Piprek, J.; Park, Y. *Appl. Phys. Lett.* **2007**, *91,* 183507.
16. Assadourian, E. *Vital Signs: The Trends That are Shaping Our Future;* W.W. Norton & Company: New York, USA, 2005.
17. Round, H. J. *Electrical World* **1907**, *49,* 309.
18. Novikov, M. A. *Physics of the Solid State* **2004**, *46,* 1.
19. Holonyak, N.; Bevacqua, S. F. *Applied Physics Letters* **1962**, *1,* 82.

20. Schubert, E. F. *Light-Emitting Diodes;* Cambridge University Press: Cambridge, UK, 2006.

21. Feng, Z. H.; Qi, Y. D.; Lu, Z. D.; Lau, K. M. *Journal of Crystal Growth* **2004**, *272,* 327.

22. Krames, M. R.; Shchekin, O. B.; Mueller-Mach, R.; Mueller, G. O.; Zhou, L.; Harbers, G.; Craford, M. G. *J. Disp. Technol.* **2007**, *3,* 160.

23. Smet, P. F.; Parmentier, A. B.; Poelman, D. *J. Electrochem. Soc.* **2011**, *158,* R37.

24. Srivastava, A. M.; Comanzo, H. A. *White-light-emitting Phosphor Blend for LED Devices*. U.S. Patent 6,501,100, December 31, 2002.

25. Lee, I. S. *White-light-emitting Diode*. U.S. Patent 7,759,683, July 20, 2010.

26. Srivastava, A. M.; Duggal, A. R.; Comanzo, H. A.; Beers, W. W. *Single Phosphor for Creating White-light with High Luminosity and High CRI in a UV LED Device*. U.S. Patent 6,522,065, February 18, 2003.

27. Setlur, A. A.; Radkov, E. V.; Henderson, C. S.; Her, J.-H.; Srivastava, A. M.; Karkada, N.; Kishore, M. S.; Kumar, N. P.; Aesram, D.; Deshpande, A.; Kolodin, B.; Grigorov, L. S.; Happek, U. *Chem. Mater.* **2010**, *22,* 4076.

28. Huang, C.-H.; Liu, W.-R.; Chen, T.-M. *J. Phys. Chem. C* **2010**, *114,* 18698.

29. Lee, M. T.; Tseng, M. R. *White-light Organic Electroluminescent Element*. U.S. Patent 7,772,762, August 10, 2010.

30. Kamtekar, K. T.; Monkman, A. P.; Bryce, M. R. *Adv. Mater.* **2010**, *22,* 572.

31. Bowers II, M. J.; McBride, J. R.; Rosenthal, S. J. *J. Am. Chem. Soc.* **2005**, *127,* 15378.

32. CIE. *Commission Internationale de l' Éclairage Proceedings, 1931;* Cambridge University Press: Cambridge, 1932.

33. Wright, W. D. *Transactions of the Optical Society* **1928**, *30,* 141.

34. Guild, J. *Phil. Trans. R. Soc. Lond. A* **1932**, *230,* 149.

35. Schanda, J. *Colourimetry: Understanding the CIE System;* John Wiley & Sons: Hoboken, NJ, 2007.

36. Nassau, K. *The Physics and Chemistry of Color, 2nd ed.;* John Wiley & Sons: New York, USA, 2001.

37. Borbely, A.; Samson, A.; Schanda, J. *Color Research and Application* **2001**, *26,* 450.

38. Schanda, J.; Sándor, N. *Lighting Research and Technology* **2005**, *38*, 225.

39. Guo, X.; Houser, K. W. *Lighting Research and Technology* **2004**, *36*, 183.

40. Davis, W.; Ohno, Y. *Optical Engineering* **2010**, *49*, 033602.

41. Murphy, T. W. *J. Appl. Phys.* **2012**, *111*, 104909.

42. Yam, F. K.; Hassan, Z. *Microelectronics Journal* **2005**, *36*, 129.

43. Schubert, E. F.; Kim, J. K. *Science* **2005**, *308*, 1274.

44. Ye, S.; Xiao, F.; Pan, Y. X.; Ma, Y. Y.; Zhang, Q. Y. *Materials Science and Engineering R* **2010**, *71*, 1.

45. Anikeeva, O. P.; Halpert, J. E.; Bawendi, M. G.; Bulović, V. *Nano Lett.* **2007**, *7*, 2196.

46. Nizamoglu, S.; Zengin, G.; Demir, H. V. *Appl. Phys. Lett.* **2008**, *92*, 031102.

47. Chen, H.-S.; Hong, H.-Y.; Kumar, R. V. *J. Mater. Chem.* **2011**, *21*, 5928.

48. Dai, Q.; Foley, M. E.; Breshike, C. J.; Lita, A.; Strouse, G. F. *J. Am. Chem. Soc.* **2011**, *133*, 15475.

49. Panda, S. K.; Hickey, S. G.; Volkan Demir, H.; Eychmuller, A. *Angew. Chem. Int. Ed.* **2011**, *50*, 4432.

50. Park, S.; Kwon, J. E.; Kim, S. H.; Seo, J.; Chung, K.; Park, S.-Y.; Jang, D.-J.; Medina, B. M.; Gierschner, J.; Park, S. Y. *J. Am. Chem. Soc.* **2009**, *131*, 14043.

51. Zhen, H.; Xu, W.; Yang, W.; Chen, Q.; Xu, Y.; Jiang, J.; Peng, J.; Cao, Y. *Macromol. Rapid Commun.* **2006**, *27*, 2095.

52. Smith, R.; Liu, B.; Bai, J.; Wang, T. *Nano Lett.* **2013**, *13*, 3042.

53. Maiti, D. K.; Bhattacharjee, R.; Datta, A.; Banerjee, A. *J. Phys. Chem. C* **2013**, *117*, 23178.

54. Chen, Q.; Dai, N.; Liu, Z.; Chu, Y.; Ye, B.; Li, H.; Peng, J.; Jiang, Z.; Li, J.; Wang, F.; Yang, L. *Applied Physics A* **2014**, *115*,1159.

55. Alam, M. M.; Jenekhe, S. A. *Macromolecular Rapid Communications* **2006**, *27*, 2053.

56. Pan, Z. W.; Dai, Z. R.; Wang, Z. L. *Science* **2001**, *291*, 1947.

57. Brus, L. E. *J. Chem. Phys.* **1983**, *79*, 5566.

58. Alivisatos, A. P. *Science* **1996**, *271*, 933.

59. Nazzal, A. Y.; Qu, L.; Peng, X.; Xiao, M. *Nano Lett.* **2003**, *3*, 819.

60. Nakamura, S.; Mukai, T.; Senoh, M. *Appl. Phys. Lett.* **1994**, *54*, 1687.

61. Arnold, S. P.; Prokes, S. M.; Perkins, F. K.; Zaghloul, M. E. *Appl. Phys. Lett.* **2009**, *95*, 103102.

62. Yang, H.; Shi, R.; Yu, J.; Liu, R.; Zhang, R.; Zhao, H.; Zhang, L.; Zheng, H. *J. Phys.Chem. C* **2009**, *113*, 21548.

63. Jamieson, T.; Bahshi, R.; Petrova, D.; Pocock, R.; Imani, M.; Seifalian, A. M. *Biomaterials* **2007**, *28*, 4717.

64. Haase, M.; Schafer, H. *Angew. Chem. Int. Ed.* **2011**, *50*, 5808.

65. Boyer, J.-C.; Vetrone, F.; Cuccia, L. A.; Capobianco, J. A. *J. Am. Chem. Soc.* **2006**, *128*, 7444.

66. Iijima, M.; Kamiya, H. *KONA Powder and Particle Journal* **2009**, *27*, 119.

67. Schulz-Dobrick, M.; Sarathy, K. V.; Jansen, M. *J. Am. Chem. Soc.* **2005**, *127*, 12816.

68. Jiang, H.; Moon, K. S.; Li, Y.; Wong, C. P. *Chem. Mater.* **2006**, *18*, 2969.

69. Yoshikawa, J.; Lewis, J. A.; Chun, B. *J. Am. Ceram. Soc.* **2008**, *92*, S42.

70. Plueddemann, E. P. *J. Adhesion* **1970**, *2*, 184.

71. Abrams, B. L.; Holloway, P. H. *Chemical Reviews.* **2004**, *104*, 5783.

72. Sykora, M.; Petruska, M. A.; Alstrum-Acevedo, J.; Bezel, I.; Meyer, T. J.; Klimov, V. I. *J. Am. Chem. Soc.* **2006**, *128*, 9984.

73. Petruska, M.; Bartko, A. P.; Klimov, V. I. *J. Am. Chem. Soc.* **2004**, *126*, 714.

74. Boulesbaa, A.; Issac, A.; Stockwell, D.; Huang, Z.; Huang, J.; Guo, J.; Lian, T. *J. Am. Chem. Soc.* **2007**, *129*, 15132.

75. Clapp, A. R.; Medintz, I. L.; Mattoussi, H. *Phys. Chem. Chem. Phys.* **2006**, *7*, 47.

76. Hyeok, J.; Kim, J. Y.; Chin, B. D.; Kim, Y. C.; Kim, J. K.; Park, O. O. *Nanotechnology* **2004**, *15*, 1217.

77. Beane, G. A.; Morfa, A. J.; Funston, A. M.; Mulvaney, P. *J. Phys. Chem. C.* **2012**, *116*, 3305.

78. Förster, V. T. *Ann. Phys.* **1948**, *6*, 54.

79. Lacowicz, J. R. *Principles of Fluorescence Spectroscopy, 3rd ed.;* Springer: New York, 2006.

80. Stryer, L.; Haugland, R. P. *Proc. Natl. Acad. Sci. U.S.A.* **1967**, *58*, 719.

81. Haugland, R. P.; Yguerabide, J.; Stryer, L. *Proc. Natl. Acad. Sci. U.S.A.* **1969**, *63,* 23.

82. Cantor, C. R.; Pachukas, P. *Proc. Natl. Acad. Sci. USA* **1971**, *68,* 2099.

83. Clapp, A. R.; Medintz, I. L.; Mauro., M. J.; Fisher, B. R.; Bawendi, M. G.; Mattoussi, H. *J. Am. Chem. Soc* **2004**, *126,* 301.

84. Corry, B.; Jayatilaka, D.; Martinac, B.; Rigby, P. *Biophysical Journal* **2006**, *91,* 1032.

85. Loura, L. M. S. *Int. J. Mol. Sci.* **2012**, *13,* 15252.

86. Steinberg, I. Z. *J. Phys. Chem.* **1968**, *48,* 2411.

87. Dale, R. E.; Eisinger, J.; Blumberg, W. E. *Biophysical Journal* **1979**, *26,* 161.

88. Langhals, H.; Esterbauer, A. J.; Walter, A.; Riedle, E. *J. Am. Chem. Soc.* **2010**, *16777,* 132.

89. Nalbach, P.; Pugliesi, I.; Langhals, H.; Thorwart, M. *Physical Review Letters* **2012**, *108,* 218302.

90. Iqbal, A.; Arslan, S.; Okumus, B.; Wilson, T. J.; Giraud, G.; Norman, D. G.; Ha, T.; Lilley, D. M. J. *Proc. Natl. Acad. Sci. USA* **2008**, *105,* 11176.

91. Lillo, M. P.; Beechem, J. M. *Biochemistry* **1997**, *36,* 11261.

92. Binet, L.; Gourier, D. *J. Phys. Chem. Solids* **1998**, *59,* 1241.

93. Roy, R.; Hill, V. G.; Osborn, E. F. *J. Am. Chem. Soc.* **1952**, *74,* 719.

94. Lorenz, M. R.; Woods, J. F.; Gambino, R. J. *J. Phys. Chem. Solids* **1967**, *28,* 403.

95. Harwig, T.; Kellendonk, F.; Slappendel, S. *J. Phys. Chem. Solids* **1978**, *39,* 675.

96. Harwig, T.; Kellendonk, F. *J. Solid State Chem.* **1978**, *24,* 255.

97. Hegde, M.; Wang, T.; Miskovic, Z. L.; Radovanovic, P. V. *Appl. Phys. Lett.* **2012**, *100,* 141903.

98. Wang, T.; Farvid, S. S.; Abulikemu, M.; Radovanovic, P. V. *J. Am. Chem. Soc.* **2010**, *132,* 9250.

99. Wang, T.; Radovanovic, P. V. *J. Phys. Chem. C* **2011**, *115,* 18473.

100. Wang, T.; Radovanovic, P. V. *Chem. Comm.* **2011**, *47,* 7161.

101. Wang, T.; Layek, A.; Hosein, I. D.; Chirmanov, V.; Radovanovic, P. V. *J. Mater. Chem. C* **2014**, *2,* 3212.

102. Vimont, A.; Lavalley, J. C.; Sahibed-Dine, A.; Arean, C. O.; Delgado, M. R.; Daturi, M. *J. Phys. Chem. B* **2005**, *109,* 9656.

103. Playford, H. Y.; Hannon, A. C.; Barney, E. R.; Walton, R. I. *Chem. Eur. J.* **2013**, *19,* 2803.

104. Srinivas, N. K. M. N.; Rao, S. V.; Rao, D. N. *J. Opt. Soc. Am. B* **2003**, *20,* 2470.

105. Casey, K. G.; Quitevis, E. L. *J. Phys. Chem.* **1988**, *92,* 6590.

106. Arbeloa, F. L.; Ojeda, P. R.; Arbeloa, I. L. *Journal of Luminescence* **1989**, *44,* 105.

107. Nishikiori, H.; Fujii, T. *J. Phys. Chem. B* **1997**, *101,* 3680.

108. Ramette, R. W.; Sandell, E. B. *J. Am. Chem. Soc.* **1956**, *78,* 4872.

109. Arbeloa, F. L.; Martinez, V. M.; Arbeloa, T.; Arbeloa, I. L. *J. Photochem. Photobiol. C: Photochem. Rev.* **2007**, *8,* 85.

110. Lettinga, M. P.; Zuilhof, H.; van Zandvoort, M. A. M. J. *Phys. Chem. Chem. Phys.* **2000**, *2,* 3697.

111. von Steyern, F. V.; Josefsson, J. O.; Tagerud, S. *J. Histochem. Cytochem.* **1996**, *44,* 267.

112. Klein, U. K. A.; Hafner, F. W. *Chem. Phys. Lett.* **1976**, *43,* 141.

113. Karpiuk, J.; Grabowski, Z. R.; De Schryve, F. C. *J. Phys. Chem.* **1994**, *98,* 3247.

114. ATTO-TEC. *Product Catalogue 2013/2015*.

115. Wang, T.; Chirmanov, V.; Chiu, W. H. M.; Radovanovic, P. V. *J. Am. Chem. Soc.* **2013**, *135,* 14520.

116. Beane, G.; Boldt, K.; Kirkwood, N.; Mulvaney, P. *J. Phys. Chem. C* **2014**, *118,* 18079.

117. Dennis, A. M.; Bao, G. *Nano Lett.* **2008**, *8,* 1439.

118. Pons, T.; Medintz, I. L.; Wang, X.; English, D. S.; Mattoussi, H. *J. Am. Chem. Soc.* **2006**, *128,* 15324.

119. Funston, A. M.; Jasieniak, J. J.; Mulvaney, P. *Adv. Mater.* **2008**, *20,* 4274.

120. Blumen, A.; Klafter, J.; Zumofen, G. *J. Chem. Phys.* **1986**, *84,* 1397.

121. Aldeek, F.; Ji, X.; Mattoussi, H. *J. Phys. Chem. C* **2013**, *117,* 15429.

122. Dworak, L.; Matylitsky, V. V.; Ren, T.; Basché, T.; Wachtveitl, J. *J. Phys. Chem. C* **2014**, *118,* 4396.

123. Halivni, S.; Sitt, A.; Hadar, I.; Banin, U. *ACS Nano* **2012**, *6,* 2758.

124. Sitt, A.; Even-Dar, N.; Halivni, S.; Faust, A.; Yedidya, L.; Banin, U. *J. Phys. Chem. C* **2013**, *117,* 22186.

125. Steinberg, I. Z. *Annu. Rev. Biochem.* **1971**, *40,* 83.

126. Yang, J.; Winnik, M. A. *J. Phys. Chem. B* **2005**, *109,* 18408.

127. Ren, T; Mandal, P. K.; Erker, W.; Liu, Z.; Avlasevich, Y.; Puhl, L.; Müllen, K.; Basché, T. *J. Am. Chem. Soc.* **2008**, *130*, 17242.

128. Farvid, S. S.; Wang, T.; Radovanovic, P. V. *J. Am. Chem. Soc.* **2011**, *133*, 6711.

129. Melhuish, W. H., *J. Phys. Chem.* **1961,** 65, 229.

130. Johansson, M. K.; Fidder, H.; Dick, D.; Cook, R. M. *J. Am. Chem. Soc.* **2002**, *124*, 6950.

131. Marras, S. A. E.; Kramer, F. R.; Tyagi, S. *Nucl. Acids Res.* **2002**, *30*, e122.